

DISS. ETH NO. 24762

# Heat transfer characteristics of spray impingement in mobile selective catalytic reduction systems

A thesis submitted to attain the degree of  
DOCTOR OF SCIENCES of ETH ZURICH  
(Dr. sc. ETH Zurich)

presented by

**Yujun Liao**

Master of Science in Energy Science and Technology  
ETH Zurich

born on 11.08.1989  
citizen of China

accepted on the recommendation of  
Prof. Dr. Konstantinos Boulouchos, examiner  
Dr. Panayotis Dimopoulos Eggenschwiler, co-examiner

2017



*To my family*



# Acknowledgments

This PhD thesis was conducted in the laboratory for Automotive Powertrain Technologies at Empa, Swiss Federal Laboratories for Materials Science and Technology.

First of all, I would like to express my gratitude to my supervisor Dr. Panayotis Dimopoulos Eggenschwiler for giving me this excellent opportunity. His careful supervision over the past three years helped me complete the work timely and successfully. His encouragement helped me stand up and move forward when I was falling down.

Also, I would like to give my special thank to Prof. Konstantinos Boulouchos, head of the Aerothermochemistry and Combustions System Laboratory at ETH Zurich for accepting me as a PhD candidate, his scientific insights and patient supervision throughout my study since my master at ETH Zurich.

I would like to thank Christian Bach, head of Laboratory for Automotive Powertrain Technologies at Empa, for his support and trust in me. I would also like to thank Dr. Alexander Spiteri, who gave me the opportunity to perform my master thesis with him and introduced me to the group. Special thanks to Daniel Schreiber, whose engineering experiences and magic hands helped me make all experiments possible. I also thank all my officemates, Thibaut, Viola and Francesco I, for pulling me out of sorrow and making fun together. I would also like to thank the students, Alex, Francesco II and Moyu, who contributed to the work in the form of master thesis or semester project. The proofreading help from Jimmy and Benjamin is also highly appreciated. Working at Empa has been a pleasure, I would like to extend my gratitude to everybody from the laboratory for Automotive Powertrain Technologies (Abt. 504), for providing such a great atmosphere.

My special thanks go to all scientific collaborators I have worked with, Dr. Graham Wigley for introducing me the phase Doppler anemometry technique, Roman Furrer and Dr. Erwin Hack for lending me the IR camera and sharing with me their IR thermography knowledge, Dr. Peter Zolliker for his hand on imaging processing issues, Lorenzo Nocivelli and Prof. Gianluca Montenegro for the numerical simulation cooperations and enlightening discussions, Dr. Daniel Rentsch for the cooperation on nuclear magnetic resonance spectroscopic measurements, Martina Lingg for helping me coat some gold mirrors. Also, I would like to thank my experimental colleagues from LAV at ETH Zurich, Dr. Schneider, Ales, Maria, Thomas for lending me experimental apparatus and giving me a hand whenever I needed it. I enjoyed working with all of them.

Last but not least, I would like to thank my family. My parents gave me the freedom to choose whatever I wanted to do and always stood on my side. I also sincerely thank my grandma, who always prepared my favourite food every time I went back home. Finally, I would like to thank all my friends, in particular my boyfriend, for their encouragement and continuous support.

Zürich, August 2017

Yujun Liao

# Abstract

Selective catalytic reduction (SCR) is the state-of-the-art technology to abate NO<sub>x</sub> emissions for mobile applications with oxygen abundance in the exhaust gas. One of the major implementation challenges is avoiding the formation of solid deposits, which are mainly caused by the urea-water solution spray impingement on exhaust duct walls. The present thesis is a comprehensive analysis of the spray impingement, which is not only of paramount importance for solid deposit formation, but also for the reducing agent distribution and the NO<sub>x</sub> reduction.

Fluid dynamic characteristics of the spray before impingement have been investigated experimentally in detail. The impinging as well as the entrained and evaporated spray fractions have been characterized and quantified based on intrusive and non-intrusive measuring techniques. The heat transfer characteristics of the impingement have been analyzed from different perspectives. The impingement of a single spray event has been analyzed for identification of the impingement regimes using IR thermography and the droplets kinetic properties. Furthermore, measurements of consecutive impingement series have resulted in the quantification of the heat transferred and the identification of the regimes associated to local evaporation phenomena. High speed imaging has been used for a phenomenological characterization of solid deposit formation process. The investigations have involved a comprehensive set of exhaust flow and injection parameters.

Phase Doppler Anemometry has been applied to measure the droplet sizes and velocities prior to the wall impingement. Sauter mean diameters of the droplets from the injectors examined are between 60 and 80  $\mu\text{m}$ . Prior to wall impingement, higher impinging velocities (vertical component, normal to the wall) are associated with larger droplets,

while smaller droplets are strongly decelerated by the aerodynamic drag during the movement towards the wall. For the 3-hole injector, over 95 % of droplets possess Mundo numbers  $K$  lower than 150 regardless of exhaust flow conditions.

Impinging spray mass flux distributions have been quantified leading to empirical correlations of entrainment and evaporation levels as a function of the flow parameters. Based on an integrated analysis of a mechanical patternator and Phase Doppler Anemometry results, it is concluded that droplets below 20  $\mu\text{m}$  are completely entrained or evaporated. The impingement rate is increasing with increasing droplet diameter up to 90  $\mu\text{m}$ . Droplets larger than 90  $\mu\text{m}$  are likely to impinge.

Infrared thermography has been used to capture the rear surface temperature distribution of a plate immersed in the exhaust flow during a single spray impingement event, with a focus on examining the influence of exhaust flow conditions. The resulting temperatures have been used for assessing the heat extracted from the plate by solving the 1D inverse heat conduction. The spray impingement leads to a substantial and rapid temperature drop on the wall, resulting in a maximum heat flux of  $\text{MW}/\text{m}^2$  during the injection duration. The spray cooling effect decreases with increasing exhaust gas flow rate due to enhanced entrainment. Increase in gas flow temperature affects the heat transfer by increasing the wall temperature. At lower wall temperatures, the principal spray/wall interaction regime is deposition. With increasing wall temperature, there is a shift to rebound and thermal breakup. The shorter contact times in the rebound and thermal breakup regimes result in decreased spray/wall heat transfer.

Furthermore, the intrinsic heat transfer characteristics of the urea-water spray impingement on hot surfaces have been investigated. Infrared thermography has been applied to measure the rear side temperature of the spray impinged plate over multiple injection process. The spray impinged side temperature and heat flux distributions have been computed by solving the 3D inverse heat conduction in the plate with the sequential function specification method. Measurements have shown that the instantaneous impinged plate temperature determines the spray



impingement heat transfer. Based on the plate temperature, different regimes (film boiling, transition boiling and nucleate boiling) are identified, as well as the associated heat fluxes. The critical heat flux and Leidenfrost temperature provide new insights into the urea-water spray boiling characteristics.

High speed imaging experiments have revealed liquid film formation, liquid accumulation, urea crystallization and melting prior to solid deposit formation. The spray impingement leads to liquid film formation. Direct relationship of liquid accumulation to the deposit formation has been identified. The permanent deposits are mainly consisting of cyanuric acid, as well as minor quantities of biuret, ammeline and ammeline as identified by nuclear magnetic resonance spectroscopy.

The present work is a comprehensive study of the fluid dynamic and heat transfer phenomena of the urea-water spray impingement and the resulting deposit formation process in exhaust SCR systems. To our knowledge so far, no comparable experimental work has been published. The insights are essential for designing future exhaust aftertreatment systems, as well as validating numerical simulation efforts.



# Zusammenfassung

Die selektive katalytische Reduktion (SCR) ist die aktuell effizienteste Technologie zur Senkung der NO<sub>x</sub>-Emissionen für mobile Anwendungen mit Sauerstoffüberschuss im Abgas. Diese Technik basiert auf die Einspritzung eines flüssigen Reaktionsmittels (Harnstoffwasserlösung) in das Abgas. Eine der großen Herausforderungen ist die Vermeidung der Bildung von festen Beiprodukten und entsprechenden Ablagerungen. Diese werden hauptsächlich vom Wandaufprall der Harnstoffwasserlösung beeinflusst. Die vorliegende Arbeit ist eine umfassende Analyse des Wandaufpralls, die nicht nur von grösster Bedeutung für die Ablagerungsbildung ist, sondern auch für die Ammoniakgleichverteilung und die NO<sub>x</sub>-Reduktion.

Die fluiddynamischen Eigenschaften des Sprays vor dem Aufprall wurden experimentell untersucht. Die auftreffenden sowie die mitgerissenen und verdampfenden Anteile des Sprays wurden mittels berührungslosen und intrusiv-mechanischen Messtechniken charakterisiert und quantifiziert. Die Wärmeübertragungseigenschaften des Aufpralls wurden aus unterschiedlichen Perspektiven analysiert. Der Aufprall einer einzelnen Einspritzung wurde mit Hilfe von Temperaturfeldern (gemessen mit IR-Thermographie) und der Kinetik der Tröpfchen analysiert. Dabei wurden die verschiedenen Aufprallregimes identifiziert. Darüber hinaus führten Temperaturmessungen während dem Aufprall von sequentiellen Einspritzungen zur Quantifizierung der übertragenen Wärme und zur Identifizierung der lokalen Verdampfungsphänomene. Hochgeschwindigkeitsaufnahmen wurden für eine phänomenologische Charakterisierung der Ablagerungsbildung benutzt. Die Untersuchungen wurden unter systematischen und umfassenden Variierungen von Abgasbedingungen und Einspritzparametern durchgeführt.

Mittels Phasen-Doppler-Anemometrie wurden die Tröpfchengrößen und -geschwindigkeiten unmittelbar vor dem Wandaufprall gemessen. Die Sauterdurchmesser der Tröpfchen aus den verschiedenen, untersuchten Injektoren liegen zwischen 60 und 80  $\mu\text{m}$ . Vor dem Wandaufprall weisen grössere Tröpfchen höhere Geschwindigkeiten (vertikale Komponente, normal zur Wand) auf, während kleinere Tröpfchen durch den aerodynamischen Widerstand stark abgebremst werden. Für den 3-Loch-Injektor besitzen über 95 % der Tröpfchen Mundozahlen,  $K$ , niedriger als 150, unabhängig von den Abgasströmungsbedingungen.

Die Verteilung der auftreffenden Spraymasse auf der gegenüberliegenden Wand wurde mit einem mechanischen Patternator bestimmt. Es ist dabei gelungen, empirische Korrelationen für die von der Gasströmung mitgerissener Spraymasse sowie auch für die verdampfende Spraymasse als Funktion von den Strömungsparametern zu gewinnen. Basierend auf der Analyse dieser und der Ergebnisse der Phasen-Doppler-Anemometrie, kann der Schluss gezogen werden, dass Tröpfchen unter 20  $\mu\text{m}$  vollständig mitgerissen oder verdampft werden. Der Anteil, der an der Wand aufprallenden Tröpfchen, steigt mit zunehmendem Tropfendurchmesser bis 90  $\mu\text{m}$ . Alle grösseren Tröpfchen erreichen die gegenüberliegende Wand.

Mit IR-Thermographie wurde die Temperaturverteilung der Rückseite einer in die Abgasströmung positionierten Platte während eines einzigen Sprayaufpralls erfasst. Die daraus resultierenden Temperaturen wurden für die Beurteilung des Wärmeaustausches zwischen Platte und Spray durch Lösung des 1D inversen Wärmeleitungsproblems verwendet. Der Sprayaufprall führt zu einem erheblichen und schnellen Temperaturabfall an der Platte, was zu einem maximalen Wärmestrom in der Größenordnung von  $\text{MW}/\text{m}^2$  während der Einspritzdauer führt. Der Effekt der Spraykühlung nimmt bei zunehmender Abgasströmung wegen verstärktem Tröpfchenmitreissens und somit reduzierter aufprallender Spraymasse ab. Die Erhöhung der Temperatur der Strömung beeinflusst die übertragene Wärme durch die Erhöhung der Wandtemperatur. Bei niedrigeren Wandtemperaturen führt der Aufprall zum mechanischen Auseinanderbrechen der Tröpfchen. Bei höheren Wandtemperaturen gibt es einen Wechsel auf Rückprall und thermischen Aufbruch. Die kürzeren

Kontaktzeiten im Bereich des Rückprallens und des thermischen Aufbruchs führen zu einer verminderten Spray-Platte-Wärmeübertragung.

Weiterhin wurden die Wärmeübertragungsphänomene von sequentiellen Sprayaufprallvorgängen auf der heissen Oberfläche der Platte untersucht. Mittels IR-Thermografie wurde die Temperatur auf der Rückseite der Platte über mehrere Einspritzvorgänge gemessen. Die Temperatur- und Wärmestromverteilungen der Sprayaufprallseite wurden durch Lösung des 3D inversen Wärmeleitungsproblems in der Platte mit der sequentiellen Funktionsspezifikationsmethode bestimmt. Die Messungen haben gezeigt, dass die momentane Plattentemperatur die Sprayaufprallwärmeübertragung massgeblich bestimmt. Basierend auf der Plattentemperatur werden unterschiedliche Verdampfungsbereiche (Filmsieden, Übergangssieden und Keimsieden) sowie die zugehörigen Wärmeströme identifiziert. Bestimmt wurden die Temperatur und die Höhe des kritischen Wärmestroms und die Leidenfrosttemperatur, sodass neue Einblicke im Sieverhalten von dem Harnstoffwasser-Spray gewonnen werden konnten.

Mittels Hochgeschwindigkeitsaufnahmen wurden die Bildung von flüssigen Wandfilmen, die Flüssigkeitsansammlung, die Harnstoffkristallisation und das Harnstoffschmelzen und die dann einsetzende Ablagerungsbildung qualitativ untersucht. Eine direkte Beziehung der Flüssigkeitsansammlung zur Ablagerungsbildung wurde identifiziert. Die Zusammensetzung der permanenten Ablagerungen wurde durch Kernspinresonanzspektroskopie bestimmt. Die Ablagerungen bestanden hauptsächlich aus Cyanursäure, sowie auch aus geringen Mengen Biuret, Ammelid und Ammelin.

Die vorliegende Arbeit ist eine umfassende Untersuchung der fluid-dynamischen und thermodynamischen Phänomene des Harnstoffwasser-Sprayaufpralls und des daraus resultierenden Ablagerungsbildungsprozesses in SCR-Systemen. Unseres Wissens ist keine vergleichbare experimentelle Arbeit veröffentlicht worden. Die Erkenntnisse sind entscheidend für die Entwicklung der Abgasnachbehandlungssysteme in der Zukunft sowie für die Validierung von numerischen Simulationsarbeiten.



# Contents

<b>Acknowledgments</b>	<b>v</b>
<b>Abstract</b>	<b>vii</b>
<b>Zusammenfassung</b>	<b>xi</b>
<b>Nomenclature</b>	<b>xix</b>
<b>1 Introduction</b>	<b>1</b>
1.1 Scope of investigation . . . . .	1
1.2 Literature Review . . . . .	4
1.2.1 Fundamentals of pool boiling . . . . .	4
1.2.2 UWS droplet evaporation phenomena . . . . .	6
1.2.3 Characteristics of UWS injection . . . . .	9
1.2.4 UWS spray impingement . . . . .	12
1.2.5 Spray impingement investigations in other contexts	14
1.3 Thesis outline . . . . .	18
<b>2 Phenomenology and quantitative characterization of the urea-water spray impingement</b>	<b>21</b>
2.1 Introduction . . . . .	22
2.2 Experimental setup and methods . . . . .	24
2.3 Results and Discussion . . . . .	29
2.3.1 Impinging spray mass flux distributions . . . . .	29
2.3.2 Spray impingement phenomenology . . . . .	35
2.3.3 Solid deposit composition analysis . . . . .	42
2.4 Summary . . . . .	45

<b>3</b>	<b>Fluid dynamic characteristics of the impinging spray</b>	<b>47</b>
3.1	Introduction . . . . .	48
3.2	Experimental setup and methods . . . . .	48
3.3	Results and Discussion . . . . .	53
3.3.1	Spray contours analysis . . . . .	53
3.3.2	Droplet sizes and velocities . . . . .	55
3.3.3	Droplet volume flow rates . . . . .	60
3.4	Summary . . . . .	63
<b>4</b>	<b>Heat transfer characteristics of a single spray impingement event</b>	<b>65</b>
4.1	Introduction . . . . .	66
4.2	Experimental setup and methods . . . . .	68
4.3	Computation of the spray cooling flux by solving the inverse heat conduction problem . . . . .	74
4.4	Results and discussions . . . . .	76
4.4.1	General heat transfer characteristics . . . . .	76
4.4.2	Influence of the gas flow conditions on the heat transfer characteristics . . . . .	80
4.5	Summary . . . . .	86
<b>5</b>	<b>Heat transfer characteristics of sequential urea-water spray impingement events</b>	<b>89</b>
5.1	Introduction . . . . .	90
5.2	Experimental setup and methods . . . . .	92
5.3	Solution of 3D inverse heat conduction problem . . . . .	94
5.4	Results and discussion . . . . .	98
5.4.1	Heat transfer characteristics during spray wall impingement . . . . .	98
5.4.2	Influence of the gas flow conditions and the injection duration on the heat transfer characteristics . . . . .	102
5.4.3	Critical heat flux estimation . . . . .	106
5.5	Summary . . . . .	109



<b>6</b>	<b>Conclusions and outlook</b>	<b>113</b>
6.1	Summary . . . . .	113
6.2	Conclusions and outlook . . . . .	120
	<b>Bibliography</b>	<b>133</b>
	<b>Curriculum Vitae</b>	<b>147</b>



# Nomenclature

## Abbreviations

A-A	air assisted injector
CDF	cumulative density function
$CaF_2$	calcium fluoride
CHF	critical heat flux
Ent	entrainment
EOI	end of injection
Eva	evaporation
FB	film boiling
FC	free convection
FTIR	Fourier transformed infrared spectroscopy
HPLC	high performance liquid chromatography
IHCP	inverse heat conduction problem
InSb	indium antimonide
IR	infrared
NB	nucleate boiling
ND-IR	non-dispersive infrared analyzer
NMR	nuclear magnetic resonance
P1-3H	3-hole pressure driven injector
P1-6H	6-hole pressure driven injector 1
P2-6H	6-hole pressure driven injector 2
PDA	phase Doppler anemometry
PDF	probability density function
RDE	real driving emissions
SCR	selective catalytic reduction

SMD	sauter mean diameter
SOI	start of injection
TB	transition boiling
UWS	urea water solution

## Symbols

### Latin

$c_p$	specific heat	$[\text{J}/\text{kg}\cdot\text{K}]$
$D$	droplet diameter	$[\mu\text{m}]$
$D_{32}$	sauter mean diameter	$[\mu\text{m}]$
$I_{camera}$	infrared radiation detected by the camera	$[\text{W}/\text{m}^2]$
$I(T)$	blackbody radiation at a given temperature $T$	$[\text{W}/\text{m}^2]$
$k$	thermal conductivity	$[\text{W}/\text{m}\cdot\text{K}]$
$K$	Mundo number	$[-]$
$\dot{m}$	gas mass flow rate	$[\text{kg}/\text{h}]$
$MW$	molecular weight	$[\text{g}/\text{mol}]$
$Nu$	Nusselt number	$[-]$
$Pr$	Prantl number	$[-]$
$Re$	Reynolds number	$[-]$
$T$	gas flow temperature	$[\text{°C}]$
$u$	droplet axial velocity component	$[\text{m}/\text{s}]$
$\bar{U}_{gas}$	gas mean flow velocity	$[\text{m}/\text{s}]$
$v$	droplet downward velocity component	$[\text{m}/\text{s}]$
$We$	Weber number	$[-]$
$x, y, z$	nozzle coordinate system	$[\text{mm}]$

### Greek

$\alpha$	thermal diffusivity	$[\text{m}^2/\text{s}]$
$\delta$	NMR chemical shift	$[\text{ppm}]$
$\varepsilon_{CaF_2}$	$CaF_2$ window emissivity	$[-]$
$\varepsilon_{mirror}$	mirror emissivity	$[-]$
$\varepsilon_{plate}$	plate emissivity	$[-]$

$\mu$	dynamic viscosity	$[\text{N}\cdot\text{s}/\text{m}^2]$
$\rho$	density	$[\text{kg}/\text{m}^3]$
$\rho_{CaF_2}$	$CaF_2$ window reflectivity	$[-]$
$\rho_{mirror}$	mirror reflectivity	$[-]$
$\rho_{plate}$	plate reflectivity	$[-]$
$\rho v^2$	gas flow momentum	$[\text{kg}/\text{m}\cdot\text{s}^2]$
$\sigma$	surface tension	$[\text{N}/\text{m}]$
$\tau_{CaF_2}$	$CaF_2$ window transmissivity	$[-]$
$\tau_{plate}$	plate transmissivity	$[-]$

## Subscripts and Superscripts

amb	ambient
back	background
cont	contact
d	droplet
env	environment
sat	saturation
w	wall



# 1 Introduction

## 1.1 Scope of investigation

NO<sub>x</sub> emissions are one of the major and most harmful atmospheric emissions induced by the industrial sector. They contribute to the formation of ground level ozone and acid rain, which lead to health and environmental problems. In the European Union, the transport sector is the largest contributor to NO<sub>x</sub> emissions, accounting for 46 % of total emissions in 2013. Newest limits stated in Euro VI, introduced recently, impose on additional reduction of 80 % by heavy duty diesel vehicles and 55 % by light duty diesel vehicles. However, NO<sub>x</sub> emissions from road transport have not been reduced as much as expected, since emissions in real-life driving conditions are often higher than those measured during the approval test. Therefore, the European Commission is introducing the Real Driving Emissions test procedure (RDE) starting from 1st September 2017. This poses great challenges for vehicle manufacturers and suppliers. Technologies used up to now can be divided into two major groups, one is to adapt the combustion process and the other is to treat NO<sub>x</sub> emissions in the exhaust pipe by catalysis. In the latter case, a three-way catalyst is only suitable for a narrow air-fuel ratio window with very low oxygen concentration in the exhaust, which is far from normal diesel operating conditions. Selective Catalytic Reduction (SCR) technology can effectively reduce NO<sub>x</sub> emissions under lean combustion with abundant oxygen. Exhaust SCR is a promising technique to reduce NO<sub>x</sub> emissions without sacrificing engine efficiency [1]. Fig. 1.1 schematically shows the composition of a typical SCR system. Generally speaking, selective catalytic reduction (SCR) is a means for converting nitrogen oxides NO<sub>x</sub> into nitrogen and water with the aid of

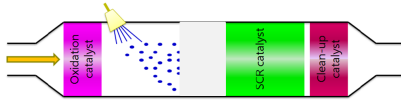
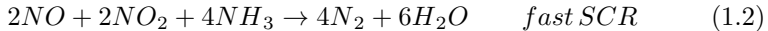
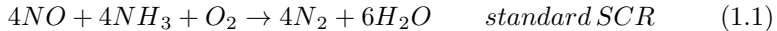


**Figure 1.1:** Schematic diagram of a typical SCR system.

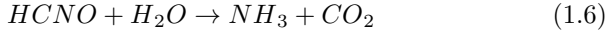
a catalyst and a reducing agent. In the SCR system ammonia ( $\text{NH}_3$ ) is used as the reducing agent. The following chemical reactions illustrate the global processes occurring in the system. Reaction 1.1 is the typical SCR reaction. When equal-molar amounts of  $\text{NO}$  and  $\text{NO}_2$  are present, reaction 1.2 dominates the process. The order of the reaction rates of these reactions is:  $1.2 \gg 1.1 \gg 1.3$ . Under normal engine combustion conditions  $\text{NO}_x$  comprises 95%  $\text{NO}$  and hence reaction 1.1 dominates. To speed up the reduction rate, an oxidation catalyst is placed upstream the urea injector to oxidize part of  $\text{NO}$  to  $\text{NO}_2$ .



In most mobile cases, urea-water-solution (UWS) is used as a source of ammonia because of its non-toxicity, and convenience of storage. UWS is sprayed into the exhaust gas flow and reactions 1.4, 1.5 and 1.6 describe the three stages of UWS releasing ammonia. The first step is the complete evaporation of water from spray droplets, followed by the thermolysis reaction 1.5 and finally the hydrolysis reaction 1.6.







These reactions are endothermic processes, thus heat transfer issues are critical for the proper preparation of the reducing agent. Yim [2] examined the thermal decomposition of urea over a fixed-bed flow reactor with non-dispersive infrared analyzer (ND-IR) and high performance liquid chromatography (HPLC). Kim [3] studied the products of the urea decomposition in function of residence time in the hot exhaust flow of different temperatures using Fourier-transform infrared spectroscopy (FTIR). It was found that the thermal decomposition increased with increasing temperature and residence time. According to [2], at 350 °C the residence time required for complete thermal decomposition was 0.1 s. The catalyst downstream has a negligible effect on the thermal decomposition, however favors the hydrolysis reaction at a temperature as low as 150 °C. Musa [4] and Wang [5] studied the evaporation characteristics of a single UWS droplet suspended over a quartz fiber in electric furnaces under quiescent conditions. Grout [6] applied Mie scattering to deduce the global UWS spray evaporation rate and synthetic Schlieren to visualize the liquid film evolution.

Due to the compact design requirement of the exhaust pipe and relatively long time scales of urea thermal decomposition [6, 7], the spray impingement on the exhaust pipe or on the mixer is unavoidable [8, 9]. According to Spiteri et al. [7], no more than 12% of the injected urea has decomposed 1.3 m downstream of the injection point (corresponding to a residence time of 0.05 s). UWS spray impingement on the exhaust manifold or on a deliberately introduced mixer can assist liquid evaporation and urea thermal decomposition on one side, on the other side leads to solid deposits such as urea, biuret, cyanuric acid, ammeline, ammeline and melamine [5, 10, 11]. The spray impingement results in local cooling of the exhaust pipe wall. When the wall temperature drops below a certain threshold, liquid film starts forming. Evaporation from the wall film leads to further cooling and results in increasing risk of deposit formation [12, 13]. Temperature-dependent impact regimes are

also responsible for the spatial distribution of the reducing agent. Currently, the main challenges for the implementation of mobile urea-SCR systems include rapid decomposition [14–17], homogeneous distribution of urea [18] and the mitigation of deposit formation [12, 19–26]. However, the SCR spray/wall heat transfer has been rarely studied. Birkhold [27, 28] underlines the importance of spray/wall interaction and includes it into his systematic modelling of UWS injection, where the implemented spray/wall interaction model was proposed by Kuhnke [29]. The spray/wall interaction classification map identified four regimes: deposition, splash, rebound and thermal breakup based on the kinetic properties of the droplets and the ratio of wall temperature to liquid saturation temperature [29]. According to Kuhnke, the critical temperature as the non-wetting threshold is 1.1 for a variety of fluids. Birkhold identified it rather at 1.4 (265 °C - 280 °C) for urea-water solution. However, to the knowledge of the author, heat transfer characteristic of UWS spray impingement have not been studied experimentally under exhaust flow conditions so far. The complexity of the SCR system requires a close look at the transient heat transfer behavior of UWS spray impingement in high temperature crossflows. The present study aims in making a contribution towards better understanding of these issues.

## 1.2 Literature Review

### 1.2.1 Fundamentals of pool boiling

Incropera et al. [30], summarize the different modes of pool boiling. Boiling is termed as the evaporation at a solid-liquid interface. The process occurs when the temperature of the surface exceeds the saturation temperature corresponding to the liquid pressure. The process is characterized by the formation of vapor bubbles, which grow and subsequently detach from the surface. Vapor bubble growth and dynamics depend on the excess temperature (the difference between the surface temperature and the saturation temperature), the nature of the surface, and the thermo-physical properties of the fluid, such as its surface tension.

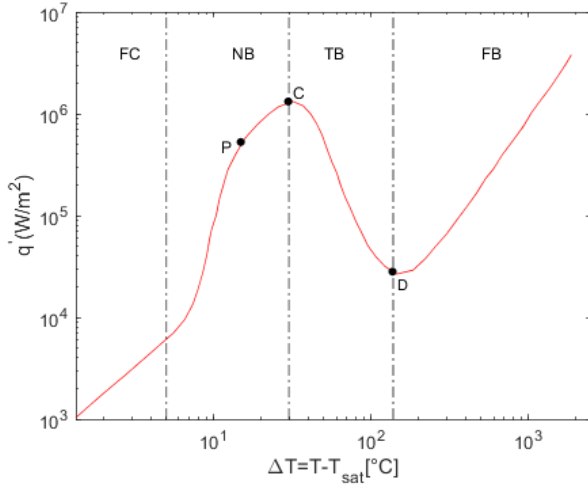


**Figure 1.2:** Typical boiling curve for water at 1 atm: surface heat flux as a function of excess temperature [30].

In turn, the dynamics of vapor bubble formation affect liquid motion near the surface and therefore strongly influence the heat transfer coefficient. An appreciation for the physical mechanisms may be obtained by examining the boiling curve. The heat flux depends on the convection coefficient and the excess temperature. Different boiling regimes may be delineated according to the excess temperature. Fig. 1.2 shows a typical boiling curve for water at 1 bar, as well as the boiling regimes [30].

**Free convection boiling** In this regime, fluid motion is determined principally by free convection effects. According to whether the flow is laminar or turbulent, the heat flux varies as a function of the excess temperature:  $q_s'' = f(\Delta T^{1.25...1.33})$ .

**Nucleate boiling** In this regime, bubbles form at nucleation sites and separate from the surface. Point P of Fig. 1.2 corresponds to an inflection in the boiling curve at which the heat transfer coefficient is maximal. The maximum heat flux in point C is termed the critical heat flux. For water at atmospheric pressure (1 atm) it exceeds  $1 \text{ MW/m}^2$ . At this point of maximum, considerable vapor

is being formed, making it difficult for liquid to continuously wet the surface. Heat convection coefficients exceeding  $10^4 \text{ W/m}^2\text{K}$  are characteristic of this regime.

**Transition boiling** Bubble formation is now so rapid that a vapor film begins to form on the surface. At any point on the surface, conditions may oscillate between film boiling and nucleate boiling. Because the thermal conductivity of the vapor is much less than that of the liquid, the heat flux must decrease with increasing excess temperature.

**Film boiling** At point D, referred to as the Leidenfrost point, the heat flux reaches the local minimum. The surface is completely covered by a vapor blanket. Heat transfer from the surface to the liquid occurs by conduction and radiation through the vapor. As the surface temperature is increased, radiation becomes more important and the heat flux increases with increasing excess temperature.

## 1.2.2 UWS droplet evaporation phenomena

The evaporation process of UWS droplets affects the thermal decomposition of urea, and thus the spatial distribution of the reducing agent. The heat needed comes from the heat transfer between exhaust gas flow and spray droplets or during the spray impingement on the hot boundary surfaces. The thermal decomposition of urea has not been studied in detail yet and therefore is poorly understood. Pure urea melts at  $133 \text{ }^\circ\text{C}$ . There is still a dispute on the state of urea (solid, liquid or gaseous) during and after the complete evaporation of water. Yim [2] stated liquid or gaseous urea, Schaber [11] reported that molten urea evaporates to gaseous urea above  $140 \text{ }^\circ\text{C}$ , but thermal decomposition to ammonia and isocyanic acid begins at  $152 \text{ }^\circ\text{C}$  and increases rapidly. Birkhold [28] and Koebel [1] pointed out that evaporation of water leads to solid or molten urea after the urea-water solution is injected into the hot exhaust gas stream. There have been a few fundamental investigations on the evaporation characteristics of a single UWS droplet on a heated plate or in a

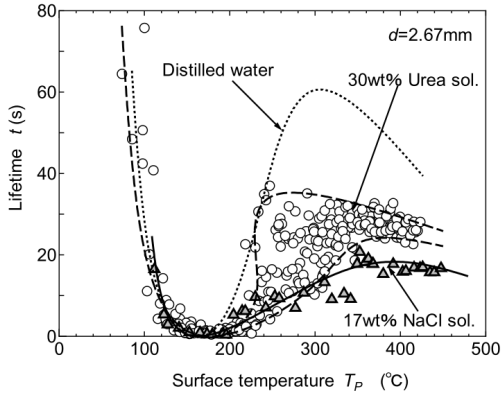


**Figure 1.3:** Evaporation characteristics of 30wt % urea-water droplets ( $d=2.67$  mm) on a heated surface [4].

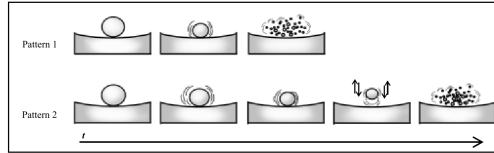


**Figure 1.4:** Illustrations of two patterns in the evaporation process [4].

heated furnace under quiescent conditions. Musa [4] measured the evaporation time of a 2.67 mm 10wt % or 30wt % urea water solution droplet on a heated surface and determined the evaporation time as a function of surface temperature (Fig. 1.3). As shown in Fig. 1.3, the curves of 30wt % urea solution are quite different to that of distilled water, especially in the transition and film boiling regions. Musa also discerned two different patterns during the evaporation process (Fig. 1.4), which were assumed to be caused by the very complex and diverse process of urea thermal decomposition [11, 15]. In real applications, the urea concentration of the droplets arriving at the hot surface should be larger than 32.5wt %. However, Musa did not study a higher concentration droplet or show the influence of the urea concentration on the droplet evaporation characteristics. Wang [5] investigated droplet evaporation by exposing comparatively large urea-water droplets on a quartz fiber to a quiescent air of high temperature. The measurements showed a two-

stage linear  $D^2$  reduction over time for most conditions, providing rate coefficients for UWS droplet evaporation as a function of initial droplet diameter and temperature. At high temperatures the droplets displayed micro-explosions. As the outer layer of water evaporated and local urea concentration increased, the urea on the droplet periphery crystalized to a sphere which prevented any further evaporation. The inner liquid then began to boil until the pressure build-up caused the droplet to burst. The extent to which this phenomena is found in real-world SCR systems is however unclear. At the end of water evaporation solid urea was seen, indicating that it firstly needs to melt and evaporate (or directly sublime) before urea decomposition can occur. These fundamental experimental studies have been very useful for simulation work on SCR sprays [31–37].

Grout [6] proposed a methodology to calculate the evaporation time of a spherical UWS drop in different aero-thermodynamic conditions. Drop size variation during the evaporation process can be modeled as a linear evolution of  $D^2$  over time as shown in the following equation.

$$D^2(t) = D_0^2 - \frac{4k}{L\rho_w}Nu(T_a - T_e)t = D_0^2 - \beta t \quad (1.7)$$

where  $k$  is the thermal conductivity of the surrounding gas,  $L$  the latent heat of evaporation,  $\rho_w$  the water density,  $Nu$  the Nusselt number in case of a moving evaporating droplet,  $T_a$  is the surrounding gas temperature,  $T_e$  the boiling temperature of UWS and  $t$  the time. The  $D^2$  evaporation law has been confirmed by the measurements of Musa [4] and Wang [5]. Grout used the following Nusselt number correlation from Sazhin [38]:

$$Nu = \frac{\ln(1 + B_T)}{B_T}(2 + 0.552Re_d^{0.5}Pr^{0.33}) \quad (1.8)$$

where  $B_T$  is the Spalding heat transfer number which compares the vapor heating energy to liquid vaporization energy,  $Re$  the droplet Reynolds number, and  $Pr$  the gas Prandtl number. Substituting Eq. 1.8 into Eq. 1.7, the evaporation rate  $\beta$  becomes:

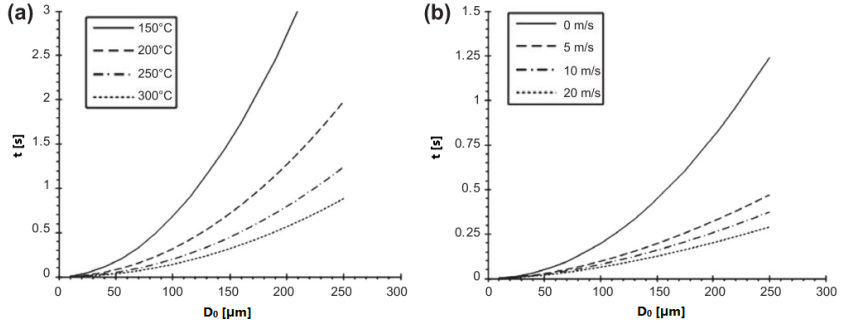


**Figure 1.5:** Water evaporation time calculated as a function of the initial drop diameter  $D_0$  for (a) several temperatures  $T_a$  in quiescent air and (b) several relative drop velocities in hot air of  $250^\circ\text{C}$  [6].

$$\beta = \frac{4k}{L\rho_w} \frac{\ln(1 + B_T)}{B_T} (2 + 0.552Re_d^{0.5}Pr^{0.33})(T_a - T_e) \quad (1.9)$$

Based on this model, Grout further calculated the time taken to completely evaporate water from an UWS drop, named water evaporation time  $t_e$ , by assuming different initial drop diameters and different flow conditions. The water evaporation time is shown as a function of initial drop diameter under various flow conditions in Fig. 1.5. At a fixed initial drop diameter, the evaporation is faster for a higher gas temperature and larger relative velocity. Considering a droplet of  $150\ \mu\text{m}$  and null relative velocity, the water evaporation time corresponds to a length of 3 m for typical automotive exhaust duct at gas flow conditions of  $250^\circ\text{C}$ ,  $6.67\ \text{m/s}$ .

### 1.2.3 Characteristics of UWS injection

The injection process of UWS determines initial conditions for the reducing agent, ammonia, distribution and therefore the efficiency of selective catalytic reduction (SCR) systems. The spray properties greatly influence urea decomposition time and thus the distribution of  $\text{NH}_3$ . If the  $\text{NH}_3$  distribution is non-homogeneous, the  $\text{NO}_x$  to  $\text{NH}_3$  ratio locally differs from the optimal ratio, resulting in ammonia slip as well as re-

duced NO<sub>x</sub> conversion. Several studies have examined these low pressure sprays [7, 28, 35, 39–49].

Fluid dynamic investigations of urea-water-solution sprays has been conducted in our laboratory recently, based on a specifically designed test rig which allows the reproduction of engine exhaust-similar conditions. The fluid-dynamic behavior of a 6-hole injector spray has been extensively investigated [35, 44, 45, 48], characterizing the macro spray properties. According to Spiteri [44], no secondary breakup occurs for this kind of low pressure sprays injected into the temperature elevated crossflow. Consequently, substantial wall impingement is inevitable under all conditions. The spray morphology and droplet size distributions under exhaust flow conditions have been used to validate numerical simulations [35, 45]. Concerning the spray sub-model, buoyancy plays a minor role and spray-wall interaction plays a crucial role under SCR operating conditions. Several models for the atomization process have been compared and the best agreement with experimental results has been achieved with a modified Rosin-Rammler model. The study evidences at low crossflow conditions two counter-rotating kidney vortices behind the spray core. These vortices entrain reflected droplets of the spray impinging on the channel floor, leading to improved mixing. The performance of the 6-hole pressure-driven injector described in [35, 44, 45] has been compared to that of an air-assisted injector in [7]. Distributions of urea and decomposition products were determined by high pressure liquid chromatography (HPLC). The urea distribution 1.3 m downstream of the air-assisted injector shows a comparatively homogeneous urea distribution in the horizontal direction and an inhomogeneous distribution vertically, with a higher concentration in the lower half of the channel. Up to this location thermal decomposition is low, no more than 12%. Fourier-transform infrared spectroscopy (FTIR) measurements downstream of a catalyst provided ammonia distributions as well as NO<sub>x</sub> reduction characteristics. The pressure-driven injector results in a highly inhomogeneous ammonia distribution downstream of the catalyst regardless of flow conditions, while the air-assisted injector improves homogeneity of ammonia in the downstream. Consequently, for identical



overall  $\text{NH}_3/\text{NO}_x$  ratios in the feed the pressure-driven injector results in lower  $\text{NO}_x$  conversion and higher  $\text{NH}_3$  slip with respect to the air-assisted injector.

Grout [6] studied the inclined injection of urea-water solution under conditions similar to diesel exhaust, although at weak gas flow. To visualize the liquid film formation during the spray impact a backlight imaging technique was used. At a fixed gas condition, the tendency of liquid film formation increases with the UWS mass flow rate due to the fact that the heat addition from the hot air stream to the wall does not balance the heat loss from the wall to the liquid. Below a critical temperature, liquid film formation starts. As liquid film evaporation occurs, the wall is further cooled. When water is fully evaporated, white solid deposits appear on the wall, increasing the surface roughness. The rough surface favours the liquid retention and leads to enhanced deposition. In addition, Mie scattering was applied to study the cross-sectional distribution of spray droplets. Based hereupon, the global spray evaporation rate was deduced taking into account that the scattered light intensity is proportional to the square of the droplet diameter and using a D-square evaporation law as stated in Eq. 1.7. The results were strongly dependent on the  $(I(t))/D(t)^2$  calibration. The spray evaporation rate was found to be  $0.1 \text{ mm}^2/\text{s}$ , at gas flow of  $42 \text{ kg/h}$  and  $246^\circ\text{C}$  and an UWS injection rate of  $0.0216 \text{ kg/h}$ . Oh [43, 50] applied the Mie scattering technique to visualize the spray patterns, and a Malvern instrument to measure the Sauter mean diameter (SMD) under atmospheric conditions. Spray patterns of a 3-hole injector show that the three spray cones are clearly distinguishable. The spray angle is  $15^\circ$  with very low variation. At an injection pressure of 5 bar, the spray flux is  $33.915 \text{ kg/h}$  and the SMD  $65 \mu\text{m}$ . A transparent exhaust channel system allowed the visualization of the spray spatial distribution under exhaust-similar flow conditions. The addition of a grid-channel plate-type mixer results in a more uniform distribution of the urea solution and a higher  $\text{NO}_x$  conversion efficiency in the downstream. The distance between the injector and the mixer is identified as the most critical factor affecting the mixer performance. Van Vuuren [42] used high speed imaging to visualize the

sprays of water and urea-water solution at different injector nozzle temperatures in quiescent air. Higher nozzle temperatures lead to a higher vapor fraction of the spray and a larger spray cone angle. At elevated temperatures, the spray is divided into a lower-velocity vapor dominated core and a higher velocity surrounding ring of small liquid droplets.

### 1.2.4 UWS spray impingement

Birkhold [27, 28] implemented a systematic model of the injection of urea water solution and the interaction with the exhaust gas flow and the exhaust pipe wall based on the spray/wall interaction model of Kuhnke [29] and the heat transfer description of Wruck [51]. It was shown that the liquid film formation related to the decrease of wall temperature. The Kuhnke model defines four different regimes, deposition, splash, rebound and thermal breakup, based on the following two dimensionless numbers which account for the thermo-physical properties of the droplets, the Mundo number  $K$  and the temperature ratio  $T^*$ .

$$K = \frac{(\rho D)^{0.75} U^{1.25}}{\sigma^{0.5} \mu^{0.25}} \quad (1.10)$$

where  $\rho$ ,  $D$ ,  $U$ ,  $\sigma$  and  $\mu$  denote the density, diameter, normal velocity, surface tension and dynamic viscosity of the droplets.

$$T^* = \frac{T_w}{T_{\text{sat}}} \quad (1.11)$$

$T^*$  is defined as the ratio of the wall temperature,  $T_w$ , to the liquid saturation temperature,  $T_{\text{sat}}$ .

Fig. 1.6 shows how the regime map is classified with these two parameters. According to Kuhnke [29], the critical transition temperature ( $T^*$ ) is 1.1 for a variety of fluids. Birkhold [27] found the critical temperature to be 1.4 (265-280 °C) for UWS, which was partly explained by the increasing saturation temperature with increasing urea concentration. It is clear that a shifting  $T^*$  to higher values corresponds to higher tendency for liquid film formation. The critical transition temperature is

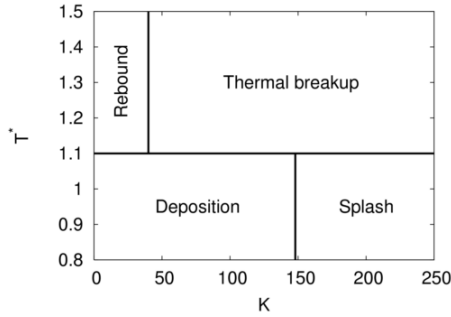


**Figure 1.6:** Spray/wall interaction regime map according to [29].

also known as the non-wetting threshold. As the spray cools down the surface, the wall temperature falls below the critical value and leads to deposition of droplets with low kinetic energy. Deposition of droplets leads to the formation of the liquid film and solid deposits which consist of urea, biuret, cyanuric acid, ammeline, ammeline and melamine [10]. Birkhold [27, 28] implemented a heat transfer model according to Wruck [51] which took into account the direct contact by two semi-infinite bodies, droplet and wall. The heat transferred by the droplets in a parcel was taken from a follow-up study by Meingast [52]:

$$Q = A_{\text{cont}} \frac{2\sqrt{t_{\text{cont}}}}{\pi} \frac{b_w b_d}{b_w + b_d} (T_w - T_d) \quad (1.12)$$

where  $A_{\text{cont}}$ ,  $t_{\text{cont}}$ ,  $T_w$ ,  $T_d$  denote the contact area, the contact time, the wall temperature and the droplet temperature.  $b$  is the heat penetration coefficient of the contact partners, which takes the following form:

$$b_i = \sqrt{(k\rho c_p)_i} \quad (1.13)$$

During impact, every droplet experiences a diameter expansion. The correlation for the maximum spreading diameter of the droplet during impact was found by Akao [53]. Birkhold [27] also measured temperatures of an impinged plate placed in the middle of a channel both with and without wall film formation and compared them with simulation results. The risk of wall film formation is highlighted. However, spray/wall

heat transfer can assist urea decomposition and improve mixture uniformity.

### 1.2.5 Spray impingement investigations in other contexts

Fuel spray impingement is an active field of research. Most studies are focused on visualization of spray impingement and measurement of droplet size and velocity before impact [54–56] or heat transfer analysis of spray impingement [57–63]. Arcoumanis [57] investigated diesel fuel sprays onto a uniformly heated plate and derived an empirical correlation for the transient spatially-resolved spray/wall heat transfer over a wide range of test conditions using phase Doppler anemometry (PDA) and fast thermocouples.

Most correlations for convective heat transfer take the general form:

$$Nu = aRe^bPr^c \quad (1.14)$$

Arcoumanis [57] introduced a correlation incorporating the Weber number, accounting for the dependency of spray/wall heat transfer on the extent of liquid spreading out over the surface. By applying dimensional analysis and fitting experimental results, the following correlation with an estimated uncertainty of  $\pm 23\%$  has been proposed.

$$Nu = 0.34 \frac{We^{0.94}}{Re^{0.53}Pr^{0.33}} \quad (1.15)$$

In a following work [60], the correlation for spray/wall heat transfer during impingement was extended to include the influence of crossflow. However, the experiments were conducted on an atmospheric test rig, which failed to include the droplet evaporation effect during the spray development. The Nusselt number correlation takes the following form:

$$Nu = 0.0012 \frac{Pr^{3.94}We^{1.59}}{Re^{1.89}} \left( \frac{U}{U + V_c} \right)^{-1.08} \left( \frac{D_{32}}{D_{32} + L_c} \right)^{-0.057} \quad (1.16)$$

where  $U$  is the droplet axial velocity,  $V_c$  the airflow velocity,  $D_{32}$  the Sauter mean diameter of droplets 30 mm downstream of the injector,

and  $L_c$  the distance between the injector and the impingement point. This correlation suggests a weak dependence of the wall heat transfer upon the crossflow velocity.

Heat transfer characteristics of water spray impingement on hot surfaces have been investigated in [64–70]. The dependency of the spray/wall heat transfer on the spray mass flux and the droplet diameter has been identified. Yao et al. [65] performed a dimensional analysis. The characteristic velocity (liquid mass flux over density) was introduced to define the spray Weber number ( $We_s$ ) as a measure of the spray inertia.

$$We_s = \frac{G^2 D}{\rho \sigma} \quad (1.17)$$

where  $G$  is the liquid mass flux,  $\rho$  the liquid density,  $D$  the characteristic length, and  $\sigma$  the surface tension. An empirical correlation of the Leidenfrost temperature based on the spray Weber number has been proposed.

$$T_{\text{Leidenfrost}} = 1400 We_s^{0.13} \quad (1.18)$$

On the other hand, Al-Ahmadi and Yao [71] presented correlations for the Leidenfrost and critical heat flux (CHF) points in function of the local mass flux for industrial nozzles with mass fluxes ranging from 1.7 to 30 kg/m<sup>2</sup>s. It has been highlighted that the Leidenfrost temperature, the Leidenfrost heat flux, the critical heat flux and the critical temperature are strongly dependent on the local spray mass flux.

$$T_{\text{Leidenfrost}}(^{\circ}C) = 536.8G^{0.116} \quad (1.19a)$$

$$q_{\text{Leidenfrost}}(kW/m^2) = 161.6G^{0.64} \quad (1.19b)$$

$$T_{\text{critical}}(^{\circ}C) = 296.4G^{0.2} \quad (1.19c)$$

$$q_{\text{critical}}(kW/m^2) = 1316G^{0.17} \quad (1.19d)$$

In general, such industrial nozzles produce relatively large droplets (350  $\mu\text{m}$ ) of moderate velocities (13–15 m/s) [66]. In addition to the water impact flux, Wendelstorf et al. [66] introduced the temperature

difference between the surface and the liquid in the analytic correlation of the heat transfer coefficient.

Moreover, several studies revealed that the critical heat flux, the Leidenfrost temperature and the critical heat flux temperature are positively correlated with the mass flux [67, 68, 70] and negatively correlated with the droplet diameter [67, 70]. Estes and Mudawar [67] provided correlations of the critical heat flux to the spray mass flux and the Sauter mean diameter (SMD) for full cone sprays. For sprays with a local mass flux of  $30 \text{ kg/m}^2\text{s}$  and a SMD of  $150 \text{ }\mu\text{m}$ , for instance, the CHF reaches about  $1 \text{ MW/m}^2$ . Jia et al. [68] conducted experiments with a multi-nozzle spray system which provided variable mass fluxes ranging from  $0.156$  to  $1.20 \text{ kg/m}^2\text{s}$  and droplets around  $30 \text{ }\mu\text{m}$ . According to [68], the critical heat flux is about  $2 \text{ MW/m}^2$  at  $1.2 \text{ kg/m}^2\text{s}$  for water spray cooling. In parallel, the critical heat flux temperature increases almost linearly with the mass flux, being  $145 \text{ }^\circ\text{C}$  at  $1.2 \text{ kg/m}^2\text{s}$ . The addition of sodium dodecyl sulfate in water broadens the critical heat flux temperature range. However, the exact reason of the broadening is not clear. Dou et al. [70] confirmed the influence of water mass flux on the Leidenfrost temperature and critical heat flux. Increase in water injection pressure (leading to smaller droplets) shifts the critical heat flux and Leidenfrost points to higher temperatures. Empirical correlations for the critical heat flux and the transition boiling regime have been obtained as a function of the Sauter mean diameter, the local water flux, the surface temperature, and the physical properties of water and vapor [70]. For sprays with a water injection pressure of  $5 \text{ bar}$  and local mass flux of  $10 \text{ kg/m}^2\text{s}$ , the critical heat flux is found to be  $1 \text{ MW/m}^2$ .

In addition, the influence of spray inclinations on the heat transfer characteristics has been examined [71]. The Leidenfrost temperature and the minimum heat flux with inclined sprays are generally higher than that with the vertical sprays. This is due to the combined effect of mass deposition of spray and overflow from the upstream liquid film. The overflow from the plate causes transition boiling to start at a higher surface temperature. Due to the overflow, the minimum heat flux with inclined spray is higher than the one with a vertical spray. The heat

flux in the nucleate boiling region is not a strong function of the spray mass flux and little effects from the spray angle are observed. This insensitivity to the spray conditions is fairly similar to the behavior of the nucleate boiling heat transfer at forced convection.

## 1.3 Thesis outline

In state-of-the-art exhaust systems, the UWS spray/wall interaction is of paramount importance for mixing urea with exhaust flow and transferring heat to the UWS droplets which in turn is decisive for urea evaporation and thermolysis and the performance of the SCR catalyst and the entire system. UWS spray impingement on different surfaces (a specifically designed mixer or the exhaust pipe) on one side can assist liquid evaporation and urea decomposition; on the other side may lead to deposit formation. This is due to the fact that spray impingement results in local cooling of the exhaust pipe wall. When the wall temperature drops below a certain threshold, droplets deposit and liquid film starts forming. The temporal evolution and spatial distribution of the liquid film and the different species it contains is temperature dependent, as well as under the influence of the periodically impinging sprays. Varying local temperatures lead to different impact regimes. The different spray/wall interaction regimes as well as the boundaries are not clear and only recently first attempts for their description have been published. Evaporation from the wall film leads to further cooling and increasing risk of solid byproducts formation. However, the heat transfer phenomena involved during the spray impingement process are not yet well-understood. The present thesis is a comprehensive experimental analysis of SCR spray/wall interaction phenomena. The emphasis lies on the spray/wall heat transfer under the presence of substantial crossflow and local evaporation. To our knowledge so far, related phenomena have been investigated for fuel sprays [57, 60] where the momentum of the spray is significantly larger than that of the SCR sprays investigated in this study. Some additional studies [65, 68, 70, 71] analyzed the liquid spray cooling of metals at high temperatures. In these cases, no gaseous crossflow has been taken into account.

In the present thesis, following aspects have been investigated in detail:

1. High speed imaging and analysis have been conducted in order to identify the phenomena associated with the impingement process, such as liquid film formation and evolution, urea crystallization



and deposit formation. Solid deposits have been analyzed by nuclear magnetic resonance spectroscopy. (Chap. 2)

2. The impinging spray mass flux distributions have been quantified. The influence of entrainment and evaporation on the impinging mass flow rate has been examined independently. Phase Doppler Anemometry measurements characterized the impinging droplet size distributions under various conditions, thus showing the impact of entrainment and evaporation in respect of droplet sizes. (Chap. 2)
3. Four commercially available injectors have been described and compared in detail in terms of the bulk spray analysis, droplet size and velocity distributions. (Chap. 3)
4. A comprehensive experimental analysis of the heat transfer characteristics of a single UWS spray impingement on a wall with stable thermal boundary conditions under typical diesel exhaust flow conditions has been conducted. The temperature distribution on the non-impinged, rear surface of a stainless steel plate has been measured by infrared thermography. The spray cooling heat fluxes have been obtained by solving the 1D inverse heat conduction problem. The resulting temperatures have been used for assessing the heat extracted from the wall. Phase Doppler Anemometry (PDA) measurements from Chap. 3 provided information on the kinetic properties of the impinging droplets. The surface temperatures in combination with the droplet kinetic properties have been used to determine the spray impingement regimes. (Chap. 4)
5. IR thermographic imaging on the rear side of a plate impinged by subsequent injection events has been performed to describe the intrinsic heat transfer characteristics of the urea-water spray impingement. The specific focus was the identification of different boiling regimes, the critical heat flux and Leidenfrost points. Thermal analysis of the spray-impinged surface involved 3D com-

putation of the inverse transient heat conduction by applying the sequential function specification method. (Chap. 5)

To our knowledge, there are so far no such detailed investigations of the wall impingement of SCR sprays in exhaust configurations. Based on these results, injection strategies, exhaust geometries and materials can be assessed in providing adequate evaporation and component mixing for SCR operation. Finally, results of this study offer versatile possibilities to calibrate and validate numerical codes.

## 2 Phenomenology and quantitative characterization of the urea-water spray impingement

Parts of this chapter are published in: Y. Liao, P. Dimopoulos Eggenchwiler, D. Rentsch, F. Curto, and K. Boulouchos, "Characterization of the urea-water spray impingement in diesel selective catalytic reduction systems," *Applied Energy*, vol. 205, pp. 964-975, 2017.

### Abstract

Exhaust after-treatment selective catalytic reduction (SCR) systems based on urea-water solution are state-of-the-art technologies mitigating NO<sub>x</sub> emissions for diesel and lean combustion systems. Major challenges for implementing the systems are high NO<sub>x</sub> reduction performance, uniform mixture formation and avoiding solid deposits formation. This study presents a detailed analysis of the urea-water spray impingement which leads to deposit formation, affecting ammonia distribution and catalytic performance. High speed images provide detailed information of the impingement process. Moreover, impinging spray mass flux distribution and droplet size distribution have been quantified under typical diesel exhaust flow conditions. The work has been performed with a commercial 3-hole pressure-driven injector dosing into a flow channel.

At gas flow conditions of 300 °C, 200 kg/h, only 35.6 % of the injected fluid impinges on the opposed wall due to entrainment and evaporation.

The entrainment level has been found to scale logarithmically with the gas flow momentum, related correlations are provided. Having an integrated analysis of a mechanical patternator and non-intrusive Phase Doppler Anemometry (PDA) results, it is concluded that droplets below 20  $\mu\text{m}$  are completely entrained or evaporated. The impingement rate is gradually increasing with increasing droplet diameter up to 90  $\mu\text{m}$ , and almost all larger droplets reach the opposed wall. Optical visualization experiments show liquid film formation, film transport, liquid accumulation, nucleate boiling, urea crystallization and melting, thin film evaporation prior to solid deposit formation. The spray impingement leads to liquid film formation. Relevant dimensions have been evaluated with digital image processing. Direct relationship of liquid accumulation to the solid deposit formation has been identified. The permanent solid deposit is consisting of cyanuric acid, biuret, ammeline and ammeline as identified by nuclear magnetic resonance spectroscopy.

## 2.1 Introduction

Diesel engines relying on lean combustion are widely used in the transportation sector due to their high energy conversion efficiency. Concerning heavy duty applications, freight transport and mobile machines, there are no potential alternatives to diesel engines in the next decades. However, they produce harmful pollutants, such as NO<sub>x</sub> and particles. NO<sub>x</sub> is one of the major and most harmful environmental pollutants induced by the transportation sector. They lead to acid rain and formation of ground level ozone, which leads to health and environmental problems. Methods to reduce NO<sub>x</sub> emissions include in-cylinder techniques and exhaust after-treatment systems. In-cylinder techniques which aim to lower peak temperatures tend to decrease engine efficiency and increase soot formation. Therefore, exhaust selective catalytic reduction (SCR) systems are currently the promising technique to reduce NO<sub>x</sub> emissions without sacrificing engine efficiency [1]. SCR systems rely on injection of ammonia precursor in the exhaust gas. In real applications, 32.5 % urea-water solution (UWS, trademark AdBlue) is used as an am-

monia precursor because of its non-toxicity and lowest freezing point. The UWS injection is followed by the evaporation of water from spray droplets. Thereafter, thermal decomposition of urea and hydrolysis of isocyanic acid take place [1, 28, 72], resulting in the production of ammonia. Ammonia reacts with NO<sub>x</sub> to water and nitrogen.

The main challenges for the implementation of mobile urea-SCR systems include homogeneous distribution of urea [14, 15, 18] as well as mitigation of solid deposit formation [12, 19, 73]. Due to these, there are increasing efforts for alternative reducing agent precursors, such as hydrocarbons [74–76] or ammonium formate [77, 78]. However, urea-SCR is the state-of-the-art technology for mobile applications. Because of compact design requirements of the exhaust pipe and relatively long time scales of urea thermal decomposition [7], the spray impingement on the exhaust pipe or on a mixer is unavoidable [28, 79]. As the wall temperature drops below a certain threshold, liquid film starts forming [27]. Evaporation from the wall film leads to further cooling and increasing risk of deposit formation such as cyanuric acid, biuret, ammeline etc. [10, 11, 80].

In the field of UWS spray impingement, two kinds of studies exist in the literature: single droplet evaporation/impact [4–6] or numerical simulation of the spray/wall impact [27–29]. However, there is a lack of experimental investigations of the spray impingement. The spray impingement has been studied in diverse applications, like fuel spray impingement [81–83], steel quenching [84] and electronics cooling [85]. Previous studies have indicated that, the impingement density has the highest influence on the spray impingement heat transfer [69, 71, 84, 86].

The present paper is a systematical investigation of the UWS spray impingement process under diesel-typical conditions. The impingement process is described both qualitatively and quantitatively. The impinging spray mass flux distributions were quantified by using a mechanical patternator. Phase Doppler Anemometry (PDA) was applied to characterize the impinging droplet size distributions under various conditions. Optical visualization experiments were conducted to observe the phenomena associated with the impingement process, such as liquid film

formation, urea crystallization and deposit formation. Solid deposits were analyzed by nuclear magnetic resonance spectroscopy. Results of this study provide new insights into the UWS spray impingement process which can be used for the lay-out of efficient after-treatment systems, and offer ample possibilities for validating numerical simulations.

## 2.2 Experimental setup and methods

Measurements were conducted in a flow lab, which was designed for the experimental investigation of SCR sprays. In the present work, a commercial 3-hole SCR injector was mounted on the top of the measurement chamber, 50° inclined to the gas flow direction. It was a pressure-driven injector with three 190 μm nozzle holes arranged evenly on a 1.9 mm diameter ring. The injection pressure was regulated to 9 bar.

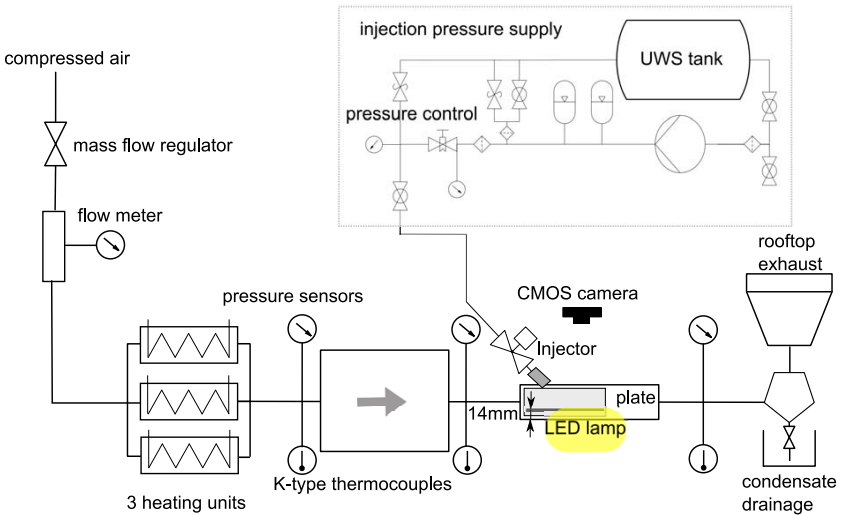


**Figure 2.1:** Schematic diagram of the flow lab with the optical film visualization setup

**Optical film visualization** experiments have been performed to study the phenomena associated with spray impingement on the plate under various exhaust-typical conditions. The stainless steel plate, having an averaged surface roughness of 0.5 μm, was placed 14 mm (mea-

sured from the front surface) above the channel bottom as shown in Fig. 2.1. The impinging plate had a dimension of 200 mm×80 mm and a thickness of 4 mm. The impingement processes were captured by a high speed CMOS camera (Casio EX-FH100) working at 30 frames per second at a resolution of 640×480 pixels. The camera was mounted vertically 352 mm upwards of the impinged plate. The illumination was provided by a LED lamp covered by a milk glass to diffuse light. For all visualization experiments, the injection frequency was set to 1 Hz, while two different injection durations were studied: 60 ms and 120 ms. The total number of injections was limited to 150. Adblue (32.5% urea-water solution) was used as the injection fluid.

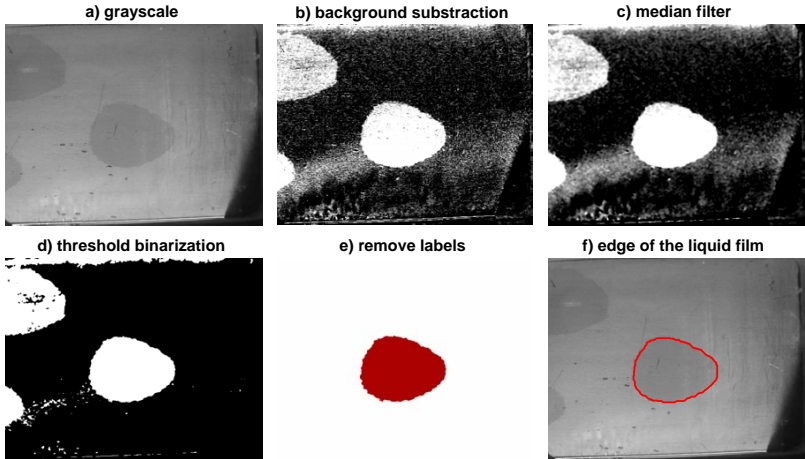


**Figure 2.2:** Image processing for extracting the liquid film area

**Image processing** was conducted in Matlab for determining the liquid film area. RGB images were firstly converted to grayscale images. The spatial intensity distribution of the grayscale images was corrected by subtracting the background image (one image before injection) as shown in Fig. 2.2b. Median filtering ( $5 \times 5$ ) was applied to the corrected images to remove the small features on the plate. The processed images were binarized by a threshold value, thus separating the wetted area from the plate (Fig. 2.2d). Thereafter, every connected region was at-

tributed to a label and only the pixels at the front cone region were kept (Fig. 2.2e and f).

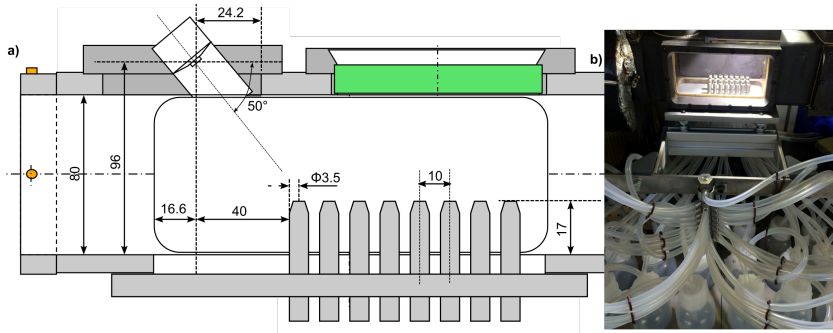


**Figure 2.3:** Schematic drawing of the patternator integrated in the flow channel

**Patternator** is an in-house developed instrument for measuring spray volume flux distributions. A perforated plate with 24 probes, each of which is connected to a PVC bottle through a silicon hose, was pressed against the channel tightly. A vacuum pump is linked to all collecting bottles through a distributor to create a slight suction for avoiding the capillary effect in the hoses. The 24 probes were arranged in three rows of 8 probes each as shown in Fig. 2.3. The probe matrix has a spacing distance of 10 mm in the flow direction and 15 mm in the transversal direction. Each probe has an inner diameter of 5 mm. To refine the measurement grid, the flow channel was traversed on a two-axis sliding system, while the patternator was fixed on the working table. In this manner, a resolution of  $2\text{ mm} \times 2\text{ mm}$  was obtained. Each data point was collected over 1700 injections. The injection strategy was set to 3 Hz of 150 ms to speed up the measurement. The injected fluid is demineralized water to avoid blockages in the hoses or probes. The mass flux displayed in the results and discussions section is calculated as follows:

$$\dot{M} = \frac{m}{nt_{inj}A} \quad (2.1)$$



where  $\dot{M}$  is the mass flux,  $m$  the total mass collected per probe,  $n$  the number of injections collected,  $t_{inj}$  the duration of each injection and  $A$  the probe tip opening area.

In order to decouple the influence of entrainment and evaporation on the impinging mass fluxes, patternator measurements were performed under iso-temperature and iso-momentum flow conditions as indicated in Tab. 2.1. For iso-momentum conditions, gas flow momentums were kept the same as that of 200 kg/h flow at 20 °C. Therefore, flow rates had to be adjusted at elevated temperatures as follows:

$$\frac{\dot{m}}{\dot{m}_{amb}} = \sqrt{\frac{\rho(T)}{(\rho(T_{amb}))}} \quad (2.2)$$

where  $\dot{m}$  is the gas mass flow rate,  $\rho$  the gas density and  $T_{amb}$  denotes 20 °C. The corrected flow rates are shown in Tab. 2.1.

	Iso-temperature conditions			
$T$ [°C]	20	20	20	20
$\dot{m}$ [kg/h]	0	100	200	300
$v$ [m/s]	0	3.6	7.2	10.8
$\rho v^2$ [kg/ms <sup>2</sup> ]	0	15.7	62.5	141.4
	Iso-momentum conditions			
$T$ [°C]	150	200	300	400
$\dot{m}$ [kg/h]	167	157	143	132
$v$ [m/s]	8.6	9.1	10.1	10.9
$\rho v^2$ [kg/ms <sup>2</sup> ]	62.5	62.5	62.5	62.5

**Table 2.1:** Gas flow conditions during the patternator measurements

**<sup>1</sup>H and <sup>13</sup>C nuclear magnetic resonance** (NMR) spectra were recorded at 400.1 and 100.6, respectively on a Bruker Avance III 400 NMR spectrometer (Bruker Biospin AG, Faellanden, Switzerland). The sample analyzed by NMR were the solid deposits, which were collected from the plate after the optical experiment under the condition of 300 °C, 100 kg/h and 1 Hz of 120 ms. The NMR experiments were performed at

298 K using the Bruker standard pulse programs and parameter sets on a 5 mm CryoProbe<sup>TM</sup> Prodigy probe equipped with z-gradient applying 90° pulse lengths of 11.4 μs (<sup>1</sup>H) and 10.0 μs (<sup>13</sup>C). The <sup>13</sup>C NMR spectra were recorded applying power gated <sup>1</sup>H decoupling using 30° excitation pulses and relaxation delays of 1 s allowing a good signal to noise ratio of the minor components in a relatively short experimental time (up to 1 day of measurement time).

comp.	urea	biuret	triuret 1 <sup>st</sup>
formula	$CH_4N_2O$	$C_2H_5N_3O_2$	$C_3H_6N_4O_3$
MW [g/mol]	60.056	103.081	146.106
$\delta^{13}C$ [ppm]	162.8	164.4	162.9
No.(C)	1	2	2
comp.	triuret 2 <sup>nd</sup>	ammelide 1 <sup>st</sup>	ammelide 2 <sup>nd</sup>
formula	$C_3H_6N_4O_3$	$C_3H_4N_4O_2$	$C_3H_4N_4O_2$
MW [g/mol]	146.106	128.091	128.091
$\delta^{13}C$ [ppm]	161.9	169.1	166.1
No.(C)	1	1	2
comp.	melamine	cyanuric acid	
formula	$C_3H_6N_3$	$C_3H_3N_3O_3$	
MW [g/mol]	126.123	129.075	
$\delta^{13}C$ [ppm]	166.7	167.2	
No.(C)	3	3	
comp.	ammeline 1 <sup>st</sup>	ammeline 2 <sup>nd</sup>	
formula	$C_3H_5N_5O$	$C_3H_5N_5O$	
MW [g/mol]	127.107	127.107	
$\delta^{13}C$ [ppm]	171.6	168.3	
No.(C)	1	2	

**Table 2.2:** Molecular formulae and weights, <sup>13</sup>C NMR chemical shifts and no. of carbons contributing to signal intensities of all chemical species possibly present in solid deposit samples

Although the recording conditions were not really quantitative, we observed only small deviations from an experiment where we applied 30 s

relaxation delays. The NMR chemical shifts ( $\delta$ ) were calibrated to the  $^1\text{H}$  NMR resonance at 4.79 ppm in the case of  $\text{D}_2\text{O}/\text{NaOD}$  solutions and  $^{13}\text{C}$  chemical shifts were calibrated externally to the signal of tetramethylsilane at 0.0 ppm. Since a considerable dependency of resonance positions on pH values and concentrations were observed, signal assignments of individual resonances were performed by addition of small amounts of all possible chemical species (urea, biuret, triuret, cyanuric acid, ammeline, ammeline or melamine [10]) to the sample solution of interest. From a line shape analysis of the  $^{13}\text{C}$  NMR spectra the relative amounts of all individual resonances were determined by non-linear least-square fits of all signals of interest using the line shape simulation software 'DMFIT' [87]. Subsequently, the sample composition can be evaluated using the following equations, where  $Int(i)$  is the relative signal intensity of species  $i$ , 'No.(C)' the number of carbons contributing to the signal and  $MW(i)$  the molecular weight of the individual species (see Tab. 2.2):

$$x(i) = \frac{\frac{Int(i)}{No.(C)} * MW(i)}{\sum \frac{Int(i)}{No.(C)} * MW(i)} [wt/wt - \%] \quad (2.3)$$

## 2.3 Results and Discussion

### 2.3.1 Impinging spray mass flux distributions

The 3-hole injector has been completely characterized using the mechanical patternator. Measurements were performed within a rectangular field, 84 mm in the flow direction  $x$  and 65 mm in the transversal direction  $z$  under ambient conditions ( $20^\circ\text{C}$ ,  $0\text{ kg/h}$ ) and under exhaust-typical conditions. The coordinates indicated in Fig. 2.4 to Fig. 2.5 are the distances from the injector nozzle exit along  $x$  and  $z$  directions. Detailed spatially-resolved mass flux distribution provided in Fig. 2.4 reveals that there are three distinct impingement regions, each corresponding to one hole of the injector. This coincides with the spray footprints as shown in Fig. 2.10. The spray patterns produced by each hole of the injector are slightly different, and the highest impingement rate  $0.0212\text{ kg}/(\text{mm}^2\text{h})$  is found in the upstream spray cone. The acquired data points were fitted

using the cubic interpolation function and integrated within the whole field, which resulted in an impingement rate of 7.44 kg/h. The nominal injection rate, which is estimated by collecting the injected mass over 3000 injections, is 7.02 kg/h. It means that the patternator method produces an error of 6 % in the impingement rate.

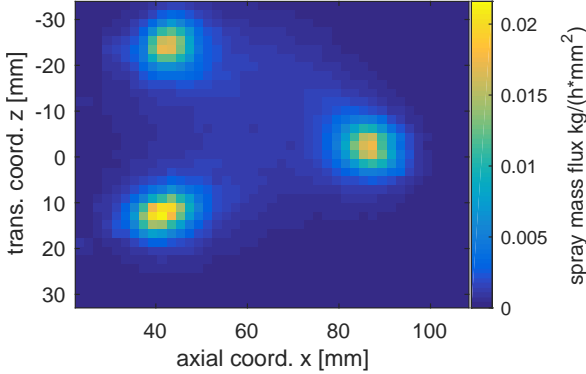


**Figure 2.4:** Mass flux distribution with a resolution of  $2\text{ mm} \times 2\text{ mm}$  on the plane 79 mm apart from the injector nozzle exit at ambient conditions ( $20\text{ }^\circ\text{C}$ ,  $0\text{ kg/h}$ ).

The spray dispersion characteristics are quantified in Tab. 2.3, showing the sizes of the areas. 90 % of the total impinged volume is contained in a region of  $2337.9\text{ mm}^2$ , which gives an average film thickness of  $119\text{ }\mu\text{m}$  for a single injection under the assumption that all droplets are deposited on the impinged plate. 50 % of the total volume is contained in an area of  $385.8\text{ mm}^2$ , 90 % of  $2337.9\text{ mm}^2$ , which indicates that the spray flux is concentrated in the core and fades out quickly towards the periphery.

Percentage of the total mass	20 %	50 %	75 %	90 %
Area at ambient [ $\text{mm}^2$ ]	86.3	385.8	1276.6	2337.9
Area at $300\text{ }^\circ\text{C}$ $200\text{ kg/h}$ [ $\text{mm}^2$ ]	53.4	181.1	384.4	663.3

**Table 2.3:** Area occupied by different mass fraction at ambient conditions and at  $300\text{ }^\circ\text{C}$ ,  $200\text{ kg/h}$ .

The mass flux distribution at ambient conditions serves as a reference case, while mass flux distributions under exhaust typical condi-

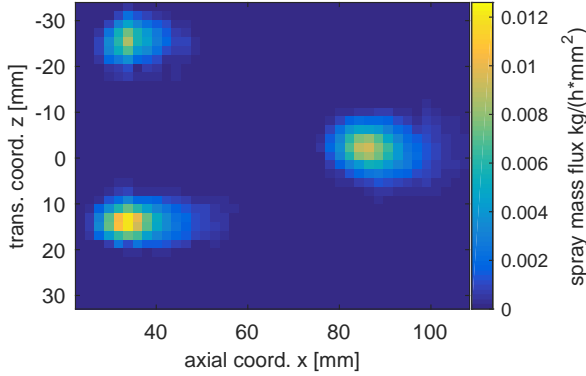


**Figure 2.5:** Mass flux distribution with a resolution of  $2\text{ mm}\times 2\text{ mm}$  on the plane  $79\text{ mm}$  apart from the injector nozzle exit at the flow condition of  $300\text{ }^\circ\text{C}$ ,  $200\text{ kg/h}$ .

tions are of more significance for real applications. The set of 1505 mass flux measurements at flow condition of  $300\text{ }^\circ\text{C}$  and  $200\text{ kg/h}$  is displayed in Fig. 2.5. The three distinct spray cones are clearly identified in Fig. 2.5, while the peak flux in the upstream cone decreases for  $44\%$  to  $0.0119\text{ kg}/(\text{mm}^2\text{h})$ . Moreover, the small droplets in the spray periphery are completely entrained by the gas flow. The sizes of the regions enclosing  $20\%$ ,  $50\%$ ,  $75\%$  and  $90\%$  of the total injected volume at  $300\text{ }^\circ\text{C}$   $200\text{ kg/h}$  are provided in Tab. 2.3. The spray is getting less dispersed compared to that at ambient conditions. The periphery of the spray is more affected by the gas flow than the spray center.

The dispersion characteristics are quantified in Fig. 2.6, showing non-normalized probability density functions (PDF) and cumulative distribution functions (CDF) of the mass flux measurements at ambient and elevated flow conditions. At ambient conditions, mass flux values range from  $0$  to  $0.0212\text{ kg}/(\text{mm}^2\text{h})$ , with an average of  $0.0013\text{ kg}/(\text{mm}^2\text{h})$  and a standard deviation of  $0.0026\text{ kg}/(\text{mm}^2\text{h})$ , while at an elevated flow condition mass flux measurements range from  $0$  to  $0.0119\text{ kg}/(\text{mm}^2\text{h})$ , with an average of  $0.0012\text{ kg}/(\text{mm}^2\text{h})$  and a standard deviation of  $0.0021\text{ kg}/(\text{mm}^2\text{h})$ . For the elevated flow condition, integrating the mass flux measurements over the total area gives an impingement rate of  $2.50\text{ kg/h}$ . The mass reduction of  $64.4\%$  compared to the nominal injection rate is

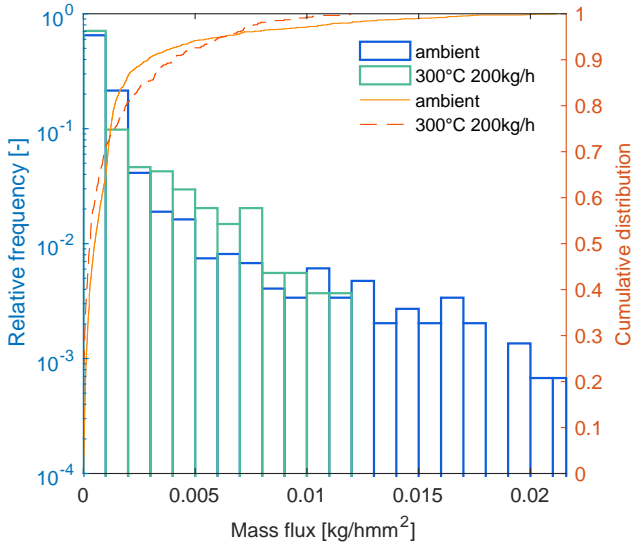


**Figure 2.6:** Relative frequency and cumulative distribution of mass flux measurements at ambient conditions and at the flow condition of 300 °C 200 kg/h.

due to the droplet entrainment by the gas flow and the droplet evaporation in the gas flow. The spray entrainment and evaporation are quantified and correlated as a function of gas flow momentum and gas flow temperature respectively as indicated in Fig. 2.8 and Fig. 2.9.

Having evidenced an impinging mass reduction due to entrainment and evaporation, droplet size distributions (ambient and 300 °C, 200 kg/h) have been compared to understand the influence of entrainment and evaporation on the impinging droplets depending on the diameter. For the comparison, the non-normalized impinging droplet PDF for the 300 °C, 200 kg/h case is multiplied by a scaling factor of 0.608, which is the ratio of the impinging mass flow rate of the 300 °C, 200 kg/h case to that of ambient conditions. It is derived by integrating the patternator measurements over the same domain as the PDA measurement region. The difference of these two PDF distributions represents the mass reduced by the flow (both entrainment and evaporation) for each diameter class as displayed in Fig. 2.7. The hot flow influences mainly droplets below 90  $\mu\text{m}$ , while its influence on bigger droplets is weak. From the CDFs

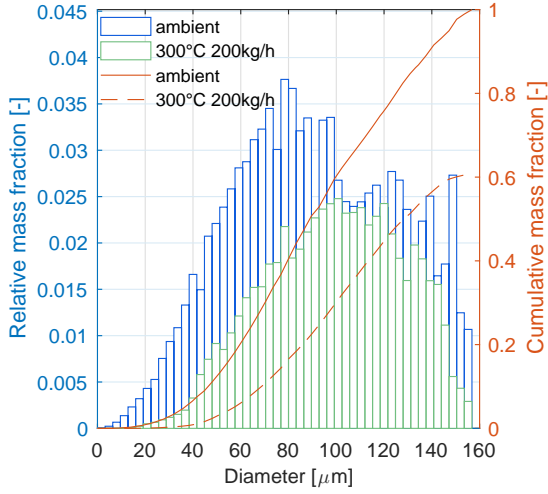


**Figure 2.7:** Droplet mass distributions at ambient conditions and at the flow condition of 300 °C 200 kg/h.

on the right-hand axis, the cumulative mass difference for droplets below 90  $\mu\text{m}$  is 0.283, whereas the total difference is 0.392 (1 - the scaling factor). Moreover, the impinging mass percentage (the impinging mass of the 300 °C, 200 kg/h case to that of ambient conditions) is gradually increasing with increasing diameter for droplets less than 90  $\mu\text{m}$ . For droplets below 20  $\mu\text{m}$ , the hot flow entrains or evaporates almost everything, whereas 60 % of the mass is still impinging from droplets between 73  $\mu\text{m}$  and 90  $\mu\text{m}$ .

To determine the spray entrainment ratio as a function of gas flow momentum, the gas flow was kept at non-evaporating conditions for this series of measurements. The flow temperature was set to 20 °C and the flow rate was varied from stagnant, to 100 kg/h, 200 kg/h, and 300 kg/h. The blue points in Fig. 2.8 show the reductions in the impingement rates, integrated over a rectangle area of the same size around the spray peak, for different gas flow momentums. The red curve is a fitted logarithmic function, which takes the following form:

$$Ent = 0.04735 \cdot \ln(0.8323 \cdot \rho v^2 + 1) \quad (2.4)$$

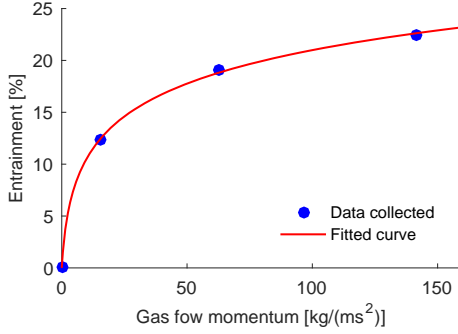


**Figure 2.8:** Entrainment as a function of momentum.

$Ent$  denotes the entrainment level and  $\rho v^2$  is the gas flow momentum. R-squared of this fit is 0.9995.

To evaluate the spray evaporation portion as a function of gas flow temperature, the gas flow momentum was kept constant at  $62.5 \text{ kg/ms}^2$ . The flow temperature was increased from ambient to  $400 \text{ }^\circ\text{C}$ . Fig. 2.9 indicates the impingement mass reduction for the various flow temperatures. The green dots were obtained by subtracting the entrainment level (19.13%) at  $62.5 \text{ kg/ms}^2$  from the overall reductions. The fitted function takes the following form:

$$Eva = 0.006331\sqrt{(T - 100)} + 0.1886 \quad (2.5)$$

$Eva$  denotes the evaporation resulting mass reduction and  $T$  the gas flow temperature. The spray is characterized by a wide range of droplets from 0 to  $160 \text{ }\mu\text{m}$ . Smaller droplets are more likely to be entrained and evaporated. The diameter of the smallest droplet after breakup that still reaches the plate is denoted as the critical evaporation or entrainment diameter. Assuming a sphere evaporation model in hot surroundings, the critical evaporation diameter scales with the square root of the temperature difference between the gas flow temperature and the liquid saturation temperature. However, droplets which are initially evaporated below the critical entrainment diameter can be entrained by the gas flow as well. The green part in Fig. 2.9 is rather a co-influence by both en-



tainment and evaporation, referred as evaporation resulting impinging mass reduction.

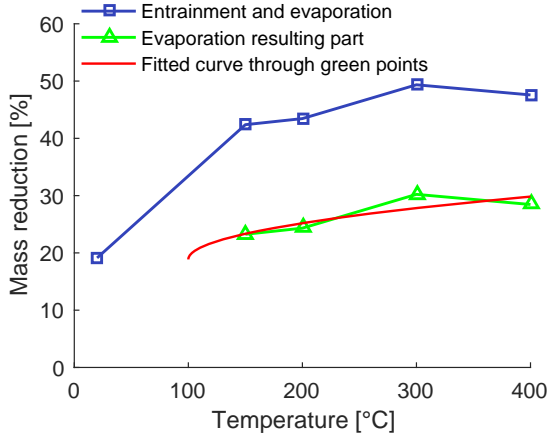


**Figure 2.9:** Evaporation as a function of temperature.

### 2.3.2 Spray impingement phenomenology

Optical high speed camera experiments have been performed in order to analyze the spray impingement behavior. The gas flow condition for results shown in Fig. 2.10 to Fig. 2.17 is 300 °C and 100 kg/h. SOI stands for the time instant of the start of the first injection, whereas EOI denotes the time instant of the end of the last injection.

Following the first injection the spray impinges on the hot plate (plate temperature similar to the flow temperature, i.e. 300 °C), resulting in three separate liquid film areas, as shown in Fig. 2.10a. The spray/wall interaction behavior is dominated by rebound and thermal breakup as long as the plate temperature remains above 280 °C (according to [27, 29]). This is strongly evidenced by the white smoke emerging in the downstream of the three impingement areas in Fig. 2.10a, consisting of urea enriched rebounding droplets, since water has partly evaporated during impingement. During each injection (duration 120 ms) the liquid film area increases, reaching a maximum shortly after the end of this injection. Thereafter, in the remaining 880 ms until the next injection starts, the liquid film retracts to a minimum. However, the liquid

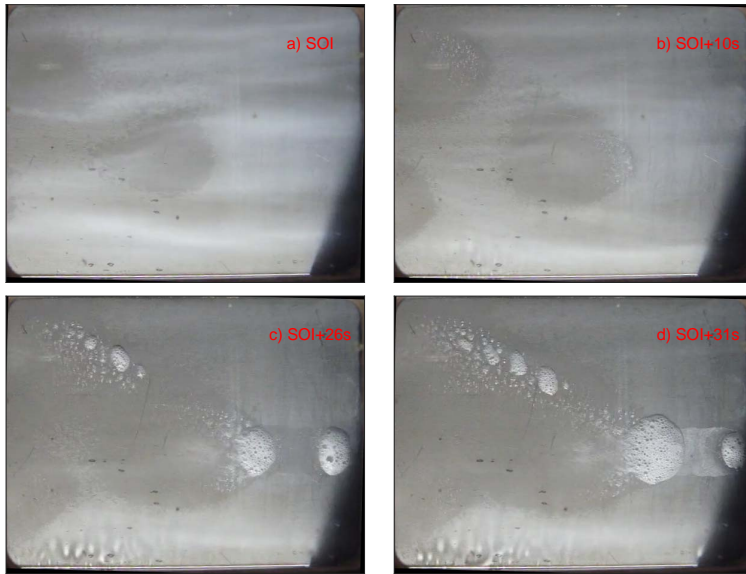


**Figure 2.10:** First stage of impingement (flow conditions: 300 °C, 100 kg/h, injection 1 Hz of 120 ms for 150 s).

film areas increase from injection to injection (Fig. 2.10b) leading after roughly 20 injections to a merging of the three films as can be seen in Fig. 2.10c. This evidences that evaporating liquid between two injections is significantly less with respect to the impinging liquid during injection.

Local evaporation is evidenced as bubble formation in Fig. 2.10b, more discernible in Fig. 2.10c and d in the downstream of the impingement areas. The impingement areas are strongly cooled down as shown by Sec. 4.4. The liquid accumulated here is being transported downstream by the momentum of each injection (and possibly partly by the gas flow), here the plate is not cooled as much as the impingement area leading to the evaporation of water. This phenomenon is more strongly pronounced after the three liquid footprints merge (Fig. 2.10c and d). Clearly discernible is the extension of the liquid film as well as the area of water evaporation on its margins.

Image processing delivered the liquid film area evolution over time before merging as shown in Fig. 2.11a. The maximum liquid film areas

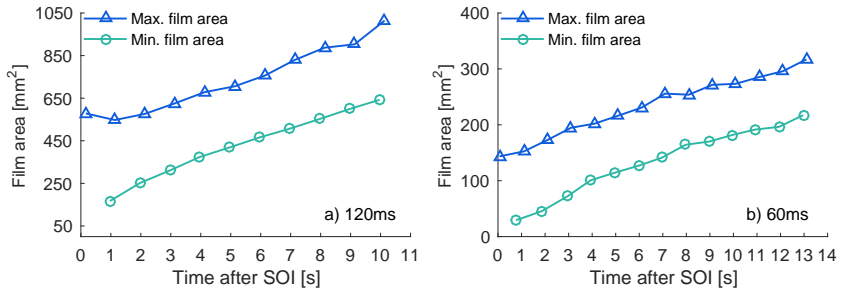


**Figure 2.11:** Initial liquid film area evolution before liquid film merging a) 300 °C, 100 kg/h, 120 ms of 1 Hz b) 300 °C, 100 kg/h, 60 ms of 1 Hz.

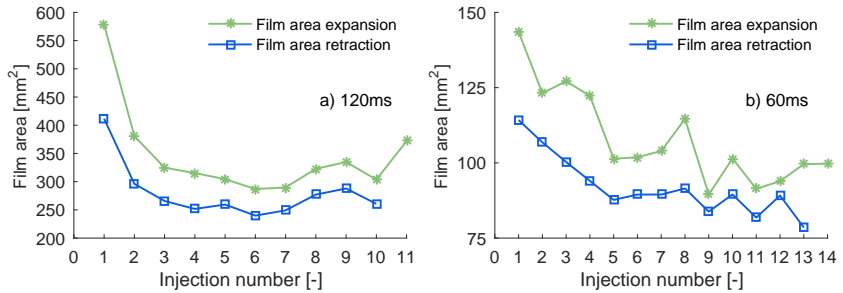


**Figure 2.12:** Liquid film area expansion and retraction a) 300 °C, 100 kg/h, 120 ms of 1 Hz b) 300 °C, 100 kg/h, 60 ms of 1 Hz.

are found right after each injection ending, while minimum film areas are found before the beginning of each injection. However, they both increase with time at a similar rate of  $50 \text{ mm}^2/\text{s}$ , as indicated by the slopes in Fig. 2.11a. A series of experiments with half of the injection duration (i.e. 60 ms) and identical gas flow conditions (Fig. 2.11b) resulted in a much slower liquid film area increase rate,  $15 \text{ mm}^2/\text{s}$  in average. By halving the injection duration, the impinging mass for each injection is lower; therefore, the liquid film area increases more slowly.

There are two effects to be considered as shown in Fig. 2.12: 1) the liquid film expansion during each injection, which is due to the new impinging liquid and 2) the liquid film retraction between two injections, which is due to the liquid evaporation. The liquid film expansion is derived by the difference between the maximum liquid film area of each injection and the minimum liquid film area of the previous injection. The

liquid film retraction is derived by the difference between the maximum and minimum liquid film areas of the same injection. The former could be used for estimating the average liquid film thickness (the impinging mass of each injection divided by the liquid film expansion area and the liquid density), while the latter could be used for estimating the heat extracted from the plate between two injections.

	Average thickness [ $\mu\text{m}$ ]	Heat [J]	Flux [ $\text{MW}/\text{m}^2$ ]
Present	611	155	1.79
IR [79]	370	94	1.09
Numerical [45]	200	51	0.59

**Table 2.4:** Estimated film thickness before liquid film merging and the comparison to numerical simulation [45].

Using Eq. 2.4 and Eq. 2.5, the entrainment and evaporation levels at the flow condition of  $300\text{ }^\circ\text{C}$ ,  $100\text{ kg/h}$  are  $12.4\%$  and  $28.7\%$ , respectively. Knowing the injection rate of  $7.2\text{ kg/h}$  (based on the manufacturer specification), the impinging mass per injection for the  $120\text{ ms}$  injection duration case is  $0.1414\text{ g}$  and  $0.0707\text{ g}$  for the  $60\text{ ms}$  case. Assuming all impinging liquid mass is deposited and local evaporation during injection is negligible, the average film thickness is estimated at  $388\text{ }\mu\text{m}$  for the  $120\text{ ms}$  injection duration case and  $611\text{ }\mu\text{m}$  for the  $60\text{ ms}$  injection duration case. These can be considered as the upper limits. Using the average film thickness and the average film retraction area between two injections (Fig. 2.12b), the evaporated mass per injection is deduced, and thus the heat extracted per injection from the plate is estimated at  $155\text{ J}$ . This leads to an average heat flux of  $1.79\text{ MW}/\text{m}^2$ . In Chap. 4 infrared thermography was used, and the heat extracted under similar conditions was estimated at  $94\text{ J}$ . Based on this heat extraction and the average film retraction area (Fig. 2.12b), the average film thickness is estimated at  $370\text{ }\mu\text{m}$ . Numerical simulations [27, 45] reported wall film thicknesses from  $70$  to  $200\text{ }\mu\text{m}$ , even though it should be taken into account that the injection and flow conditions are not directly comparable.

To our knowledge so far, no further studies reported liquid film thicknesses under comparable conditions.

At a later time, during the injection interval (between two injections), urea crystallizes intermittently at some locations as identified in Fig. 2.13. Water is primarily evaporated during the multi-stage evaporation process of UWS droplets [4, 5]. Therefore, the liquid film on the impinged plate is composed of a urea-enriched solution. When the plate temperature drops below the saturation point, urea crystallizes locally. The next injection with higher concentration of water subsequently dissolves the urea crystals as it arrives.

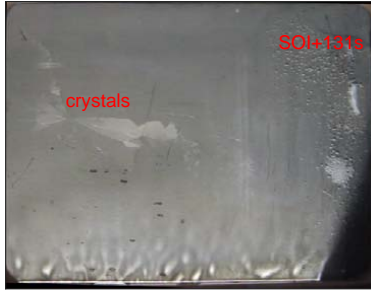


**Figure 2.13:** Solid urea crystallizes during the injection interval at a later stage (flow conditions: 300 °C, 100 kg/h, injection 1 Hz of 120 ms for 150 s).

After the end of the last injection, urea begins to crystallize from the urea-enriched liquid film in the periphery of the spray impinged area, reaching the maximum amount at EOI+9s (Fig. 2.14b). Thereafter, urea crystals start melting as a consequence of the temperature recovery of the plate and disappear completely at EOI+26s (Fig. 2.14c and d).

The crystal area evolution after EOI is quantified in Fig. 2.15. The image processing was performed according to the description in Sec. 2.2. The urea crystals spread most to 1117mm<sup>2</sup>. Furthermore, the urea crystallization speed is almost 2 times the urea melting speed. The crystallization temperature for 80 % urea-water solution is 80 °C. Therefore, the crystallization phase here is mainly driven by the process kinetics. However, the melting phase is strongly dependent on the heat transfer

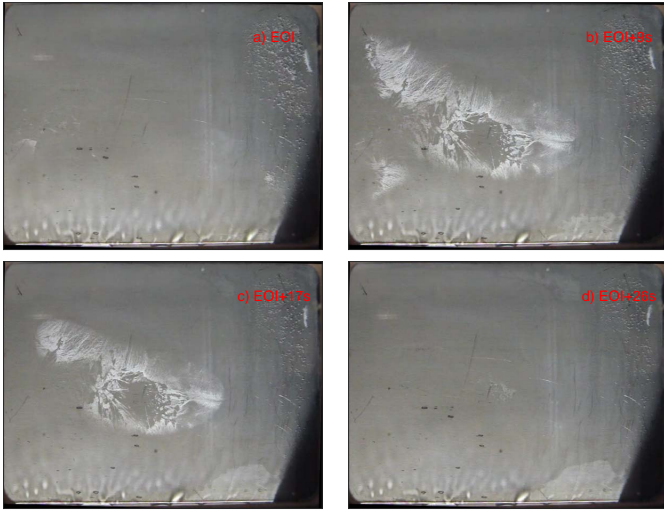


**Figure 2.14:** After the injector closes permanently, urea firstly crystallizes and then melts, followed by the liquid film evaporation (flow conditions: 300 °C, 100 kg/h, injection 1 Hz of 120 ms for 150 s).

rate. The fitted orange curve shown in Fig. 2.15 follows a 3<sup>rd</sup> order polynomial function, which takes the following form:

$$A = 0.00001354t^3 - 0.02249t^2 + 9.27t + 15.27 \quad (2.6)$$

where  $A$  is the crystal area, and  $t$  is the time after EOI.

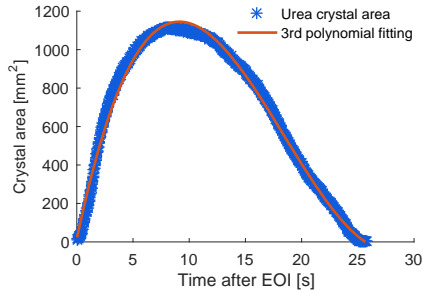


**Figure 2.15:** Urea crystallization and urea melting area evolution after the end of injection.

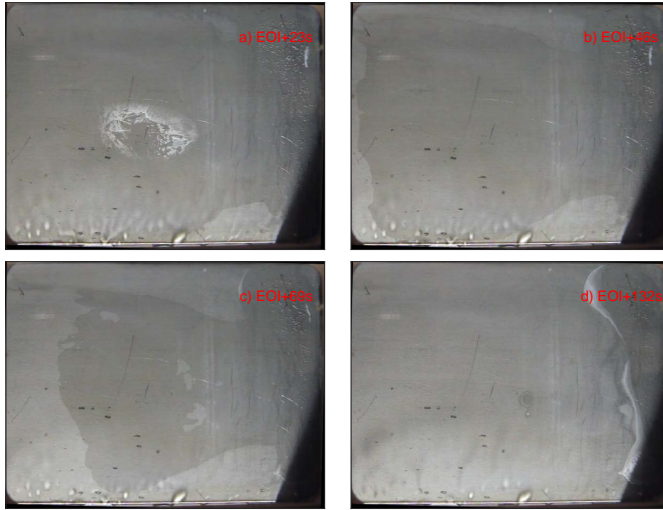


**Figure 2.16:** Urea enriched film starts evaporating from the upstream side, and white deposits form in the downstream side.

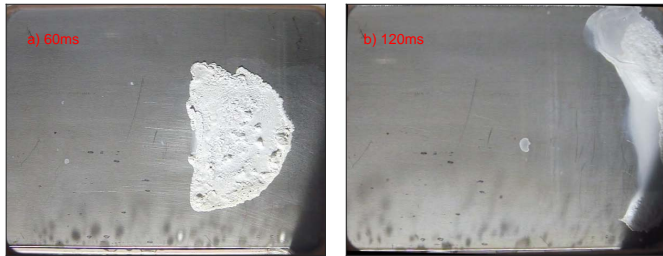


**Figure 2.17:** Deposit location and quantity for different injection durations at the flow condition of 300 °C 200 kg/h.

At EOI+23s, the urea-enriched film starts evaporating from the upstream side, from which the hot gas flow is coming. Fig. 2.16a shows the co-existence of urea crystal melting and liquid film evaporation. The evaporation front propagates from upstream to downstream and from the plate periphery to the plate center as displayed in Fig. 2.16a to c. At EOI+132s (Fig. 2.16d), the liquid film is completely evaporated in the impinging region, where no deposit is evidenced. However, white permanent deposits start forming in the merged film tip. This

deposit formation site is more downstream than the impingement region. Fig. 2.17b displays the final state of the permanent deposits on the plate after the liquid is completely evaporated. If the injection duration is shortened, the deposit formation site is located more upstream as shown in Fig. 2.17a. Decreased injection momentum drives the liquid accumulation region less downstream.

### 2.3.3 Solid deposit composition analysis

Solid deposits removed from the plate (Fig. 2.17b) have been analyzed by NMR spectroscopy. The main resonance with around 75% of the total signal intensity is observed at 167.2 ppm and four resonances of minor compounds are detected at 169.1, 168, 166.5 and 164.7 ppm as shown in Fig. 2.18a. In a series of further experiments, small aliquots of reference materials urea, biuret, triuret, cyanuric acid (CYA), ammeline, ammeline or melamine were added to the sample solution. From the increases of individual resonances after spiking with individual resonance compounds, the compounds ammeline, ammeline and biuret were unambiguously identified (Fig. 2.18b-d). The main resonance at 167.2 ppm in the  $^{13}\text{C}$  NMR spectrum is assigned to cyanuric acid (spectrum not shown). Please note that the recording of  $^{13}\text{C}$  NMR data of the pristine reference material throughout resulted in considerably different chemical shifts not directly comparable to the signals observable in the spectrum of the sample.

In Fig. 2.19 the  $^{13}\text{C}$  NMR spectra of the sample 'as is' and after spiking with the reference materials urea, triuret and ammeline are shown. It is clear from these spectra, that none of the three compounds is present in the mixture at significant amounts since none of the additional signals match to the resonances of the sample solution (Fig. 2.19a). The decomposition of cyanuric acid initiates at 320 °C and is limited by the reaction kinetics [10]. Therefore, cyanuric acid and the other chemical species remain in the form of permanent deposits for the 300 °C case. From line shape analysis (see experimental part) and under consideration of the formulae shown in Eq. 2.3, the composition [wt-wt-%] of the



sample was determined as 73.0% cyanuric acid, 13.8% biuret, 11.8% ammeline and 1.5% ammeline. In Tab. 2.5 the sample compositions of all data shown in Fig. 2.18 and Fig. 2.19 are summarized. It is clearly observable that, as expected, the spiking with reference material is reflected in an increase of the amount of the respective material. It must be mentioned that depending on pH and sample concentrations we observed a considerable variation of the  $^{13}\text{C}$  chemical shifts in NaOD/D $_2\text{O}$  solutions. It seems that for each sample of interest with an essentially different composition, the above mentioned laborious signal assignment procedure must be carried out.

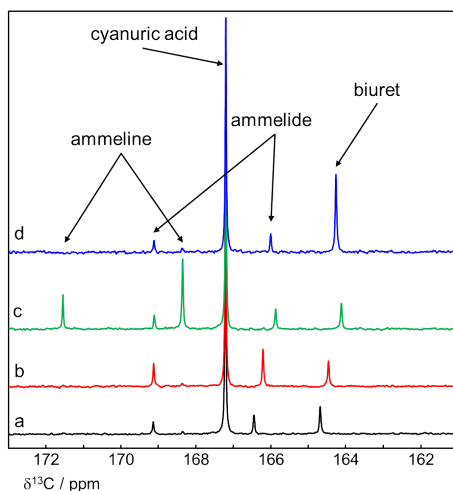


**Figure 2.18:**  $^{13}\text{C}$  NMR spectra of a stock solution (1.3 wt/wt-%) of solid deposits in 1.5 M NaOD/D $_2\text{O}$  of a) 'as is' and after addition of small quantities of b) ammeline, c) ammeline and d) biuret.

Our preliminary investigations using DMSO- $d_6$  as solvent at the beginning resulted in very promising results since the chemical  $^{13}\text{C}$  shifts did not largely vary for different sample concentrations nor for spectra recorded using the pristine reference compounds. In contrast to the NaOD/D $_2\text{O}$  solutions discussed above, in DMSO also valuable information seemed to result from  $^1\text{H}$  NMR where each reference material showed individual and partially well separated resonances. The big

compound	ammelide	ammeline	CYA	biuret	urea	triuret
sample	11.8 %	1.5 %	73.0 %	13.8 %		
& urea	7.6 %	1.2 %	48.9 %	7.9 %	34.3 %	
& biuret	8.7 %	2.0 %	58.1 %	31.2 %		
& triuret	8.3 %	1.1 %	50.1 %	10.0 %		30.4 %
& ammeline	9.4 %	26.1 %	54.6 %	9.9 %		
& ammelide	21.0 %	1.8 %	65.5 %	11.8 %		
& CYA	3.7 %	0.6 %	90.8 %	4.9 %		

**Table 2.5:** Sample compositions determined by quantitative evaluation of  $^{13}\text{C}$  NMR data of sample under the condition of 300 °C, 100 kg/h 120 ms 'as is' and after addition of small aliquots of reference material.

drawback of DMSO as solvent was the low solubility of e.g. ammelide and ammeline and clean solutions were only obtained upon heating up to 180 °C or even higher. We noticed that under these conditions the cyclic poly-urea chemical species partly decomposed to lower molecular weight compounds (urea, biuret). Moreover, depending on the sample treatment, we observed rather different sample compositions although the same starting material was examined.

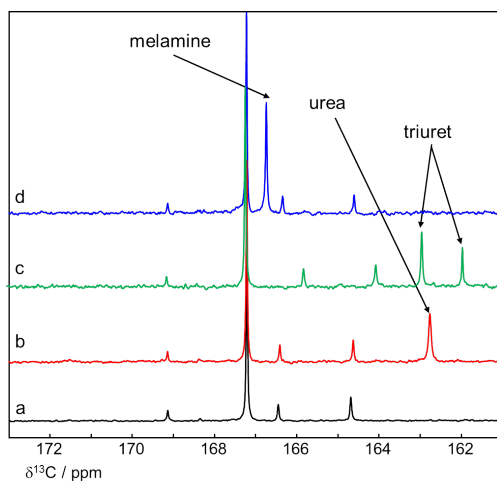


**Figure 2.19:**  $^{13}\text{C}$  NMR spectra of a stock solution (1.3 wt/wt-%) of solid deposits in 1.5 M NaOD/D<sub>2</sub>O of a) 'as is' and after addition of small quantities of b) urea, c) triuret and d) melamine.

## 2.4 Summary

A detailed experimental investigation of the UWS spray impingement under diesel exhaust-typical flow conditions has been performed. First, the spray impinging mass and its dependency on the gas flow momentum and temperature have been quantified by a mechanical patternator. Additionally, the impinging droplet size distribution has been characterized by PDA. Furthermore, phenomena associated to the UWS spray impingement process, such as liquid film evolution, nucleate boiling and solid deposit formation, have been analyzed through optical high speed imaging experiments. Finally, the solid deposit composition has been identified by NMR spectroscopic analysis. The main conclusions and achievements of this work are:

1. There are three distinct impingement regions, each corresponding to one hole of the used injector. The maximum local impingement flux is  $0.0212 \text{ kg}/(\text{mm}^2\text{h})$  at stagnant condition, while it drops down to  $0.0119 \text{ kg}/(\text{mm}^2\text{h})$  at the flow condition of  $300^\circ\text{C}$ ,  $200 \text{ kg/h}$ .
2.  $35.6\%$  of the injected fluid impinges on the opposed wall at the exhaust flow conditions of  $300^\circ\text{C}$ ,  $200 \text{ kg/h}$  due to the entrainment and the evaporation in the gas flow. The relationship between the entrainment level and the gas flow momentum fits well with a logarithmic function, while the gas flow temperature influence on evaporation is more complex.
3. The impingement mass percentage is gradually increasing with increasing droplet diameter up to  $90 \mu\text{m}$ , whereas almost all larger droplets reach the opposed wall. For droplets below  $20 \mu\text{m}$ , the hot flow entrains or evaporates almost everything, whereas  $40\%$  of mass reduction is evidenced from droplets between  $73 \mu\text{m}$  and  $90 \mu\text{m}$ .
4. The spray impingement leads to liquid film formation due to strong local cooling. Over time, liquid film footprints spread out and

merge. Thereafter, significant amount of the liquid is transported downstream mainly by the momentum of each injection and forms a liquid accumulation site.

5. After the injection termination, urea starts to crystallize from the urea-enriched liquid film around the spray impinged area, and then melts. The urea crystallization rate is almost 2 times the urea melting rate. The crystallization rate is mainly driven by the process kinetics. However, the melting rate is strongly dependent on the heat transfer rate.
6. Following melting, the urea-enriched film starts evaporating from the upstream side. The thin film in the impinged region is completely evaporated, and no deposit remains.
7. However, solid deposits form at the liquid accumulation site. Increasing the injection momentum drives the liquid accumulation further downstream, thus the deposit formation site.
8. From NMR spectroscopy, it has been determined that the solid deposit is composed of 73.0% cyanuric acid, 13.8% biuret, 11.8% ammeline and 1.5% ammeline.

The observed phenomena and proposed correlations can be used for the design and lay-out of the injection and mixing sections of the SCR systems. Although it is not entirely clear how solid deposits could be completely avoided, our study shows ways to mitigate the deposits. In addition, it is shown that high temperatures help, and above a certain threshold they even contribute to the sublimation of solid deposits.

# 3 Fluid dynamic characteristics of the impinging spray

Parts of this chapter are published in: Y. Liao, P. Dimopoulos Eggenchwiler, A. Spiteri, L. Nocivelli, G. Montenegro, and K. Boulouchos, "Fluid Dynamic Comparison of AdBlue Injectors for SCR Applications," *SAE International Journal of Engines*, vol. 8, no. 5, pp. 2303-2311, 2015.

## Abstract

The injection process of urea-water solution (AdBlue) determines initial conditions for reactions and catalysis and is fundamentally responsible for optimal operation of selective catalytic reduction (SCR) systems. The spray characteristics of four commercially available injectors (one air-assisted and three pressure-driven with different nozzle-hole configurations) are investigated with non-intrusive measuring techniques. Injection occurred in the crossflow of a channel with preheated air in an exhaust duct similar configuration. The effect of several gas temperatures and flows on the spray propagation and entrainment has been extensively studied by shadow imaging. Shadow images have shown that the spray of the pressure-driven injectors is only marginally affected by the gas crossflow. In contrast, the air assisted spray is strongly deflected by the gas, the effect increasing with increasing gas flow. Phase Doppler Anemometry (PDA) measurements have delivered droplet size distributions and droplet velocities. Measurements have been performed in several locations near the opposed channel wall area. Sauter mean diameters of the droplets from the pressure-driven injectors are between 60-80  $\mu\text{m}$  while that of the air assisted is 20  $\mu\text{m}$ . Higher velocities have

been associated with the larger droplets in the pressure-driven spray after the primary breakup while droplet velocities have been evenly distributed to all droplets sizes in the air-assisted spray.

### **3.1 Introduction**

Fluid dynamic investigations of urea-water SCR sprays have been conducted in our laboratory in the last years based on a specifically designed test rig having exhaust similar conditions while providing the possibility to set exact mass, temperature and composition of the gas flow. The fluid dynamic behavior of a 6-hole SCR injector spray was extensively investigated [44], characterizing the macro spray properties. The spray morphology and droplet size distributions under exhaust flow conditions have been used to validate numerical simulations [35, 45]. The influence of two different injectors on the NO<sub>x</sub> conversion of an SCR catalyst was investigated in [7].

The present work compares four commercially available injectors experimentally in terms of the bulk spray analysis, droplet size and droplet velocity distributions and predicts the suitability for mobile SCR applications. In addition, the results provide valuable initial boundary conditions for numerical modelling of the SCR system or alternatively enable the validation of SCR spray models.

### **3.2 Experimental setup and methods**

The experiments were conducted in the flow laboratory at EMPA, Dübendorf. This laboratory was designed for the experimental investigation of urea-water injection into the exhaust channel for SCR application. All experiments were done with dry air as exhaust flow to investigate the fluid dynamic behavior of the injection spray. The air is taken from the EMPA pressurized air network and fed into a large dampening volume to get rid of possible oscillations. The air flow is then led through three heating units to reach the target temperature. The prepared gas flow subsequently passes through the injection channel assembly which allows

Injector	A-A	P1-6H	P-3H	P2-6H
Driven mechanism	air-assisted	pressure	pressure	pressure
Pressure	-	9 bar	9 bar	9 bar
Air-pressure	1.5 bar	-	-	-
Static flow rate	2.64 kg/h	15.2 kg/h	7.2 kg/h	7.3 kg/h
Nozzle diameter	970 $\mu\text{m}$	210 $\mu\text{m}$	190 $\mu\text{m}$	130 $\mu\text{m}$
Nozzle number	1	6	3	6
Spacing diameter	-	1.3 mm	1.9 mm	1.9 mm

**Table 3.1:** Characteristics of the four commercial SCR injectors

optical access from four directions, two from the sides, one from the top and one from the bottom. In this work, the chamber with a square cross section of 80 mm by 80 mm and 150 mm in length is used. The gas flow through the measurement chamber can be regulated up to 450 kg/h and 500 °C, which allows the reproduction of engine exhaust-like conditions.

Tab. 3.1 shows the injector characteristics including: driven mechanism, working pressure, static flow rate and nozzle geometries. The injector was mounted on the top of the measurement chamber, 50° inclined to the gas flow direction. The high pressure system of the urea dosing unit can deliver fluid pressures of up to 15 bar. The pressure-driven injectors were operated with a back pressure of 9 bar during experiments and the air-assisted injector worked with an air pressure of 1.5 bar. Fig. 3.1 shows the stereo-microscopic photographs of the nozzle tip configuration of the four commercial SCR injectors investigated. A-A is a single-hole air-assisted injector. The intermediate ring between the injection nozzle and the air nozzle is 310  $\mu\text{m}$  thick and the width of the air nozzle is 165  $\mu\text{m}$ .

In this study, shadow imaging and phase Doppler anemometry (PDA) have been applied to investigate the behavior of the spray. For shadow imaging, the optical system was set up according to Fig. 3.2. The laser positioned at the back of the injection chamber was expanded over a hemispherical lens to illuminate the diffusion plate, for creating a uniform bright background. The camera was located on the other side of the injection chamber to capture images of the spray in front of the il-

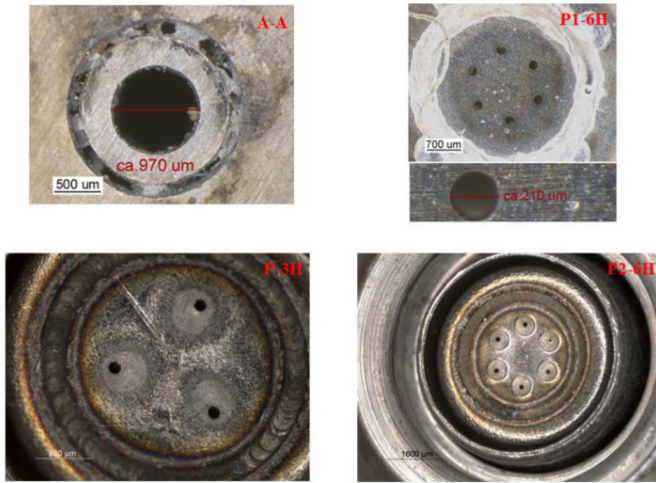


**Figure 3.1:** Stereo-microscopic photographs of the nozzle tip configuration of the four commercial SCR injectors investigated.

luminated background. On the images captured by the camera there are shadows where the laser light has been scattered away by the spray droplets, being visible over a bright background as shown in Fig. 3.2. The background illumination was done by using Cavitar CAVILUX Smart. It is a pulsed diode laser light source with a wavelength of 690 nm. Laser pulses of 40 ns and 1 Hz synchronized with the injection event were used to avoid significant movement during the laser pulse and overexposure of the camera sensor. The PCO Sencicam camera with a resolution of 1040 by 1376 pixels was used as the recording source.

Phase doppler anemometry (PDA) has been applied to measure the droplet sizes and velocities prior to the impingement on the wall. The setup is shown in Fig. 3.3 and the settings are shown in Tab. 3.2. The system uses two high power diode lasers at the wavelength of 488 nm and 514 nm. The receiver detects the first order refracted light at the Brewster angle of  $70^\circ$  with parallel polarization in the horizontal plane. The 2D PDA system measures velocities in the vertical direction and in the horizontal direction. PDA measurements were conducted on the plane 60 mm below the injector exit vertically for the injectors A-A and



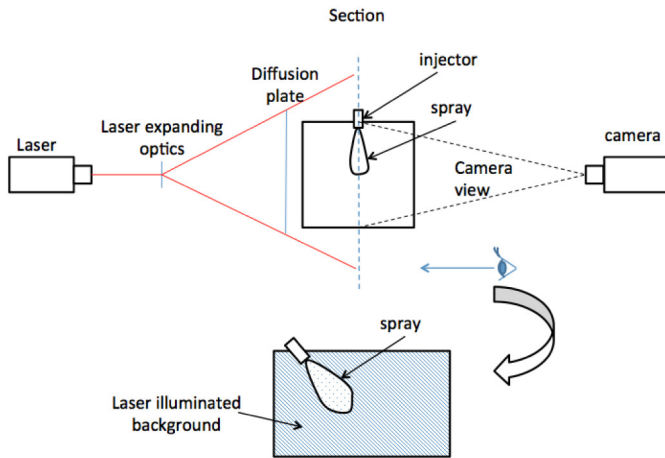


**Figure 3.2:** Schematic diagram of shadow imaging setup.

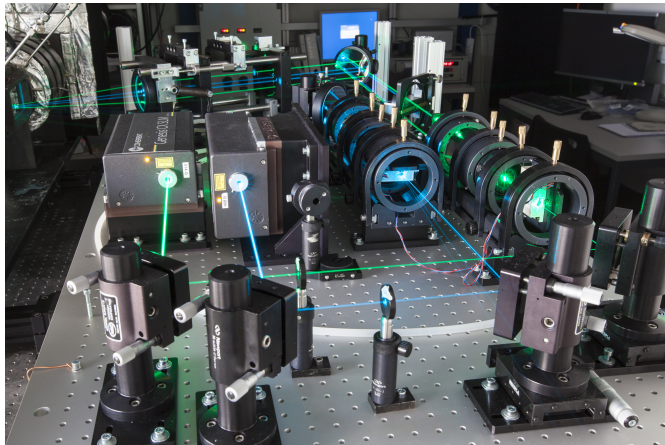


**Figure 3.3:** Setup to characterize the plate emissivity with lid removed.

Sending optics		
Wavelength	514 nm	488 nm
Separation distance	45 mm	45 mm
Lens focal length	350 mm	350 mm
Intersection angle	7.36°	7.36°
Measurement volume	80 $\mu\text{m}$ $\times$ 80 $\mu\text{m}$ $\times$ 1190 $\mu\text{m}$	80 $\mu\text{m}$ $\times$ 80 $\mu\text{m}$ $\times$ 1190 $\mu\text{m}$
Fringe spacing	4 $\mu\text{m}$	3.8 $\mu\text{m}$
Receiving optics		
Receiving optics	DANTEC 57 $\times$ 10 2-D	
Scattering angle	70°	
Polarization angle	0°	
Lens focal length	310 mm	
Angle adjustment slit	0.25 mm	
Processor	DANTEC 58N10	
Processor bandwidth	45 MHz	

**Table 3.2:** PDA sending optics and receiving optics settings

Temperatures [ $^{\circ}\text{C}$ ]	Flow rate [kg/h]	Mean velocity [m/s]	Re [-]
200	100	5.8	15116
200	200	11.6	30332
200	300	17.5	45498
300	100	7	13292
300	200	14.1	26585
300	300	21.1	39877

**Table 3.3:** Experimental flow conditions

P1-6H, and 80 mm for the injectors P-3H and P2-6H at different transverse locations. The PDA result part involves a droplet size comparison of four commercial injectors, two of which are from a previous dissertation conducted in the same laboratory [48]. Previous study [44] in the same laboratory proves that the injected fluid water and Adblue show similar behaviors in terms of the bulk spray properties and the droplet size distributions. Thus, water sprays were used in this work. For both shadow imaging and PDA measurements, relevant flow conditions were chosen. They are similar to exhaust gas conditions at the catalyst inlet. Tab. 3.3 shows the channel flow conditions at which different optical techniques were applied.

## 3.3 Results and Discussion

This section is organized in the following way: firstly, shadow imaging shows the overall shape of sprays from different SCR injectors and also the influence of the exhaust flow conditions on the overall spray outline. Comparative analysis of droplet size distributions from PDA measurements on the near-wall plane provides a good indication of the atomization efficiency of the different injectors studied and gives the initial conditions of the spray/wall interaction together with the droplet velocities. Finally, the study is completed by the determination of droplet volume flow rates at different locations for different droplet sizes.

### 3.3.1 Spray contours analysis

Shadow imaging is applied to visualize the overall shape of the sprays from the four injectors. Fig. 3.4 shows the spray contours at the same exhaust flow temperature of 300 °C but at different exhaust mass flow rates 100 kg/h, 200 kg/h and 300 kg/h. The images are obtained through binarizing the averaged image of 120 raw images which were taken at 16 ms after the electronic start of injection. According to a previous study conducted in the same laboratory [44], the pressure-driven injector sprays reach the maximum penetration in the flow channel at 10 ms after the electronic start of injection.

Fundamentally different to the other three injectors, the air-assisted injector spray features increasing deflection of propagation with increasing exhaust mass flow rate. With increasing exhaust flow velocity the spray tends to propagate along the axial flow direction. As the spray moves coaxially with the exhaust flow, the droplets mix better with the exhaust flow and wall impingement is minimized. This behavior is favorable for the SCR application.

The spray from the 3-hole pressure-driven injector has three distinct spray cones, whereas sprays from the other two pressure-driven injectors merge into a single spray cone. This is due to the relatively large circumferential separation of the nozzle holes (120°) and the larger ratio of the nozzle diameter to the spacing radius, as seen in Tab. 3.1 and Fig. 3.1.

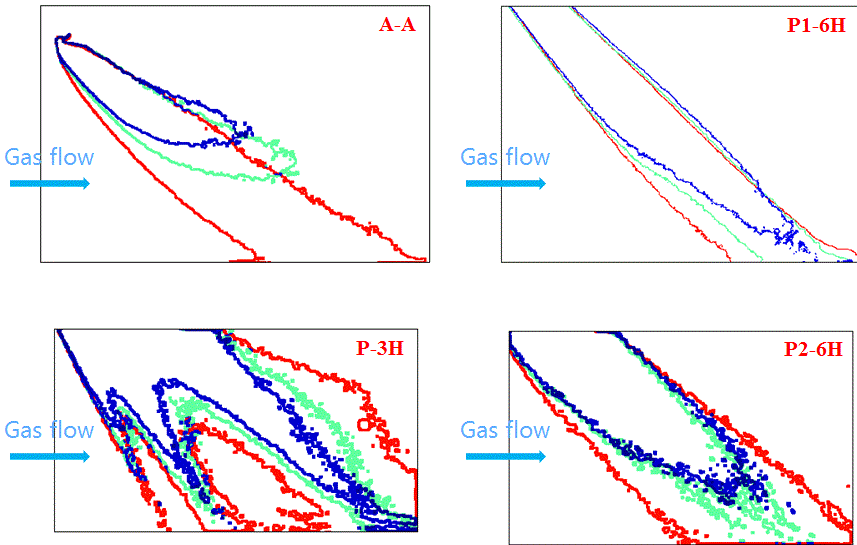


**Figure 3.4:** Shadow imaging contours at different flow conditions for the four commercial SCR injectors (gas flow conditions: 300 °C, red: 100 kg/h, green: 200 kg/h, blue: 300 kg/h)

This phenomenon prevents the formation of a large unified liquid pool on the opposed channel wall. Nevertheless, the liquid pool forming on the opposed wall is substantial. This can be detrimental for the SCR systems operation.

Comparing the different color contours in Fig. 3.4, the spray contour shrinks with the increasing exhaust gas flow velocity. The shrinking evidences increasing small droplet entrainment with increasing gas flow. As can be expected, the spray wall impingement also decreases with the increasing gas flow velocity. The images of the sprays of the two 6-hole injectors show also that the exhaust gas flow affects only the upstream contour of the spray and does not affect the downstream contour. Based on extensive investigations, we can conclude that the sprays from pressure-driven injectors are hitting the opposed wall always at the same location, regardless of the flow properties.

### 3.3.2 Droplet sizes and velocities

#### Droplet size distributions

PDA measurements were conducted on the plane  $y=60$  mm for the injectors A-A and P1-6H,  $y=80$  mm for the injectors P-3H and P2-6H at different transverse locations. In this section, the droplet size distributions, droplet velocities and droplet volume flow rates will be shown and discussed.

The figures shown in this section contain the droplet size distributions and droplet volume distributions. The size and volume distributions are significant for the mass and heat transfer issues of the spray in the exhaust gas flow. The droplet volume distributions determine the droplet mass distributions and have great influence on the effectiveness of the selective catalytic reduction reactions in a catalyst downstream. Fig. 3.5 to Fig. 3.8 show such distributions for the four different injectors at exhaust gas flow condition of  $300\text{ }^{\circ}\text{C}$ ,  $100\text{ kg/h}$ .

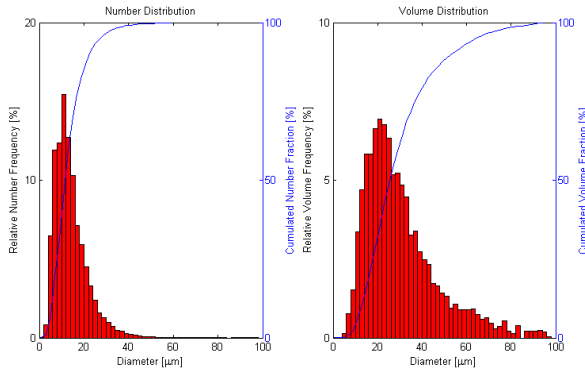


**Figure 3.5:** Droplet size distribution and droplet volume distribution of the injector A-A (air-assisted) exhaust gas flow conditions:  $300\text{ }^{\circ}\text{C}$ ,  $100\text{ kg/h}$

The air-assisted injector produces much smaller droplets than the pressure-driven injectors. The 6-hole P2-6H features a narrow distribution centered around  $47\text{ }\mu\text{m}$ . Compared to the 3-hole injector P-3H, P2-6H produces much smaller droplets due to the reduced nozzle diameter, in spite of the same operating pressure and static flow rate.

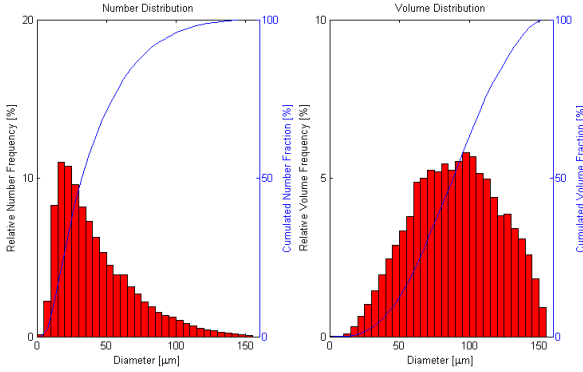


**Figure 3.6:** Droplet size distribution and droplet volume distribution of the injector P1-6H (6-hole pressure-driven) exhaust gas flow conditions: 300 °C, 100 kg/h.

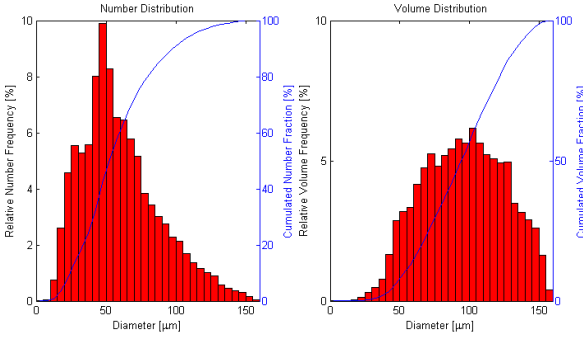


**Figure 3.7:** Droplet size distribution and droplet volume distribution of the injector P-3H (3-hole pressure-driven) exhaust gas flow conditions: 300 °C, 100 kg/h.

Droplet sizes of air-assisted injection are considerably lower than those of the other three injectors. From the droplet size distribution on the left, it is seen that 80% percent of droplets are smaller than 18  $\mu\text{m}$  and there is no droplet which is larger than 100  $\mu\text{m}$ . However, the last one percent of droplets which are bigger than 39  $\mu\text{m}$  contribute to 22% percent of the total mass. Nevertheless, the air-assisted injector has been seen as a better atomization source for this purpose, compared to the conventional pressure-driven injectors.

	A-A	P1-6H	P-3H	P2-6H
Maximum droplet size [ $\mu\text{m}$ ]	97	153	162.5	138
80% of droplets $\leq$ [ $\mu\text{m}$ ]	18	61	80	63.5
80% of mass in droplets $\leq$ [ $\mu\text{m}$ ]	41	117	121.5	91.5
$D_{32}$ [ $\mu\text{m}$ ]	20.4	68.7	81.4	64.5
80% of mass in droplets [ $\mu\text{m}$ ]	[13,55]	[46,130]	[13,134]	[41,103]

**Table 3.4:** Summary of droplet size distributions

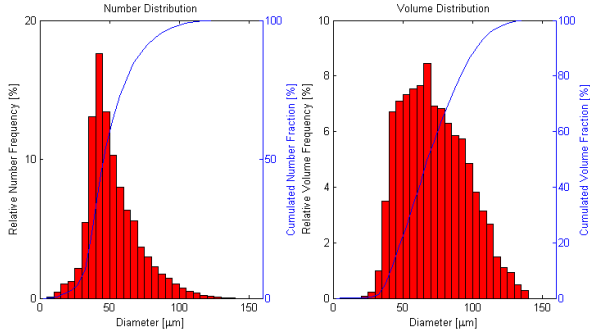


**Figure 3.8:** Droplet size distribution and droplet volume distribution of the injector P2-6H (6-hole pressure-driven) 300 °C, 100 kg/h.

The most important results from the distributions shown in Fig. 3.5 to Fig. 3.8 are summarized in Tab. 3.4.

### Droplet velocity distributions

Fig. 3.9 to Fig. 3.12 show the mean downward and flow-directional velocity components together with the error bar at different transverse locations for the four injectors at exhaust flow of 300 °C, 300 kg/h. At this flow condition, the mean gas flow velocity is 21.1 m/s and the maximum gas flow velocity 26 m/s. The injector axis ( $x=50$  mm) can be clearly seen in the velocity profiles of the air-assisted injector, around which there are higher velocity magnitudes in particular of the vertical velocity component. This velocity component decreases towards 0 with increasing distance from the injector axis in the downstream locations. The axial velocities are between 20 and 26 m/s, close to the mean exhaust gas velocity. Larger droplets have slightly lower velocities which are stabilizing in the downstream locations. This is clear indication that

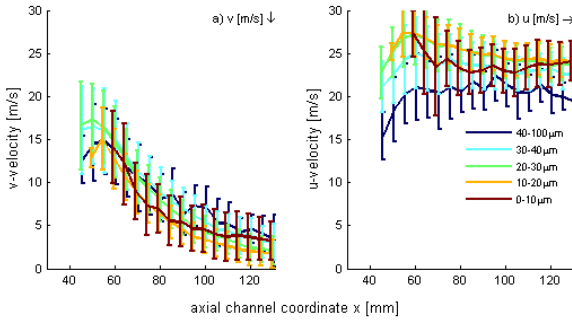


**Figure 3.9:** a) Mean downward velocities and b) mean axial velocities for the case of 300 °C, 300 kg/h at different axial locations for A-A (air-assisted) for different droplet size classes

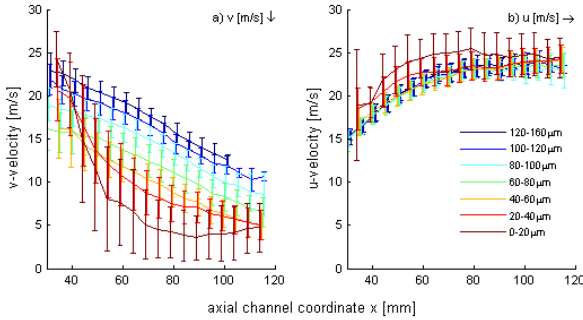


**Figure 3.10:** a) Mean downward velocities and b) mean axial velocities for the case of 300 °C, 300 kg/h at different axial locations for P1-6H (6-hole pressure-driven) for different droplet size classes.

larger droplets are accelerated by the exhaust flow towards the mean flow velocity. Smaller droplets have rather higher axial velocities and are slowed down by the flow towards the gas flow velocity.

The velocity components of all the three pressure-driven injectors show different behaviors. The axial velocity component has very similar characteristics among all three pressure driven injectors (Fig. 3.10 to Fig. 3.12). Droplets are accelerated towards the mean exhaust gas velocity in the downstream region and the variance of their velocities is very limited.



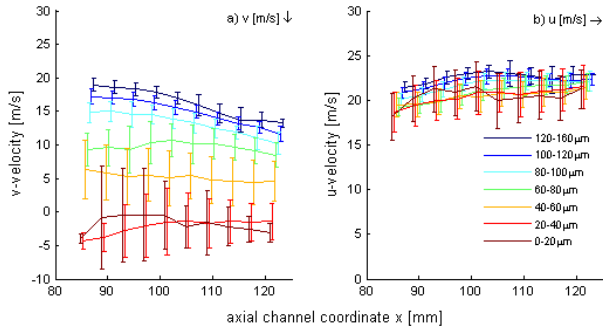


**Figure 3.11:** a) Mean downward velocities and b) mean axial velocities for the case of 300 °C, 300 kg/h at different axial locations for P-3H (3-hole pressure-driven) for different droplet size classes.

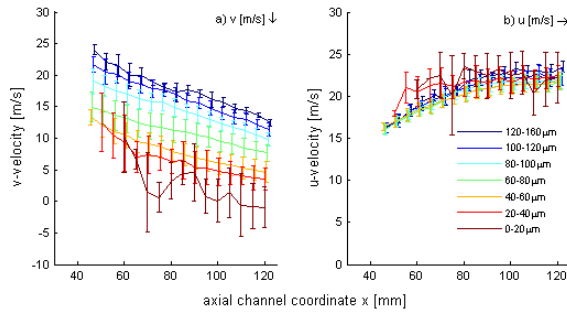


**Figure 3.12:** a) Mean downward velocities and b) mean axial velocities for the case of 300 °C, 300 kg/h at different axial locations for P2-6H (6-hole pressure-driven) for different droplet size classes.

The characteristics of the vertical velocity component distribution differ significantly among the three pressure-driven injectors as well as in respect to the air-assisted one. All droplets from the P1-6H injector have similar vertical velocities in the vicinity of the injector axis. Further downstream the bigger droplets have also larger vertical velocity components. Smaller droplets are stronger decelerated. This is due to the aerodynamic drag acting on the droplet, which is inversely proportional to the square of the droplet diameter and proportional to the relative velocity. Vertical velocities of droplets from the 3-hole pressure-driven injector

(Fig. 3.11) are less affected by the flow environment: larger droplets have maintained a large portion of their initial vertical velocities (vertical velocities drop from 20 m/s to 14 m/s). Smaller droplets on the other hand have even negative vertical velocity components. This is clear indication of droplet rebound on the opposed wall. Droplets from the second tested pressure-driven 6-hole injector, (P2-6H), as seen in Fig. 3.12, have been stronger decelerated in their vertical movement. Bigger droplet velocities are below 13 m/s in the downstream locations. Negative downward velocities of smallest droplet size class may imply the splashing effect.

### 3.3.3 Droplet volume flow rates

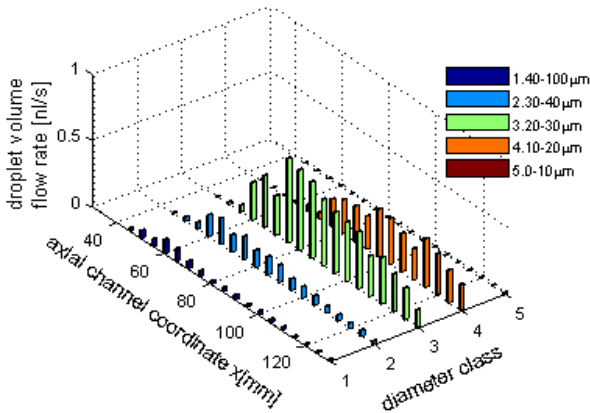


**Figure 3.13:** Droplet volume flow rate for the case of 300 °C, 300 kg/h at different axial locations for the A-A (air-assisted) injector.

The main volume flow of the spray from the air-assisted injector is characterized by droplets between 20 and 40  $\mu\text{m}$  in the vicinity of the injector axis ( $x=50$  mm). Further downstream the spray volume flow is included in diminishing droplet sizes. While at around 80 mm downstream the injector exit the spray volume is mainly contained in droplets with diameters in the 20-30  $\mu\text{m}$  class, further downstream the prevailing diameter class is 10-20  $\mu\text{m}$  (Fig. 3.13).

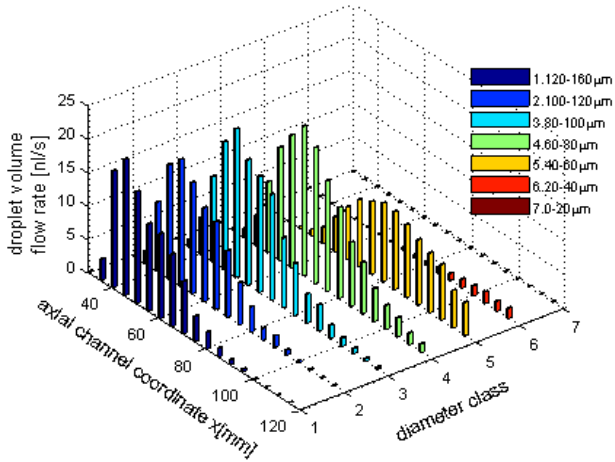


**Figure 3.14:** Droplet volume flow rate for the case of 300 °C, 300 kg/h at different transverse locations for P1-6H (6-hole pressure-driven) injector.

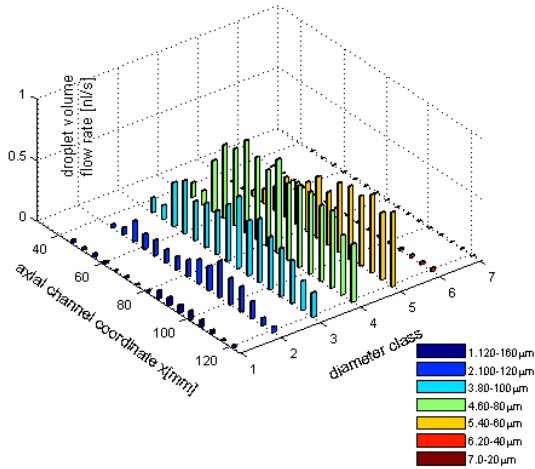


**Figure 3.15:** Droplet volume flow rate for the case of 300 °C, 300 kg/h at different axial locations for P2-6H (6-hole pressure-driven) injector.

The main volume part of the spray is distributed in completely different diameter classes if taking into account the 6-hole injector P1-6H, Fig. 3.14. In the vicinity of the spray axis ( $x=50$  mm) the spray volume is more or less equally distributed in droplets from 80-160  $\mu\text{m}$ . Further

downstream (at  $x=100$  mm) the spray volume is distributed in droplets from 20-60  $\mu\text{m}$ .

The differences between the two 6-hole injectors, already discussed in combination with Fig. 3.6 and Fig. 3.8 are also reflected in the spray volume flow rates when comparing Fig. 3.14 and Fig. 3.15. The spray of injector P2-6H contains the largest part of the volume flow in smaller droplets in the vicinity of the injector axis (60-100  $\mu\text{m}$ ). In respect to the more downstream positions, the majority of the volume flow is contained in droplets with diameters in the 40-60  $\mu\text{m}$  range.

As already described in the former section, the spray of the 3-hole injector is consisting of 3 distinct spray cones. Thus the crucial reference point for the characterization is the intersection of one spray cone's axis with the measurement plane at  $x=95$  mm. On the axis of this cone the largest part of the spray volume is transported with droplets from 100-160  $\mu\text{m}$ . Further downstream the droplets carrying significant part of the spray volume are smaller but still larger than 40  $\mu\text{m}$ .

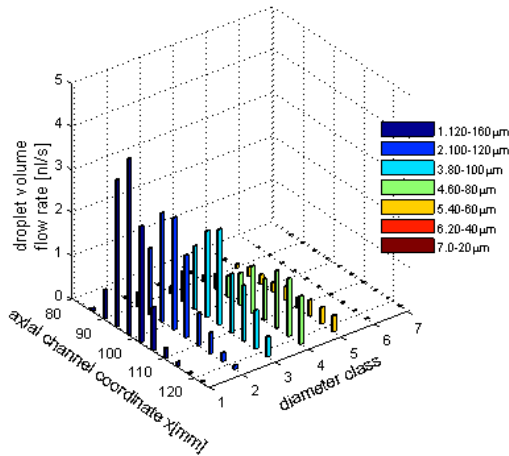


**Figure 3.16:** Droplet volume flow rate for the case of 300 °C, 300 kg/h at different axial locations for P-3H (3-hole pressure-driven) injector.

## 3.4 Summary

SCR spray characteristics differ drastically among available injectors.

1. The air-assisted injector generates a spray which is highly susceptible to the exhaust gas flow. Increasing exhaust gas flow strongly deflects the spray and increases entrainment drastically. The result is significantly decreased wetting of the opposed wall.
2. The 3-hole pressure-driven injector generates 3 distinctive spray cones. These cones are only weakly affected by the exhaust flow, propagating in the same direction regardless of the exhaust flow intensity. However, entrainment modestly increases with increasing flow rate.
3. The two 6-hole pressure-driven injectors generate one single spray cone as the six cones merge soon after the nozzles. Only the upstream contour of the spray is affected by the exhaust flow. Entrainment increases with increasing exhaust gas flow in a moderate manner.
4. All sprays of the pressure-driven injectors hit the opposed wall at the same location, regardless the exhaust flow conditions.

The droplet size distributions of each injector revealed:

1. The air-assisted injector results in smallest droplet sizes.
2. The 3-hole pressure-driven injector is characterized by the largest droplet sizes.
3. Injectors P1-6H and P2-6H, the pressure-driven 6-hole injectors, have similar average droplet sizes. However, the distribution of the latter is narrower than of the former. The largest part of the spray mass of the latter is contained in droplets almost 30% smaller than those of the former.

Mean velocities of droplets in the sprays generated by the injectors tested had significantly different characteristics:

1. Axial velocities of the droplets generated by pressure-driven injectors in the injector axis were lower than the mean gas velocities. Droplets regardless of size have been accelerated in the downstream towards the mean flow velocities.
2. The vertical velocity components of the droplets generated by the pressure-driven injectors had a clear distribution over the droplet sizes:
  - a) Larger droplets are only modestly decelerated by the gases and keep the larger part of their velocity also in the locations far downstream the injector axis.
  - b) Smaller droplets are stronger carried by the axial flow and strongly decelerated by the aerodynamic drag in their vertical movement.
  - c) The droplets from the 3-hole pressure-driven injector reach the opposed wall and splash.
3. Velocities of the droplets from the air-assisted injector behaved similar to the smallest droplets of the pressure-driven injectors. In addition, taking into account entire spray propagation characteristics it can be expected that only a very limited fraction of these droplets will reach the opposed wall with very low velocities. Thus, very limited, if any, rebound is expected.

In general, the main part of the spray volume flow is contained in larger droplets in the vicinity of the spray or the spray cone axis. Further downstream, the droplet sizes containing the main part of the spray volume are significantly smaller. The air-assisted injector spray is associated with smaller droplets in all investigated locations. Among the pressure-driven injectors significant differences exist in respect to the spray volume distribution over different droplet sizes. The injector location and the vicinity to further parts like the exhaust pipe walls and the catalysts are decisive for the selection of the most suitable injector.

# 4 Heat transfer characteristics of a single spray impingement event

Parts of this chapter are published in: Y. Liao, R. Furrer, P. Dimopoulos Eggenschwiler, and K. Boulouchos, "Experimental investigation of the heat transfer characteristics of spray/wall interaction in diesel selective catalytic reduction systems," *Fuel*, vol. 190, pp. 163-173, 2017.

## Abstract

This study presents an experimental investigation of the heat transfer characteristics of the spray/wall interaction in diesel selective catalytic reduction (SCR) systems. The work was performed with a commercial 3-hole pressure-driven injector dosing into a flow channel under typical diesel exhaust flow conditions. Infrared thermography captured the surface temperature of the wall around the impingement area with high temporal and spatial resolution. The resulting temperatures have been used for assessing the heat extracted from the wall. Phase Doppler Anemometry (PDA) was applied to measure the droplet sizes and velocities prior to the wall impingement, providing information on the kinetic properties of the impinging droplets. Based on these, the influence of the gas flow conditions on the heat transfer characteristics is deduced. The spray impingement leads to a substantial and rapid temperature drop on the wall, resulting in a maximum heat flux of several MW/m<sup>2</sup> during the injection duration. The spray cooling effect decreases with increasing exhaust gas flow rate due to the increased entrainment of spray

droplets in the flow prior to impingement. Increase in gas flow temperature affects the heat transfer by increasing the wall temperature. The shorter contact times in the rebound and thermal breakup regimes result in decreased spray/wall heat transfer.

## 4.1 Introduction

To comply with the stringent regulations as stated in Euro6 legislation, the NO<sub>x</sub> emissions of light and heavy-duty vehicles have to be reduced by up to 80% in respect of Euro5 [88]. Exhaust SCR system is a promising technique to reduce NO<sub>x</sub> emissions without sacrificing engine efficiency [1]. In most mobile applications, urea water solution (UWS) is used as an ammonia precursor because of its non-toxicity and convenience of storage. UWS is sprayed into the exhaust gas flow, followed by the evaporation of water from spray droplets. Thereafter, thermal decomposition and hydrolysis take place [1, 28]. The main challenges for the implementation of mobile urea-SCR systems include rapid decomposition [14, 15] and homogeneous distribution of urea [18] as well as mitigation of deposit formation [12, 19, 73]. Due to compact design requirements of the exhaust pipe and the relatively long time scales of urea thermal decomposition [7], the spray impingement on the exhaust pipe or on a mixer is unavoidable [28]. UWS spray impingement on the exhaust pipe wall or on a mixer can assist liquid evaporation and urea thermal decomposition on one side; on the other side leads to deposit formation, since spray impingement results in local cooling. As the wall temperature drops below a certain threshold, liquid film starts forming [27]. Temperature-dependent impact regimes are also decisive for the spatial distribution of the reducing agent. Evaporation from the wall film leads to further cooling and to increasing risk of deposit formation such as solid urea, biuret, cyanuric acid, ammeline, ammelide and melamine [10, 11, 27]. Incropera et al. [30] summarized different modes of evaporation occurring at a solid-liquid interface: free convection, nucleate boiling, transition boiling and film boiling. The importance of the Leidenfrost temperature, where the local heat flux is minimized, is



highlighted. The evaporation characteristics of urea-water solution have been recently considered due to the use of 32.5wt % urea-water solution as a liquid ammonia precursor in diesel exhaust systems. Musa et al. [4] derived the modified boiling curve, from droplet evaporation times on a heated surface as a function of the surface temperature, for a single UWS droplet. In the study, different regimes of boiling were observed and beyond the critical heat flux point two different patterns, fast evaporation and slow evaporation, were found. Wang et al. [5] and Musa et al. [4] found the multi-stage evaporation behavior of UWS droplets through conducting experiments in an electric furnace under quiescent conditions. The first stage is only water evaporation, following the  $D^2$  law. The second stage is characterized by micro explosion, the extent of which depends on the ambient temperature. After the complete depletion of liquid, white solid deposit remains at temperatures below 550 °C. Grout et al. [6] used synthetic schlieren method to visualize the liquid film evolution, and Mie scattering to measure the 2D liquid distribution in stream cross-sections under exhaust flow conditions. Through analyzing these consecutive distributions, the global spray evaporation rate was deduced. Birkhold et al. [27, 28] realized the importance of spray/wall interaction and included it into his systematic modelling of UWS injection. In the Kuhnke [29] model, the spray/wall interaction regime map was classified into four regimes: deposition, splash, rebound and thermal breakup based on the kinetic properties of the droplets, Mundo number  $K$ , and the temperature of the wall as displayed in Fig. 1.6. According to Kuhnke, the critical temperature at the non-wetting threshold was determined to be 1.1 for a variety of fluids, but Birkhold found it to be 1.4 (265 °C-280 °C) for urea-water solution. However, to the knowledge of the author, heat transfer characteristic of UWS spray/wall impingement under exhaust flow conditions have not been studied experimentally so far.

Heat transfer of spray impingement is significant in many fields of application, like fuel spray impingement, steel quenching and electronics cooling. They [57, 60, 63, 69, 71, 81, 84, 89] gave rise to the experimental methods used in this study. The present study is a comprehensive ex-

perimental analysis of the heat transfer characteristics of the impinging SCR spray under typical diesel exhaust flow conditions. Infrared thermography was introduced to assess the surface temperature of the wall with high temporal and spatial resolution around the impingement area. The resulting temperatures have been used for assessing the heat extracted from the wall. Phase Doppler Anemometry (PDA) was applied to measure the droplet sizes and velocities prior to the wall impingement, providing information on the kinetic properties of the impinging droplets.

## 4.2 Experimental setup and methods

Measurements were conducted in the flow lab, which was designed for the experimental investigation of SCR systems. Fig. 4.1 shows a schematic diagram of the flow lab. All measurements within this work were performed with dry air as exhaust flow. The dry air was taken from the pressurized air network. Thereafter, the gas flow rate is regulated according to a hot wire anemometer, and the target flow temperature is achieved by using the three heating units. Subsequently, the prepared gas flow passes through the injection channel assembly which consists of two optically accessible measurement chambers, each with four-directional optical access. In this work, the 2<sup>nd</sup> optical chamber of 80 mm by 80 mm in cross-section and 150 mm in length was used. Typical engine exhaust conditions have been selected, which are shown in the results and discussions section.

The urea dosing unit consists of a pressure system and a commercial SCR injector. The injector was mounted on the top of the small measurement chamber, 50° inclined to the gas flow direction. The injector was a 3-hole pressure-driven injector, operated at a pressure of 9 bar. The three nozzle holes of 190 μm diameter are evenly distributed on a 1.9 mm diameter circle. Previous shadow imaging experiments [90] which have been performed in the same laboratory exhibited that this injector produces a spray of three distinct spray cones. A previous study [44] has proved that water spray and UWS spray behave similarly in terms

of bulk spray properties. Thus, distilled water was used as the injected fluid in this work for the sake of simplicity. Future investigations with UWS injection will follow. For all results presented in this study, the injection duration was set at 60 ms. The time between two subsequent injections was chosen such that the thermal equilibrium between the plate and the surrounding gas flow was re-established.

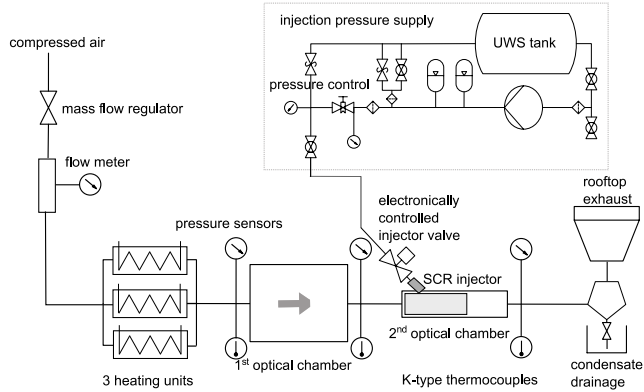


**Figure 4.1:** Schematic diagram of the flow lab

**Infrared thermography** temperature profiles on the spray-impinged plate were captured by the infrared camera, Cedip Jade III, with a 50 mm lens. The radiation detector is an indium antimonide (InSb) quantum detector that is sensitive in the 3.6 to 5.1  $\mu\text{m}$  wavelength range. It is cooled by a Stirling motor to 77 K. During the measurements, the IR camera recorded 150 frames per second at a resolution of  $320 \times 240$  pixels at 0.245 mm/pixel. Data acquisition was performed with the Altair software, version 5.8, from Cedip. The camera was calibrated with a traceable blackbody for the range of 5 to 500  $^{\circ}\text{C}$  at both low and high camera housing temperatures. The camera calibration process was performed by exposing the camera detector to a black body of different known temperatures at both low and high housing temperatures. The traceable black body used in the calibration process is Gemini R550

which allows for calibration of non-contact infrared thermometers over the temperature range  $30^{\circ}\text{C}$  to  $550^{\circ}\text{C}$ . The obtained calibration points have been linearly interpolated based on the housing temperature at which the actual measurements have been made. Thereafter, the interpolated calibration points have been fitted using a polynomial function in Matlab as shown in Fig. 4.2. Finally, the polynomial function have been used to convert the digital levels captured by the IR camera into temperatures.

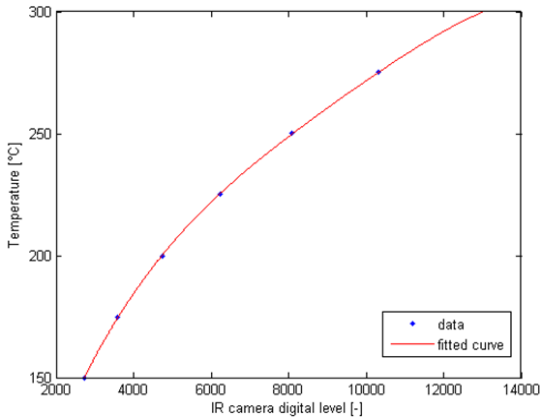


**Figure 4.2:** Infrared thermography camera calibration curve

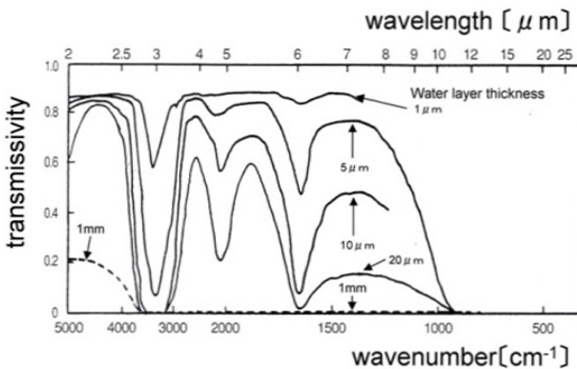


**Figure 4.3:** Water emissivity as a function of the wavelength varying with the water film thickness [91].

The spray-impinged wall is a 0.3 mm thin plate, placed 14 mm above the bottom of the flow channel. The thin plate is made of stainless steel type 304. Since water absorption varies with the water film thickness [91] (Fig. 4.3), it has been decided to measure the temperature profile of the rear surface of the plate. A calcium fluoride ( $\text{CaF}_2$ ) glass window with a high transmissivity in the mid-infrared range allows a non-intrusive optical access for the infrared camera. Due to the limited space underneath the channel, a gold coated mirror is added to redirect the infrared radiation to the camera as shown in Fig. 4.4.

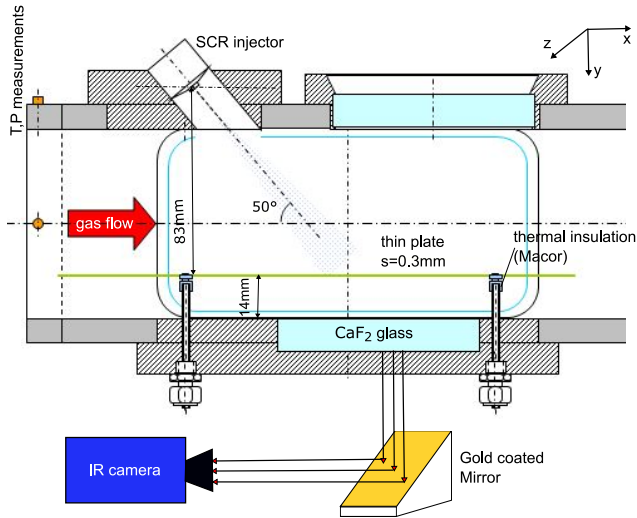


**Figure 4.4:** Experimental setup of infrared thermography in the flow channel.

The IR camera measures all radiation impacting on the detector, which includes the plate emission, the plate reflecting ambient emission, the  $\text{CaF}_2$  glass reflecting ambient emission, the  $\text{CaF}_2$  glass emission, the plate reflecting the  $\text{CaF}_2$  glass emission, the gold mirror emission, the  $\text{CaF}_2$  glass reflecting the mirror emission, the plate reflecting the mirror emission and the  $\text{CaF}_2$  glass reflecting the plate emission. The complete radiation balance of the infrared detector is displayed in Eq. 4.1. Thus, the material properties of the plate, the glass, and the mirror have to be

determined in the mid-infrared range to correct the measured temperature according to Eq. 4.1.

Air transmissivity in laboratory conditions is nearly 1 [92]. Thus, it is omitted in Eq. 4.1. The material properties were characterized with the IR camera, the black body and several calibrated thermocouples.

$$\begin{aligned}
 I_{camera} = & \varepsilon_{plate} \tau_{CaF_2} \rho_{mirror} I(T_{plate}) + \rho_{mirror}^2 \tau_{CaF_2}^2 \rho_{plate} I(T_{amb}) \\
 & + \rho_{mirror}^2 \rho_{CaF_2} I(T_{amb}) + \rho_{mirror} \varepsilon_{CaF_2} I(T_{CaF_2}) \\
 & + \rho_{mirror} \tau_{CaF_2} \rho_{plate} \varepsilon_{CaF_2} I(T_{CaF_2}) \\
 & + \varepsilon_{mirror} I(T_{mirror}) + \rho_{mirror} \rho_{CaF_2} \varepsilon_{mirror} I(T_{mirror}) \\
 & + \rho_{mirror} \rho_{plate} \tau_{CaF_2}^2 \varepsilon_{mirror} I(T_{mirror}) \\
 & + \rho_{mirror} \rho_{plate} \tau_{CaF_2} \rho_{CaF_2} \varepsilon_{plate} I(T_{plate})
 \end{aligned} \tag{4.1}$$

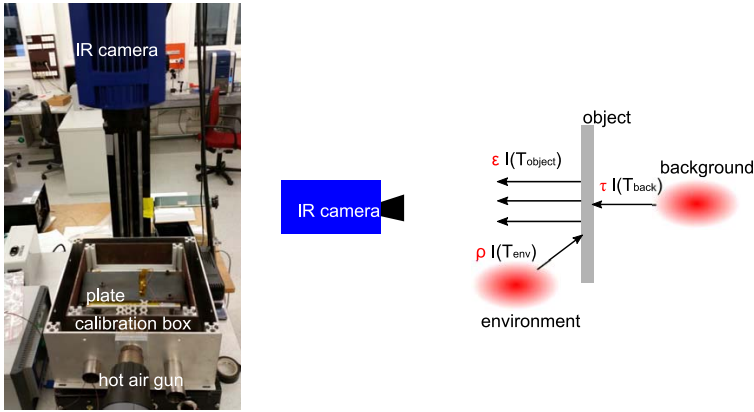


**Figure 4.5:** Setup to characterize the plate emissivity with the lid removed.

The plate emissivity was measured using a self-made box, as shown in Fig. 4.5, in which the plate was heated with a hot air gun. Several K-type thermocouples connected to a Fluke 52K/J thermometer monitored the temperature distribution inside the box and on the sample. When the plate reached a uniform temperature, the camera recording was started and the lid of the box was removed. The first pictures immediately after the lid removal were used to determine the emissivity. The process was

repeated for the entire temperature range of the plate expected in the experiment.

The measured radiation  $I_{camera}$  can be related to the black body radiation of known temperature which is given by the thermocouple to obtain the plate emissivity as shown in Eq. 4.2 [93].

$$I_{camera} = \varepsilon_{plate}I(T_{plate}) + \rho_{plate}I(T_{env}) + \tau_{plate}I(T_{back}) \quad (4.2)$$

where  $I(T_{plate})$  is the blackbody radiation of  $T_{plate}$ .

By heating the plate to different temperatures in a controlled way, the plate emissivity can be calculated according to Eq. 4.3 as the difference between the measurements.

$$\varepsilon_{plate} = \frac{I_{camera,2} - I_{camera,1}}{I(T_{plate,2}) - I(T_{plate,1})} \quad (4.3)$$

To measure transmissivity or reflectivity, the traceable blackbody was placed behind the plate or at a certain angle with respect to the plate, respectively, and was heated to several temperatures. The emissivity of the thin plate has been found to be  $\varepsilon_{plate} = 0.865$  and no transmission has been observed in the mid-infrared range of 3.6 to 5.1  $\mu\text{m}$ . The  $\text{CaF}_2$  transmissivity and reflectivity have been determined to be 94.6% and 5.4%, respectively. The mirror reflectivity is 99% and it has no transmission. The IR results shown in Sec. 4.4 were averaged over five single injection events.

**Phase Doppler Anemometry** (PDA) provided information on kinetic properties of droplets prior to the impinged wall. The setup measured the droplet velocities together with the droplet diameters, which allowed the determination of Mundo numbers. Mundo number, as described in Eq. 4.4, is the parameter defining the spray/wall interaction regime [28, 29].

$$K = \frac{(\rho D)^{0.75} U^{1.25}}{\sigma^{0.5} \mu^{0.25}} \quad (4.4)$$

where  $\rho$ ,  $D$ ,  $U$ ,  $\sigma$  and  $\mu$  denote the density, diameter, normal velocity, surface tension and dynamic viscosity of the droplets. The measure-

ments were performed at various locations across the centerline of the downstream spray cone at the height of 18 mm above the bottom of the channel.

### 4.3 Computation of the spray cooling flux by solving the inverse heat conduction problem

Having measured the rear surface temperature of the plate, the inverse heat conduction problem was solved to determine the front surface temperature and estimate the spray cooling heat flux.

$$\frac{\partial^2 T}{\partial x^2} + \frac{\partial^2 T}{\partial y^2} + \frac{\partial^2 T}{\partial z^2} = \frac{\rho c_p}{k} \frac{\partial T}{\partial t} \quad (4.5)$$

It can be reduced to a 1D heat conduction problem by assuming negligible lateral heat conduction compared to the normal heat conduction on this timescale, which is verified by [59, 70] and the results.

$$\frac{\partial^2 T}{\partial x^2} = \frac{1}{\alpha} \frac{\partial T}{\partial t} \quad (4.6)$$

where  $\alpha$  is the thermal diffusivity of the stainless steel type 304. Initial condition:

$$T_{t=0} = T(y, 0) \quad (4.7)$$

Boundary conditions:

$$T_{y=d} = T(d, t) \quad (4.8)$$

$$-k \frac{\partial T}{\partial y} \Big|_{y=d} = q_{rad} + q_{conv} = \epsilon \sigma (T_s^4 - T_a^4) + h(T_s - T_g) \quad (4.9)$$

$$k \frac{\partial T}{\partial y} \Big|_{y=0} = q_{spray} \quad (4.10)$$



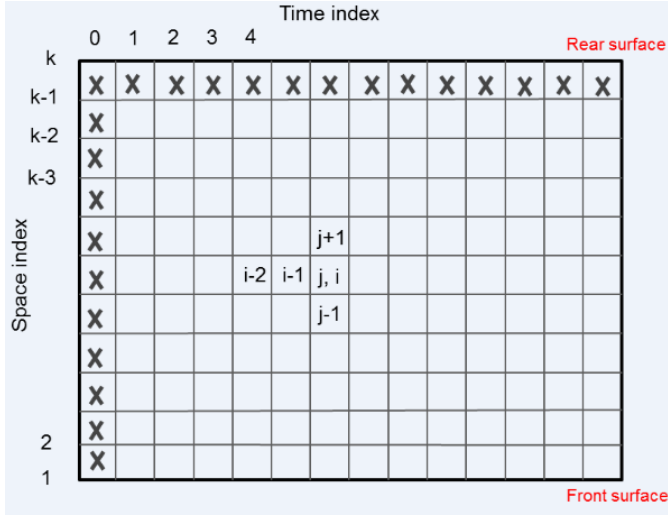


**Figure 4.6:** Schematic illustration of 1D inverse heat conduction problem solved with finite element scheme [94].

where  $d$ ,  $k$ ,  $T_s$ ,  $\varepsilon$ ,  $\sigma$ ,  $T_a$  and  $T_g$  denote the plate thickness, the plate thermal conductivity, rear surface temperature, the emissivity of the plate, Stephan Boltzman's constant, the ambient temperature and the surrounding flow temperature;  $t$  is time;  $y$  is the normal direction of the plate;  $T$  is the temperature of any node across the plate and  $q_{spray}$  is the spray heat flux. The initial plate temperature across the thickness and one boundary temperature and heat flux are known. Therefore, the front surface heat flux is determined by solving the 1D inverse heat conduction problem with finite element scheme as indicated in Fig. 4.6. The problem is discretized in time according to the IR camera frame rate, 150 steps per second. The 0.3 mm plate is discretized into 30 steps based on the criteria that the thin layer could be considered of uniform temperature if the Biot number is less than 0.1.

$$\frac{(T_{j+1}^i - T_j^i)/\Delta y - (T_j^i - T_{j-1}^i)/\Delta y}{\Delta y} = \frac{1}{\alpha} \frac{(T_j^i - T_j^{i-1})}{\Delta t} \quad (4.11)$$

Starting from the rear surface and the injection beginning, the neighboring node temperature is solved according to the previous equation. Finally, the whole matrix in Fig. 4.6 is solved.

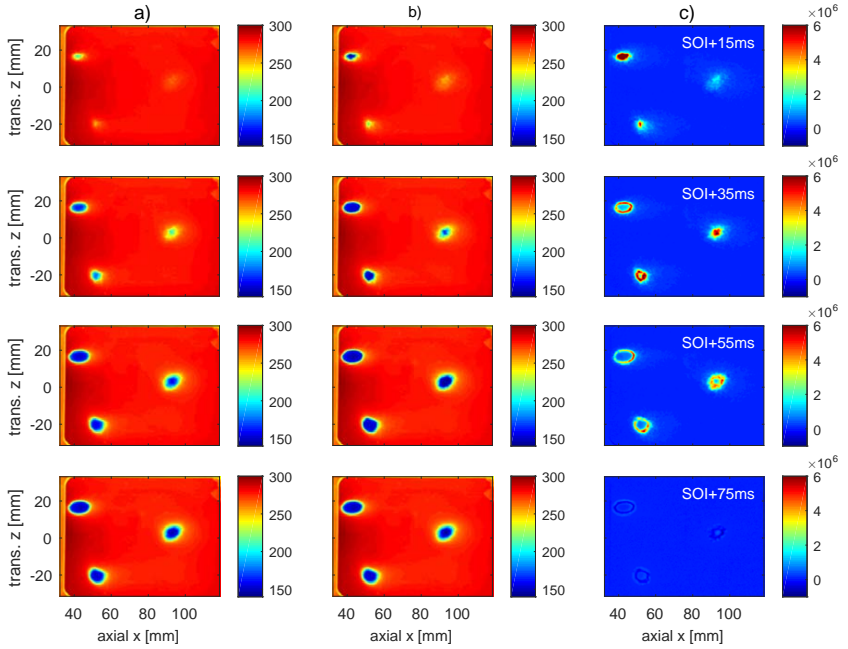
$$q_{spray,i} = k \frac{\partial T}{\partial y} \Big|_{y=0} = k \left( \frac{T_2^i - T_1^i}{\Delta y} - \frac{\Delta y}{2\alpha} \frac{T_1^i - T_1^{i-1}}{\Delta t} \right) \quad (4.12)$$

The inverse heat conduction model allowed obtaining the front surface temperature and the front surface heat flux at any given time during the experiments, which are shown in the results and discussions section.

## 4.4 Results and discussions

### 4.4.1 General heat transfer characteristics

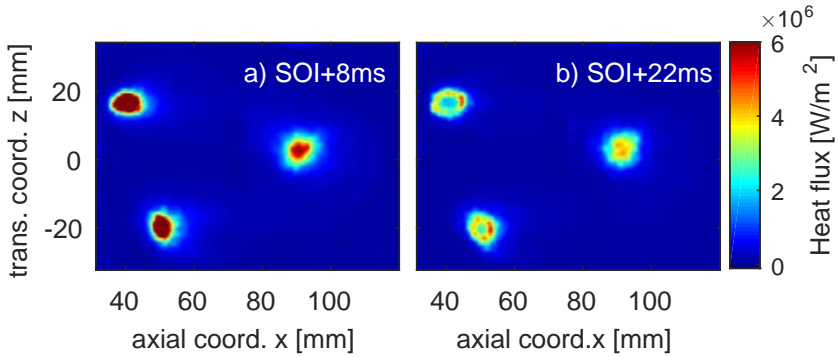
The measurements were done under various conditions typical for diesel exhaust. The images recorded by the camera during the experiments were post-processed in Matlab according to Sec. 4.2 and Sec. 4.3. Fig. 4.7a shows the post-processed rear surface temperatures at different time instants after the electronic start of injection (SOI), Fig. 4.7b indicates the front surface temperature calculated as described above, while Fig. 4.7c displays the front surface heat flux. The x and z coordinates indicate the measurement locations with respect to the injector nozzle exit. The temperature pattern on the thin plate shows that the cooling areas are isolated from each other and concentrated in elliptical shapes, which confirms that the spray of the 3-hole pressure-driven injector has three distinct spray cones. Later in this section, they are referred to as the upstream, middle and downstream cone depending on the location in the axial flow direction. In each of the spray cone impingement regions, there is a substantial temperature drop (Fig. 4.7a and b). On the front surface (Fig. 4.7b), the temperature drop is up to 150 °C, and after closing the injector it slowly recovers. Local cooling in the impingement regions occurs with a time difference, which is proportional to the cone travelling distance from the injector nozzle. The upstream cone with the shortest



**Figure 4.7:** Spatial distribution of a) the measured rear surface temperature [ $^{\circ}\text{C}$ ], b) the calculated front surface temperature [ $^{\circ}\text{C}$ ] and c) the calculated front surface heat flux [ $\text{W}/\text{m}^2$ ] (flow conditions:  $300^{\circ}\text{C}$ ,  $200\text{ kg}/\text{h}$ ).

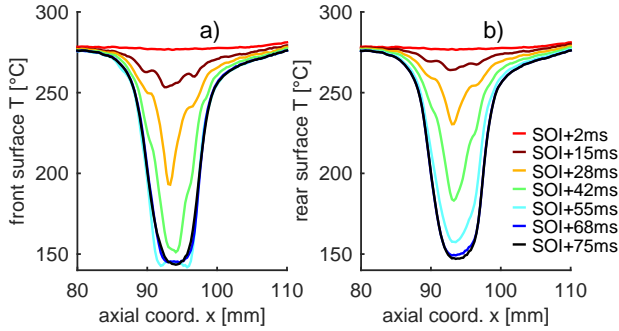
traveling distance is cooled the earliest and spreads over the most along the axial flow direction. The spray cooling on the front surface is strong (as computed with Eq. 4.12) on the millisecond timescale, resulting in heat fluxes of several megawatts per square meter during the injection.

Fig. 4.8 displays the front surface heat flux at different time instants after SOI for the flow condition  $300^{\circ}\text{C}$ ,  $100\text{ kg}/\text{h}$ . The cooling starts in the spray cone core region. Here, heat flux peak values are up to  $10\text{ MW}/\text{m}^2$ . This is mainly due to the evaporation of the impinging droplets. With evolving time, the plate temperatures in the core decrease considerably to  $160^{\circ}\text{C}$  which is similar to the transition temperature from nucleate boiling to free convection according to [4]. Thus, heat fluxes in the core decrease. However, in the near periphery of the core the plate temperatures are still high. Therefore, the spray cooling front (strong evaporation) moves radially to the periphery at SOI+22 ms.



**Figure 4.8:** Spatial distribution of the front surface heat flux [ $\text{W}/\text{m}^2$ ] a) 8 ms after SOI b) 22 ms after SOI (flow conditions:  $300^\circ\text{C}$ ,  $100\text{ kg}/\text{h}$ ).

The temperature of the plate is quite uniform before injection, along the surface and across the thickness, as indicated by the SOI+2 ms curve in Fig. 4.9. This temperature is slightly lower than the gas flow temperature, due to the heat loss from the optical chamber to the surrounding environment. The lowest temperature reached on the front surface is about  $145^\circ\text{C}$  (SOI+68 ms). The spray firstly cools the front surface, and then the temperature drop propagates along the thickness of the plate by heat conduction. Thus, the temperature profile on the rear surface lags behind the front surface temperature as shown in Fig. 4.9b. At SOI+15 ms, the maximum temperature drop on the front surface is about  $24^\circ\text{C}$  in the center of the impingement region. Thereafter, the temperature gradient firstly increases and then decreases, reaching a maximum between SOI+15 ms and SOI+28 ms. Since after the electronic SOI it takes some time for the spray to get fully developed and reach the maximum impinging mass flow rate. However, after a certain time period the temperature difference between the plate and spray reduces, thus the driving force of heat transfer is weakened. After SOI+68 ms (the injector valve is closed), the front surface temperature stays constant and the rear surface temperature continues to decrease but with a lower rate. It's evidenced again that the cooling effect remains relatively concentrated in the spray impinged area while the temperature of the non-impact area stays unaffected. The lateral heat conduction is not significant in the ob-



**Figure 4.9:** a) Plate front surface temperature and b) plate rear surface temperature profiles across the centerline ( $z = 2.3$  mm) of the downstream spray cone at different times after the electronic SOI (flow conditions:  $300\text{ }^{\circ}\text{C}$ ,  $200\text{ kg/h}$ ).

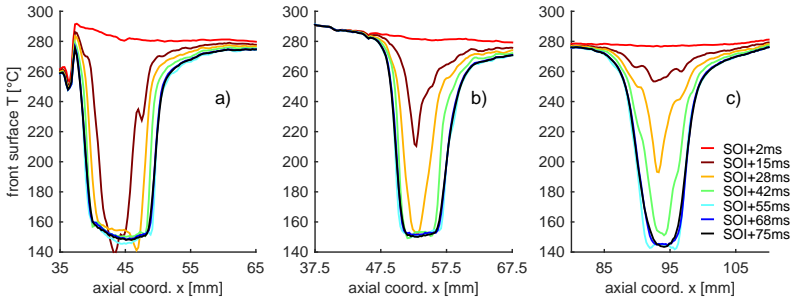


**Figure 4.10:** Temperature profiles across the centerline of each spray cone on the front surface at different times after the electronic SOI a) Upstream cone ( $z = 15.7$  mm), b) middle cone ( $z = -20.6$  mm) and c) downstream cone ( $z = 2.3$  mm) (flow conditions:  $300\text{ }^{\circ}\text{C}$ ,  $200\text{ kg/h}$ ).

servation time range comparing to the normal one, as can be seen by the diminishing temperature gradients at the periphery locations ( $x < 85$  mm and  $x > 105$  mm).

The spray footprint shows three elliptic areas as indicated in Fig. 4.7. Fig. 4.10 depicts the front surface temperature profiles across the centerline of each spray cone over time. At SOI+2ms, no droplets have arrived at the plate yet, the temperature is quite uniform across the whole surface area. The minor differences are due to the increasing heat losses to the environment along the optical chamber. The upstream cone,

which travels the least distance in the hot flow before reaching the plate, spreads over the most along the axial flow direction. At SOI+15 ms, the upstream area is cooled to the lowest temperature of the injection duty cycle, whereas the downstream cone is only marginally affected. Thereafter, the upstream cone maintains the lowest temperature 150 °C for almost 60 ms. This lowest temperature is approached also by the middle and downstream cones. The middle cone is earlier than the downstream cone since it has the shorter distance from the injector. Similar trend is observed in Fig. 4.7c, where the heat flux extracted by the upstream cone reaches the maximum at SOI+15 ms, and the heat flux peak of the downstream cone is evidenced at SOI+35 ms.

#### **4.4.2 Influence of the gas flow conditions on the heat transfer characteristics**

Fig. 4.11 displays the temperature averaged over different sizes of area for the downstream spray cone. The curve at  $r = 2.7$  mm shows the core behavior and at  $r = 5.4$  mm the overall behavior of the cone. Different mass flow rates are set to 100, 200, 300 kg/h at the same gas flow temperature 300 °C. The steady-state temperature on the plate before injection increases with increased gas flow rate, which implies that the heat loss to the ambient gets less significant with respect to the incoming heat flux. From SOI+62 ms to SOI+68 ms, there is a sudden temperature rise in the plate, especially discernible at high flow rates. This is due to the fact that the injector closes between these two time instants. At 300 °C and 200 kg/h, only limited area around the spray cone center is cooled down to 150 °C, and the overall downstream spray cone is cooled to 200 °C on average. In the case of weaker flow rate, the spray core and the overall spray are cooled in a similar manner to about 160 °C. At the higher flow rate of 300 kg/h, the overall spray cone is only slightly affected. The spray cooling effect decreases with increasing gas flow rate, which is more pronounced in the overall spray cone. Furthermore, the initial temperature gradient is less steep for higher flow rates.

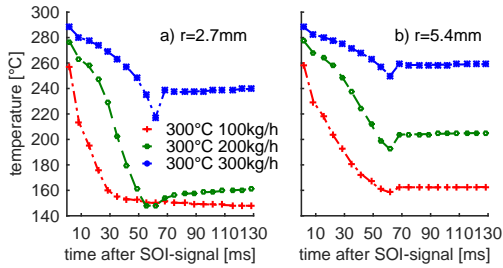


**Figure 4.11:** Temperatures averaged over different sizes of area around the downstream spray cone center for different flow conditions with constant  $T$  and different  $\dot{m}$  a)  $r = 2.7$  mm, b)  $r = 5.4$  mm.

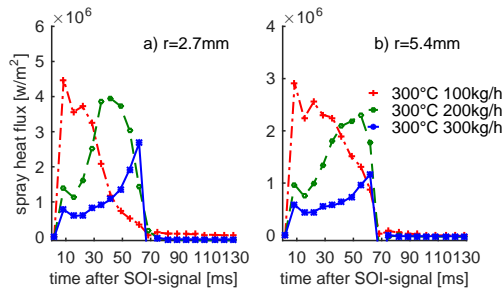


**Figure 4.12:** Front surface heat flux averaged over different sizes of area around the downstream spray cone center for different flow conditions with constant  $T$  and different  $\dot{m}$  a)  $r = 2.7$  mm, b)  $r = 5.4$  mm.

Therefore, the spray heat flux peak of the same region is increasing in magnitude with decreasing gas flow rate as shown in Fig. 4.12. At 300 °C and 100 kg/h it amounts up to 4.5 MW/m<sup>2</sup> on average in the spray core region, whereas it only reaches 3 MW/m<sup>2</sup> at 300 °C and 300 kg/h. The peak heat flux is also reached earlier in the case of lower flow rate. The plate temperatures before impingement are similar for all cases investigated. Consequently, it is concluded that the plate temperature is not the sole factor that determines the spray/wall interaction regime. The kinetic properties of the spray droplets play an important role according to Kuhnke [29] and the local spray mass flux is also decisive as reported in the steel quenching application [84, 95].

If the gas flow rate of 200 kg/h is kept constant but the gas flow temperature is varied, the heat flux decreases greatly with increasing gas

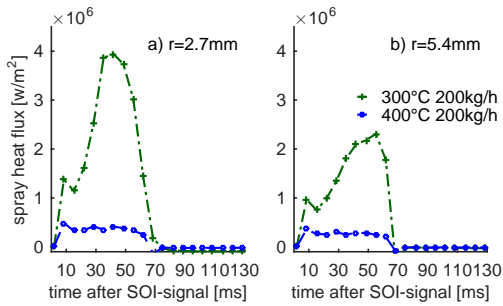


**Figure 4.13:** Front surface heat flux averaged over different sizes of area around the downstream spray cone center for different flow conditions with constant  $\dot{m}$  and different  $T$  a)  $r = 2.7$  mm, b)  $r = 5.4$  mm.

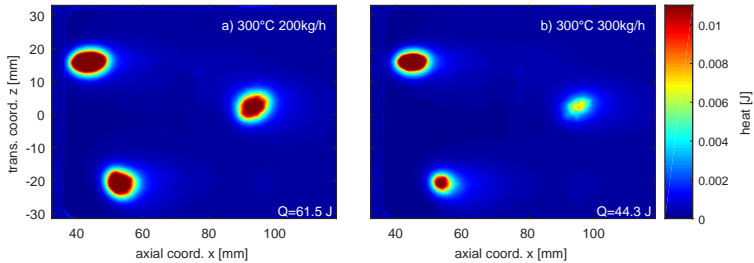


**Figure 4.14:** Spatial distribution of heat exchanged during one injection event a) 300 °C, 200 kg/h, b) 300 °C, 300 kg/h

flow temperature from 300 °C to 400 °C as indicated by Fig. 4.13. At 300 °C and 200 kg/h the peak heat flux is up to 4 MW/m<sup>2</sup> , while it reaches at most 0.5 MW/m<sup>2</sup> at 400 °C without a clear peak. Heating up the exhaust pipe is a solution to limit the cooling on the exhaust pipe wall, thus avoiding deposit formation. However, more active heat transfer surfaces should be added in order to deliver more heat to facilitate the evaporation and thermal decomposition of the urea-water solution.

Should the heat flux be integrated over time during the spray cooling phase, the spray/wall heat transferred during a single injection can be deduced. Fig. 4.14 shows the heat transferred locally at two different flow conditions. In addition, the integrated heat transferred from the plate to the spray is displayed in the right bottom corner of Fig. 4.14. If the gas flow rate is increased from 200 kg/h to 300 kg/h, the total amount



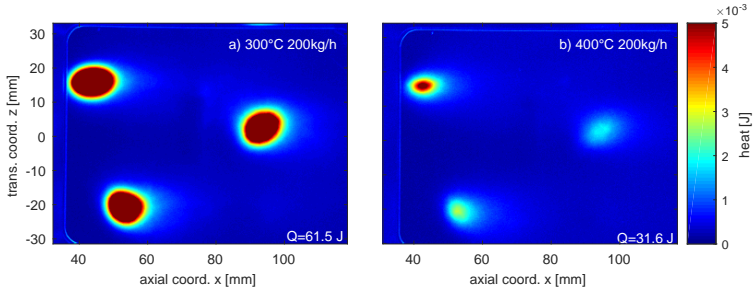


**Figure 4.15:** Spatial distribution of heat exchanged during one injection event a) 300 °C, 200 kg/h, b) 400 °C, 200 kg/h

of heat transferred declines by about 30 % (from 61.5 J to 44.3 J). For the three different spray cones, the gas flow has the biggest influence on the downstream cone, while affecting the upstream cone only moderately. This is due to the fact that the downstream cone has the longest traveling distance before impinging on the thin plate, therefore more droplets could be entrained by the increasing gas flow.

Fig. 4.15 displays that if the gas flow temperature is increased from 300 °C to 400 °C, the total amount of heat transferred decreases by about 50 % for the whole spray. The increase in gas flow temperature influences the heat transfer by changing the wall temperature during spray/wall interaction. For this reason, the influence on the three spray cones is quite similar. The spray/wall interaction regimes are classified into four different regimes depending on the kinetic properties of the droplets, described by Mundo number  $K$ , and the critical temperature ratio as shown in Fig. 1.6. The critical transition temperature for UWS was determined to be 265 °C - 280 °C by experiments of Birkhold et al. [27]. In our single droplet experimental work, the transition temperature ratio +for distilled water was found to be 1.42 and increased with the concentration of urea in the solution. As shown in Fig. 4.16, over 95 % of droplets possess Mundo numbers ranging from 0 to 150 regardless of gas flow conditions. As the gas flow temperature is increased from 200 °C to 400 °C, the temperature ratio is ranging from 1.27 to 1.8. Thus, the principal interaction behavior is deposition at gas flow temperatures of

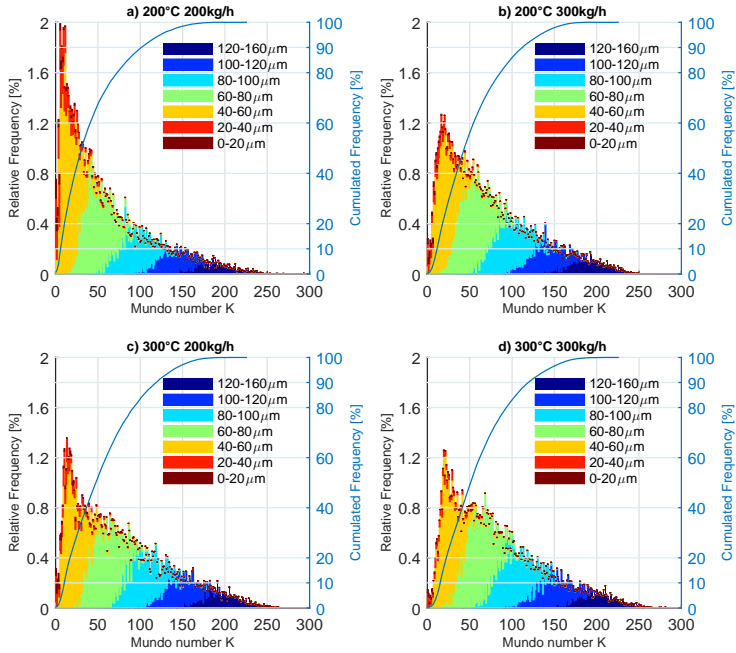


**Figure 4.16:** Mundo number K estimated from PDA measurements at different flow conditions along the downstream cone centerline at 18 mm above the bottom of the channel.

200 °C and 300 °C. At the gas flow temperature of 400 °C, the spray/wall interactions for over 95 % of droplets are in the rebound and thermal breakup regimes (according to Fig. 1.6). Due to the short contact time of rebound and thermal breakup, the spray/wall heat transfer declines greatly in the case of Fig. 4.15b).

As displayed in Fig. 4.16, large droplets have high Mundo numbers, and small droplets have low Mundo numbers. At the same gas temperature, increasing the gas flow rate flattens out the Mundo distribution, whereas the maximum Mundo number remains constant. This is mainly due to the relatively small droplets entrained by the increasing gas flow. At the same flow rate, increasing the gas flow temperature means enhanced evaporation. Thus, the small diameter frequencies decrease.

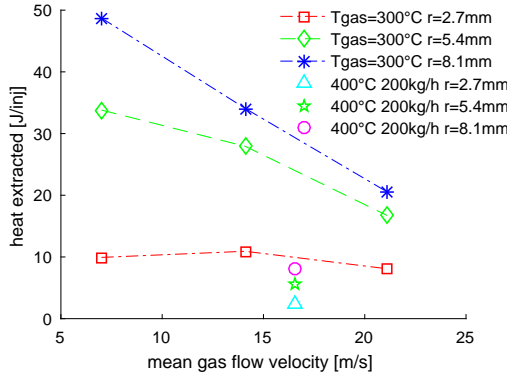


**Figure 4.17:** Heat extracted by the spray cone area of different sizes at various gas flow conditions.

Fig. 4.17 compares the heat transferred per injection during the spray/wall interaction at different exhaust-similar conditions. Should the flow temperature be kept constant at 300 °C, increasing the mean gas flow velocity does not change too much the heat transferred in the spray core area of  $r = 2.7$  mm. PDA measurements have shown that bigger droplets with higher momentum are more often in the center of the spray than in the periphery. This explains why the core is more inert to the change in gas flow momentum. If the area is doubled, the dependency of heat transferred in this area on the mean gas flow velocity gets stronger, especially from 200 kg/h to 300 kg/h. The flow momentum is proportional to the square of the gas flow velocity; therefore droplets of higher momentum could be entrained. If the area is extended to  $r = 8.1$  mm, the heat transferred declines linearly as a function of the mean gas flow velocity. On the other side, keeping the gas flow rate constant, 200 kg/h, and increasing the gas temperature from 300 °C to 400 °C, the heat transferred drops substantially for all areas due to the change in the spray/wall interaction regimes as stated in Fig. 4.15. The heat transferred at 300 °C and 200 kg/h (61.5 J) is able to superheat and evaporate about 21 % of the total injected mass based on the assumption that the arriving droplets temperature is 60 °C. In order to enable fast evaporation, thermal decomposition and mitigate deposit formation in such systems, enhancing the heat transfer plays an important role. This could

be achieved by changing the exhaust pipe material from stainless steel to a material of higher thermal diffusivity or heating the exhaust pipe wall above the critical transition temperature. In the latter case, shifting the spray/wall interaction regime from deposition to rebound and thermal breakup decreases the heat transferred from wall to droplets, therefore it is highly recommended that more active impingement surfaces with heating should be added to act like an active evaporator.

## 4.5 Summary

The spray cooling effect on the exhaust pipe wall is evidenced and quantified by infrared thermography. The kinetic properties of droplets prior to the wall are characterized by PDA. The experiments with a commercial 3-hole pressure-driven ( $P=9$  bar) injector at exhaust-similar conditions reveal the following:

1. The spray has three distinct spray cones. The spray cooling footprints are isolated from each other and concentrated in elliptical shapes. The cooling effect on the exhaust pipe wall is local and the lateral heat conduction plays a minor role on the relevant time scale.
2. The spray impingement leads to a substantial temperature drop. At flow conditions of  $300\text{ }^{\circ}\text{C}$  and  $200\text{ kg/h}$ , the temperature drop on the  $0.3\text{ mm}$  stainless steel plate is up to  $150\text{ }^{\circ}\text{C}$  (injection duration  $60\text{ ms}$ ) in all three impingement areas. Cooling peaks have time differences proportional to the distances from the injector nozzle exit.
3. The spray cooling on the front surface is instantaneous, on the millisecond timescale, resulting in a heat flux of several  $\text{MW/m}^2$ . The cooling starts in the spray cone core of the impingement region. Thereafter, the cooling front moves radially to the periphery.
4. The spray cooling effect decreases with increasing exhaust gas flow rate. Thus, the initial temperature gradient is less steep for higher

gas flow rates. The influence of the gas flow rate is less pronounced in the spray core impingement area. For a single injection, at 300 °C increasing the gas flow rate from 200 kg/h to 300 kg/h results in 30 % lower heat transferred from the plate to the spray as a result of enhanced droplet entrainment in the gas flow prior to the impingement.

5. Changes in gas flow temperature influence the spray/wall interaction regimes by changing the wall temperature. At 200 kg/h, increasing the gas flow temperature from 300 °C to 400 °C leads to a 50 % decrease of the transferred heat, mainly due to the shift in spray/wall interaction regimes from deposition to rebound and thermal breakup.
6. The spray/wall heat transfer is not only dependent on the wall temperature, but also on the kinetic properties of the droplets. For 95 % of droplets Mundo numbers range from 0 to 150 regardless of gas flow conditions, which implies that the principal interaction behavior is deposition below the critical wall temperature.



# 5 Heat transfer characteristics of sequential urea-water spray impingement events

Parts of this chapter are published in: Y. Liao, P. Dimopoulos Eggenchwiler, R. Furrer, M. Wang, and K. Boulouchos, "Heat transfer characteristics of urea-water spray impingement on hot surfaces," *International Journal of Heat and Mass Transfer*, vol. 117, pp. 447-457, 2018.

## Abstract

This study presents an investigation of the heat transfer characteristics of the urea-water spray impingement on a stainless steel plate under typical exhaust flow conditions. The rear side temperature of the spray-impinged plate is measured by infrared thermography with high temporal and spatial resolution. The spray-impinged side temperature and heat flux distributions are computed by solving the 3D inverse heat conduction in the plate with the sequential function specification method. Measurements have shown that the instantaneous impinged plate temperature determines the spray impingement heat transfer. Based on the plate temperature, different regimes (film boiling, transition boiling and nucleate boiling) are identified. The critical heat flux value and temperature found are in good agreement with the trend in previous studies.

## 5.1 Introduction

To comply with the stringent regulations, the NO<sub>x</sub> emissions of light and heavy-duty vehicles have to be reduced significantly. Urea-SCR using ammonia as the reducing agent is a promising technique to reduce NO<sub>x</sub> emissions without sacrificing engine efficiency [1]. In most applications, urea water solution (UWS) is injected into the exhaust gas flow as an ammonia precursor because of its non-toxicity. Due to compact design requirements of the exhaust pipe, the spray impingement on the exhaust pipe or on a mixer is unavoidable [28, 79]. The UWS spray impingement leads to local cooling on the wall [27, 79], and thereafter wall film formation [6, 27]. Evaporation from the liquid film leads to further cooling and to increasing risk of deposit formation [10, 28, 96]. Several application-oriented papers have clearly pointed out detrimental effects of solid deposits in real applications [12, 73, 97]. According to Kuhnke [29] and Liao et. al. [79], temperature-dependent impingement regimes are decisive for the spray/wall heat transfer. Different modes of pool boiling occurring at a solid-liquid interface have been summarized by Incropera et al. [30]: free convection boiling, nucleate boiling, transition boiling and film boiling according to the wall temperature. The critical heat flux point (CHF, 130 °C), between the nucleate boiling and transition boiling, has a heat flux exceeding 1 MW/m<sup>2</sup> for water at atmospheric pressure. The Leidenfrost point, where the heat flux is minimized in film boiling, is located at 220 °C. Heat transfer characteristics of the water spray impingement have been investigated in [64–70]. Yao et al. [65] performed a dimensional analysis and introduced the characteristic velocity (liquid mass flux over density) to define the spray Weber number ( $We_s$ ) as a measure of the inertia of the spray as a whole. The dependency of the spray/wall heat transfer on the spray mass flux and droplet diameter has been identified, leading to an empirical correlation of the Leidenfrost temperature based on the spray Weber number. In a following study [71], Al-Ahmadi and Yao presented correlations for the Leidenfrost and critical heat flux (CHF) points in function of the local mass flux for industrial nozzles with mass fluxes ranging from 1.7 to



30 kg/m<sup>2</sup>s. Again, it has been highlighted that the Leidenfrost and CHF points have a stronger dependency on the local mass flux than on the droplet velocity and size. It should be taken into account that industrial nozzles in general produce relatively large droplets (350 μm) of moderate velocities (13–15 m/s), as reported by Wendelstorf et al. [66]. In addition to the water impact flux, Wendelstorf et al. [66] introduced the temperature difference in the analytic correlation of the heat transfer coefficient. Estes and Mudawar [67] provided correlations of the critical heat flux to the spray mass flux and the Sauter mean diameter (SMD) for full cone sprays. The results reveal that the CHF value increases with increasing mass flux and decreasing droplet diameter. For sprays having a local mass flux of 30 kg/m<sup>2</sup>s and SMD of 150 μm, the CHF reaches about 1 MW/m<sup>2</sup>. Jia et al. [68] conducted experiments with a multi-nozzle spray system which provided variable mass fluxes ranging from 0.156 to 1.20 kg/m<sup>2</sup>s and droplets around 30 μm. It has been found that for water spray cooling the critical heat flux increases with the mass flux, reaching about 2 MW/m<sup>2</sup> at 1.2 kg/m<sup>2</sup>s. The CHF temperature increases almost linearly with the mass flux, being 145 °C at 1.2 kg/m<sup>2</sup>s. The addition of sodium dodecyl sulfate in water broadens the CHF temperature range. However, the exact reason of the broadening is not clear. Dou et al. [70] confirmed the influence of water mass flux on the Leidenfrost temperature and critical heat flux. Increase in water injection pressure (leading to smaller droplets) shifts the CHF and Leidenfrost points to higher temperatures. The empirical correlations for the critical heat flux and the transition boiling regime have been obtained as a function of Sauter mean diameter, local water flux, surface temperature, and physical properties of water and vapor. For sprays with a water injection pressure of 5 bar and local mass flux of 10 kg/m<sup>2</sup>s, the critical heat flux is found to be 1 MW/m<sup>2</sup>. To our knowledge so far, only Musa et al. [4] have examined the urea-water single droplet impact on elevated temperature surfaces. Based on the experiments, the modified boiling curve was derived, exhibiting a higher CHF temperature, 180 °C, and a relatively flat behavior around the Leidenfrost point. In the meantime, two different patterns in the transition and film boiling regimes were identified, which

were assumed to be caused by the processes involved in urea thermal decomposition [11]. The complex nature of spray impingement on hot surfaces and the uncertainty of urea water solution make it very difficult to predict the spray wall heat transfer in real applications. Numerical simulation efforts [27, 35, 45, 98] have deliberately pointed out that there is a lack of experimental data concerning UWS spray wall heat transfer. The present study is a comprehensive experimental analysis of the heat transfer characteristics of the SCR spray wall impingement under typical diesel exhaust flow conditions. Infrared thermography has been applied to measure the rear surface temperature of the impinging wall with high temporal and spatial resolution. Different boiling modes as well as the CHF and Leidenfrost temperatures have been identified from the temporal gradients of the surface temperatures. Finally, the measured rear surface temperatures have been used to compute the spray cooling heat flux by solving the 3D inverse heat conduction problem (IHCP) with the function specification method.

## 5.2 Experimental setup and methods

Measurements were conducted in the flow channel, which was designed for the experimental investigation of thermo-fluid properties of UWS sprays in general and the impingement processes in particular. The schematic diagram of the flow channel has been shown in Sec. 4.2. All measurements within this work were performed with dry heated air as exhaust flow. The urea-water spray was introduced by a commercial SCR injector, mounted  $50^\circ$  inclined with respect to the gas flow direction, in a channel part with a quadratic 80 mm by 80 mm cross section equipped with various optical accesses. The injector has 3 nozzles with  $190\ \mu\text{m}$  diameter evenly located on a 1.9 mm diameter circle. Operated at 9 bar, the static flow rate is 7.2 kg/h. For all results presented in this chapter, the injection frequency was set to 2 Hz. The standard injection duration in this study was set at 100 ms resulting in 0.2 g UWS per injection. For studying the impingement process a plate was introduced in the channel 14 mm above and parallel to the channel wall. Thus the

gas flow wetted the upper (impinging plate surface) as well as the lower plate surface providing stable thermal boundary conditions. The injection commenced once the thermal equilibrium between the plate and the surrounding gas flow was achieved. The plate, consisting of stainless steel type 304, had 0.7 mm thickness. Temperature profiles on the impinging plate were captured by the infrared camera, Infratec ImageIR 8300 hp, with a 50 mm lens. The radiation detector is an InSb quantum detector that is sensitive in the 2 to 5.7  $\mu\text{m}$  wavelength range. It is cooled by a Stirling motor to 77 K. During the measurements, the IR camera recorded 200 frames per second with a resolution of  $640 \times 512$  pixels at 0.149 mm/pixel. Since water absorption varies with the water film thickness [91], it was decided to measure the temperature profile of the rear surface of the plate. A calcium fluoride ( $\text{CaF}_2$ ) glass window with a high transmissivity in the mid-infrared range allows a non-intrusive optical access for the infrared camera. Due to the limited space underneath the channel, a gold coated mirror is added to redirect the infrared radiation to the camera as shown in Fig. 5.1. The IR camera measures all radiation impacting on the detector, which includes the plate emission, the plate reflecting ambient emission, the  $\text{CaF}_2$  glass reflecting ambient emission, the  $\text{CaF}_2$  glass emission, the plate reflecting the  $\text{CaF}_2$  glass emission, the gold mirror emission, the  $\text{CaF}_2$  glass reflecting the mirror emission, the plate reflecting the mirror emission and the  $\text{CaF}_2$  glass reflecting the plate emission. The complete radiation balance of the infrared detector is displayed in Eq. 4.1. Thus, the material properties of the plate, the glass, and the mirror have to be determined in the mid-infrared range to correct the measured temperature according to Eq. 4.1.

Air transmissivity in laboratory conditions is nearly 1 [92]. Thus, it is omitted in Eq. 4.1. The material properties were characterized with the IR camera, a calibrated blackbody and several calibrated thermocouples as described in [79]. The emissivity of the thin plate was found to be  $\varepsilon_{plate} = 0.865$  and no transmission was observed in the mid-infrared range. The  $\text{CaF}_2$  transmissivity and reflectivity have been determined to be 94.6% and 5.4%, respectively. The mirror reflectivity is 99% and it has no transmission.

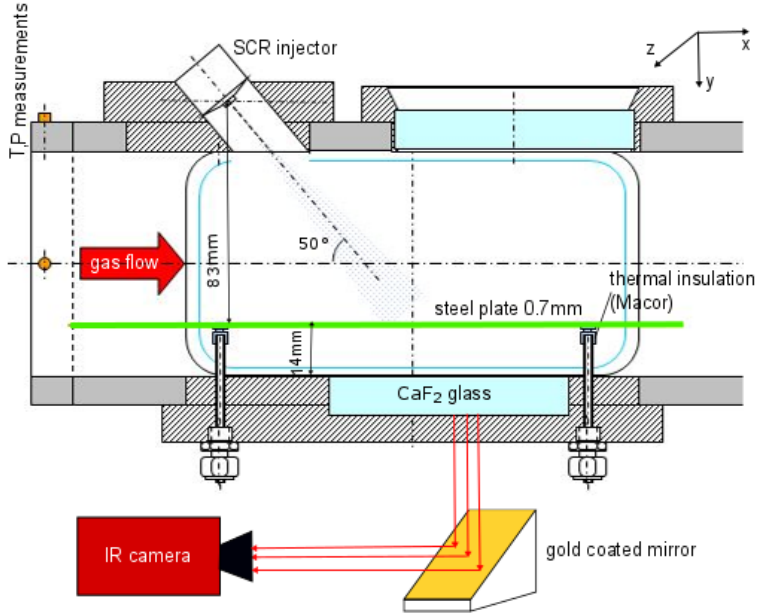


**Figure 5.1:** Experimental setup of infrared thermography in the flow channel

### 5.3 Solution of 3D inverse heat conduction problem

Having measured the rear surface temperature of the plate, the 3D inverse heat conduction problem (IHCP) was solved to determine the front surface temperature and the spray cooling heat flux. Inverse heat conduction problem is a so-called "ill-posed problem", because it is especially sensitive to measurement inaccuracy. There are several methods developed to cope with the IHCP, including function specification method, regularization method, trial function method, conjugate gradient method and filter form method [94]. In the present work, the sequential function specification method has been chosen due to better computational efficiency than the whole domain function specification method.



Assuming a transfer matrix  $A$  is used for the specified function,  $q$  could be written in the following way:

$$q = A\beta, A = \begin{bmatrix} A(1) \\ A(2) \\ \vdots \\ A(r) \end{bmatrix}, \beta = \begin{bmatrix} q_1(M) \\ q_2(M) \\ \vdots \\ q_I(M) \end{bmatrix} \quad (5.5)$$

$A(i)$  is an  $I \times I$  identity matrix by assuming the heat flux matrix to be temporarily constant. The calculated temperature can now be written as:

$$T = T|_{\beta=0} + Z\beta, Z = XA \quad (5.6)$$

Least square method is used to compare the estimated  $T$  to measured data  $Y$ . The problem is then to minimize the objective function below:

$$S = (Y - T|_{\beta=0} - Z\beta)^T(Y - T|_{\beta=0} - Z\beta) \quad (5.7)$$

$\hat{\beta}$ , the estimated heat flux matrix, can be determined by differentiating Eq. 5.7 with respect to  $\beta$  and setting the derivative equal to 0.

$$\hat{\beta} = (Z^T Z)^{-1} Z^T (Y - T|_{\beta=0}) \quad (5.8)$$

In this way,  $\beta$ , the heat flux matrix at the time step  $M$ , is determined. The equation provides an algorithm that is used in a sequential manner by increasing  $M$  by one for each time step. By repeating the optimization process, all components of the heat flux can be estimated.

Ansys is coupled with Matlab to solve the 3D inverse heat conduction problem as shown in Fig. 5.2. First of all, initial thermal states of all nodes are simulated by conducting a steady-state simulation in Ansys, since the plate may suffer from temperature differences due to local flow influence. Then Ansys is run to obtain the temperature response matrix on the rear surface for  $r$  future steps assuming all fluxes to be zero. Afterwards, unit heat flux ( $1 \text{ MW/m}^2$ ) is applied at one location and all other heat fluxes are assumed to be zero, to obtain the temperature response matrix for  $r$  future steps. The same procedure is repeated  $I$  (the

number of independent heat flux) times, thus generating  $I$  number of temperature response matrices. They are sent back to Matlab together with the zero heat flux response to compute the sensitivity matrix  $X$ . Together with measurement data, the heat flux matrix is estimated according to Eq. 5.8. Finally, the estimated heat flux matrix is fed into Ansys to perform a direct simulation for updating thermal states of all nodes. The whole procedure is iterated for the next time step until the end. The 3D inverse heat conduction model allowed obtaining the front surface temperature and the front surface heat flux at any given time step during the experiments, which are shown in the results and discussions section.

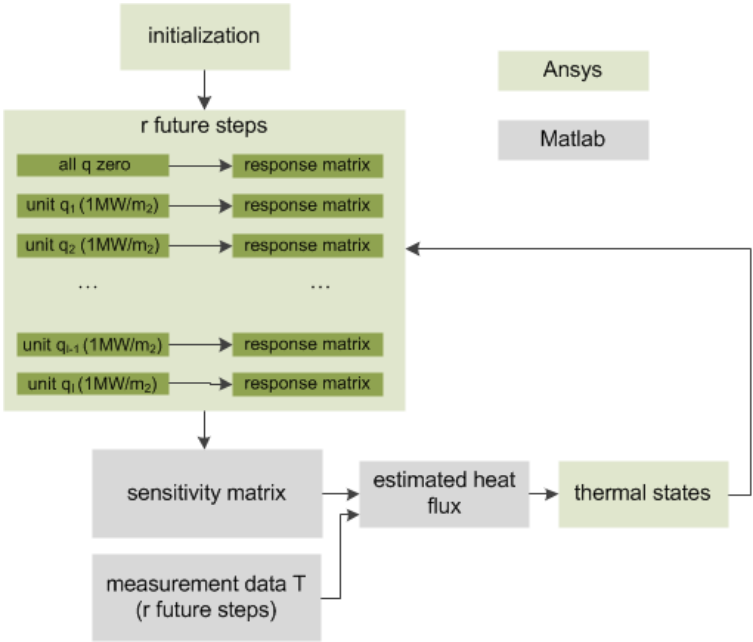


**Figure 5.2:** Flow chart of the 3D inverse heat conduction algorithm

## 5.4 Results and discussion

### 5.4.1 Heat transfer characteristics during spray wall impingement

The images recorded by the IR camera during the experiments were post-processed in Matlab according to Sec. 5.2. The injection duration was set to 100 ms and the injection frequency at 2 Hz. The associated gas flow condition was 400 °C and 100 kg/h. The x and z coordinates indicate the measurement locations with respect to the injector nozzle exit.

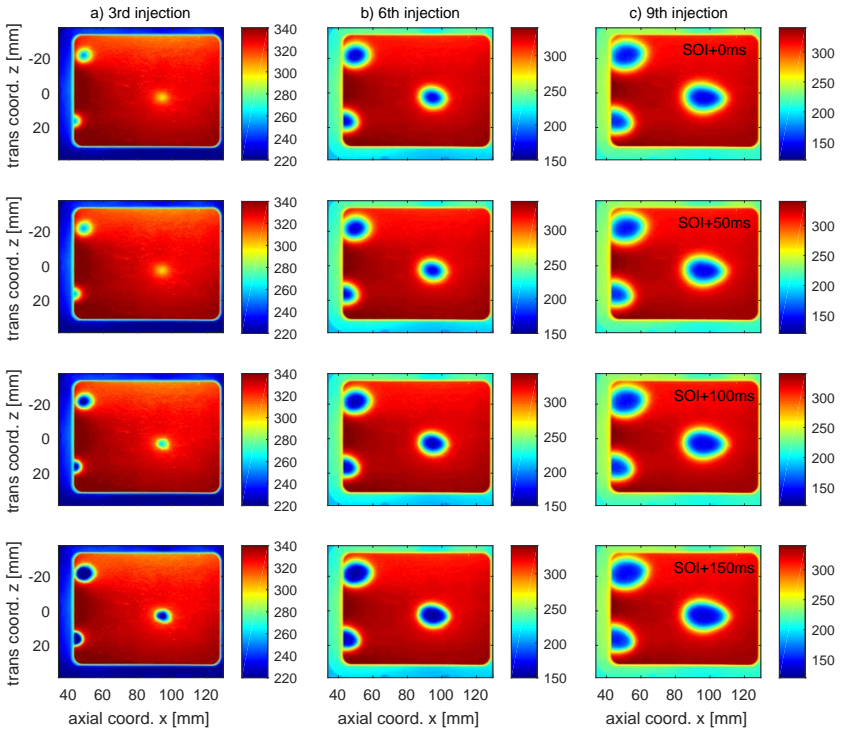


**Figure 5.3:** Spatial distribution of the measured rear surface temperature for a) the third injection [°C], b) the sixth injection [°C] and c) the ninth injection [°C] (gas flow: 400 °C, 100 kg/h, and injection parameters: 100 ms, 2 Hz).

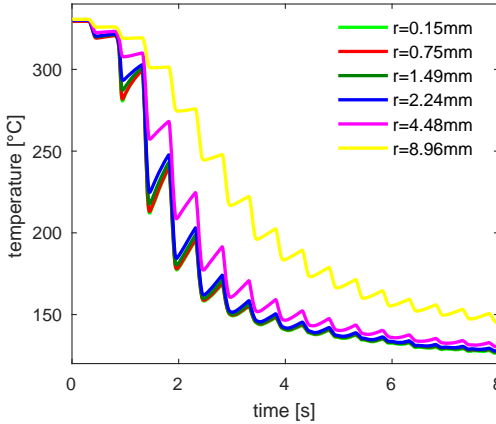


Fig. 5.3a shows the rear surface temperatures at different time instants after the electronic start of injection (SOI) for the third, Fig. 5.3b for the sixth, and Fig. 5.3c for the ninth injection. At these gas flow conditions and without UWS injection, the temperatures on the plate after achieving thermal equilibrium with the flow are around 345 °C in the mid-section of the upstream edge ( $x=45$  mm,  $z=0$  mm), and 330 °C in the mid-section of the downstream edge ( $x=127$  mm,  $z=0$  mm). In the lateral  $z$  direction, the temperature distribution is not entirely symmetric due to different materials of the channel walls. On the left side the wall is consisting of stainless steel, resulting in slightly higher heat losses to the ambient  $T(x=86$  mm,  $z=-31$  mm) = 310 °C, while on the right side  $T(x=86$  mm,  $z=31$  mm) = 335 °C. These values can also be retrieved from the upper diagram of Fig. 5.3a in the non-wetted areas of the plate.

The 3-hole injector produces three unique impingement footprints. Later in this section, they are referred to as the upstream, middle and downstream cone depending on the location in the axial flow direction. Clearly discernible is the individual development of the impingement regions, as the cone with the smallest distance from the plate (upstream cone) is the first to impinge and develops the associated footprint and the cone with the longest distance (downstream cone) is the last. As evidenced in the plot, the spray causes strong local cooling in the impingement regions, resulting in a temperature difference of about 120 °C to the non-impinged region after the third injection. With increasing number of injections, the cooled regions expand laterally and spread out, the most along the axial flow direction. After the ninth injection, the temperature difference between the impinged and non-impinged regions reaches up to 190 °C, while the temperature at the impinged regions approaches 140 °C.

Fig. 5.4 indicates the temporal evolution of the downstream cone impingement area temperature, averaged around the center over different radii. The effect of each injection is clearly visible. Following injection beginning, strong local cooling is evident. Between two injections, the plate is reheated by the gas flow, although weakly. The local cooling of

the first two injections is weak. From the third injection, the cooling effect ramps up. After several injections (approximately nine), the plate temperature has dropped substantially, reaching a quasi-steady state. As expected, averaging over a larger radius leads to strong attenuation of the cooling effect. The bigger the averaging radius is, the less the average temperature decreases. Averaging by 2.24 mm preserves the core characteristics well, therefore it is chosen as a reference.



**Figure 5.4:** Temporal evolution of temperature averaged around the downstream cone center ( $x=95$  mm,  $z=4$  mm) over different radii (gas flow:  $400$  °C,  $100$  kg/h, and injection parameters:  $100$  ms,  $2$  Hz)

Fig. 5.5 illustrates the temperature drop for each injection event along the downstream cone impingement centerline. In the impingement area center ( $x=95$  mm) the temperature difference is the highest, peaking up to  $90$  °C in the third injection. With increasing number of injections, the local temperature difference decreases gradually to  $5$  °C in the ninth injection. However, the temperature difference in the impingement periphery ( $x=110$  mm) reaches its maximum of  $50$  °C in the ninth injection. The cooling front on the plate originates from the center of impingement regions, and then propagates further outward, like a cooling ring. This is in good agreement with the detailed analysis for only one injection in Chap. 4. However, the downstream side gets cooled stronger than the upstream side from the fifth injection and on. The injected liquid forms

a liquid film on the plate, which is transported downstream by the injection momentum (and partly by the gas flow) as shown in Chap. 2. Here the plate temperature is higher than that of the already cooled down impingement region leading to evaporation of water. Nevertheless, the highest temperature difference, corresponding to the heat flux peak, is found around the spray cone center. Therefore, temperatures around the cone center are further analyzed.

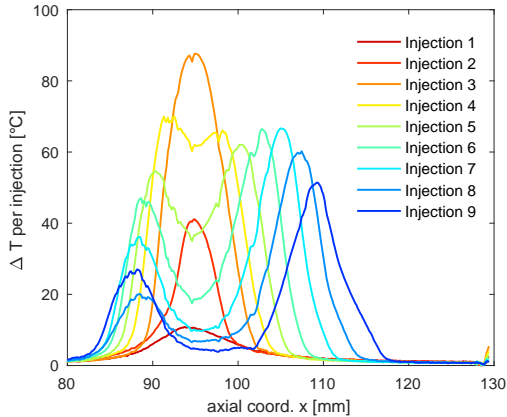


**Figure 5.5:** Temperature difference (per injection) profiles across the centerline of the downstream spray cone (gas flow: 400°C, 100kg/h, and injection parameters: 100ms, 2Hz).

Fig. 5.6 shows the temporal evolution of the average temperature around the spray cone center (radius=2.24 mm) and its (temporal) gradient. For the first injection, the plate temperature is the highest, 330 °C, as well as the temperature difference to the impinging spray (spray temperatures around 60 °C). The temperature gradient (in other words, the spray cooling flux), though, is quite small. Before the third injection, the local plate temperature drops to 300 °C. However, the gradient reaches a peak during this injection, nine-fold the first injection. Afterwards, the plate temperature as well as the gradient decreases.

The local plate temperature is decreasing while the temperature gradient (being proportional to the heat flux) firstly increases, then decreases. This can be associated with the boiling behavior of the UWS solution.

During the first injection, the plate temperature is around the Leidenfrost point, therefore the gradient is low. As temperature decreases further, the critical heat flux area is crossed, exhibiting the highest temperature gradient. Later in time, the plate temperature is low, being in the nucleate boiling regime, which is characterized by the low and diminishing temperature gradients. Due to the periodic operation of the injector, the gradient is oscillating with the injection profile, while following the boiling characteristics in general.

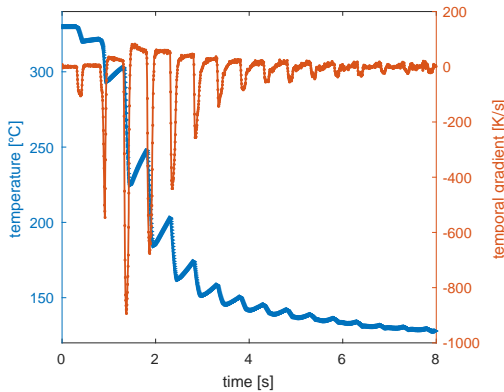


**Figure 5.6:** Evolution of temperature (averaged around the cone center for  $r=2.24$  mm) and its temporal gradient (gas flow:  $400^{\circ}\text{C}$ ,  $100$  kg/h, and injection parameters:  $100$  ms,  $2$  Hz).

## 5.4.2 Influence of the gas flow conditions and the injection duration on the heat transfer characteristics

The influence of the gas flow temperature is examined; setting the gas flow temperature to  $200$ ,  $300$ ,  $400$  and  $500^{\circ}\text{C}$  while keeping the gas flow rate constant at  $100$  kg/h. Higher gas flow temperature also means higher temperature of the spray-impinged plate since the plate is immersed in the channel flow and reaches the thermal steady-state before the injection starts. On the other hand, the influence of the gas temperature on the liquid spray temperature arriving at the plate is marginal. With increasing gas temperature, a large portion of the smallest droplets

evaporate before reaching the plate, while the larger droplets are heated but to a small extent. In Sec. 2.3.1 the influence of gas flow temperature on the evaporation of the spray as well as on the impinging mass flux was analyzed in detail.

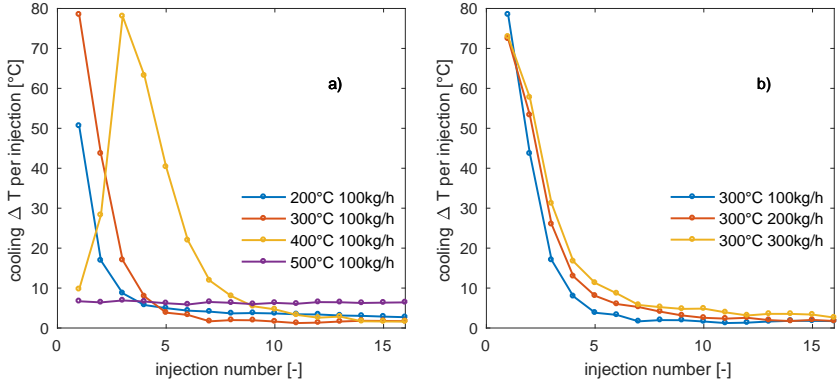


**Figure 5.7:** Temperature (averaged around the cone center over  $r=2.24$  mm) difference per injection for a) different gas flow temperatures and b) different gas flow rates (injection parameters: 100 ms, 2 Hz).

Fig. 5.7a displays the cooling phase temperature changes per injection. Again temperatures are averaged over  $r=2.24$  mm for the downstream spray cone. At the gas flow temperature of 500 °C, the spray cooling on the plate is weak for all 16 injections. There is a constant temperature drop of about 7 °C for each injection. Under this condition, the plate temperature is above Leidenfrost temperature, therefore less heat is transferred due to a lack of direct contact of the liquid and the hot surface. At gas flow temperature 400 °C, the plate has an initial temperature around the Leidenfrost point, which drops to the critical heat flux point and then follows the nucleate boiling behavior as shown in Fig. 5.6. At 300 °C gas flow temperature, the initial plate temperature is in the critical heat flux area. The injection cools the plate and nucleate boiling regime is entered. Interestingly, the temperature drop around the critical heat flux point is approximately 80 °C regardless whether the gas flow temperature is 300 °C or 400 °C (Fig. 5.7a). At the lowest gas flow temperature, 200 °C, the spray cooling effect on the plate peaks in the

first injection featuring a temperature drop of  $50\text{ }^{\circ}\text{C}$ , decreases substantially in the following injections, and finally stabilizes at less than  $5\text{ }^{\circ}\text{C}$  from the fifth injection onward. This again indicates that the plate temperature fundamentally determines the spray impingement heat transfer for such applications. This is also reflected in Fig. 5.7b). If the same gas flow temperature of  $300\text{ }^{\circ}\text{C}$  is kept but the gas flow rate is varied from  $100\text{ kg/h}$  to  $300\text{ kg/h}$ , the spray cooling effect on the plate follows a similar pattern as the nucleate boiling behavior.

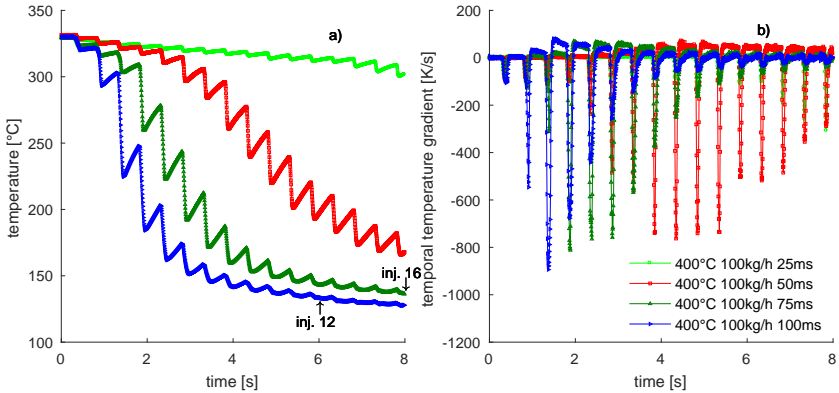


**Figure 5.8:** Evolution of a) temperature (averaged around the cone center for  $r=2.24\text{ mm}$ ) and b) its temporal gradient for different injection durations (gas flow:  $400\text{ }^{\circ}\text{C}$ ,  $100\text{ kg/h}$ , and injection frequency:  $2\text{ Hz}$ ).

Fig. 5.8 compares the downstream cone plate temperature at the impingement area and the corresponding temporal gradient evolutions for different injection durations ( $25\text{ ms}$ ,  $50\text{ ms}$ ,  $75\text{ ms}$  and  $100\text{ ms}$ ) under the gas flow condition of  $400\text{ }^{\circ}\text{C}$ ,  $100\text{ kg/h}$  (reference case analyzed in Sec. 5.4.1), in effect different amounts of injected UWS and thus differing liquid amount impinging per injection event. However, according to Spiteri [48], the impinging spray mass flux is constant and independent of the injection duration. Shorter injection durations result in slower plate cooling, clearly discernible from the  $25\text{ ms}$  and  $50\text{ ms}$  curve (Fig. 5.8a)). However, the plate temperature is cooled to a similar level for identical total injected mass, as can be seen by the comparison of the plate temperatures after the 16<sup>th</sup> injection of the  $75\text{ ms}$  case and the 12<sup>th</sup> injection

tion of the 100 ms case. Fig. 5.8b) shows that different injection duration cases lead to very similar phenomena differing only in the time pattern. All examined cases lead to similar magnitudes of critical heat flux (temperature gradient around  $-900$  K/s). The longer the injection duration is, the earlier the critical heat flux is reached. This time is inversely proportional to the injection duration, taking place in the third injection for the 100 ms case, fourth injection for the 75 ms case, ninth injection for the 50 ms case and 19<sup>th</sup> injection for the 25 ms case (not shown in Fig. 5.8 in order to have an appropriate resolution for the three former cases).

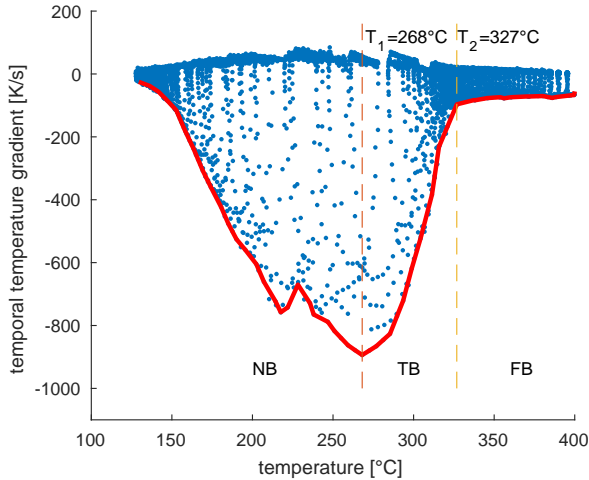


**Figure 5.9:** Temperature gradient as a function of temperature (averaged around the cone center for  $r=2.24$  mm) for different conditions investigated.

All temperature gradients, collected from all different conditions, are plotted over the plate temperature in Fig. 5.9. Intermediate gradients, due to the periodic operation of the injector, are plotted with blue points. The red curve connects the maximum temperature gradients reached for each plate temperature. All cases lead to almost identical temperature gradients for the same plate temperatures. In addition, the similarity to the Nukiyama's boiling curve for water [30] is evident. At high plate temperatures (above  $327^{\circ}\text{C}$ ), the temperature gradients are low. This

corresponds to an area around the Leidenfrost point. UWS single droplet evaporation experiments [4, 90] exhibit relatively long droplet life times in this area, almost independent of temperature. Between 327 °C and 268 °C, temperature gradients increase, as expected in the transition boiling regime. The critical heat flux (CHF) temperature for impinging SCR spray is estimated to be 268 °C. However, this analysis is based on the rear surface temperature. In the next section, numeric solving of the inverse heat conduction problem and related analysis deliver the front side plate CHF temperature. Below the CHF temperature, temperature gradients decrease as the nucleate boiling regime is entered.

### 5.4.3 Critical heat flux estimation

As mentioned before, the function specification method has been used for computing the front side temperatures based on the measured rear side temperatures by solving the 3D inverse heat conduction. Hereby, the reference case 400 °C, 100 kg/h with 100 ms injection duration has been analyzed to assess the difference between temperatures as well as to quantify the critical heat flux.

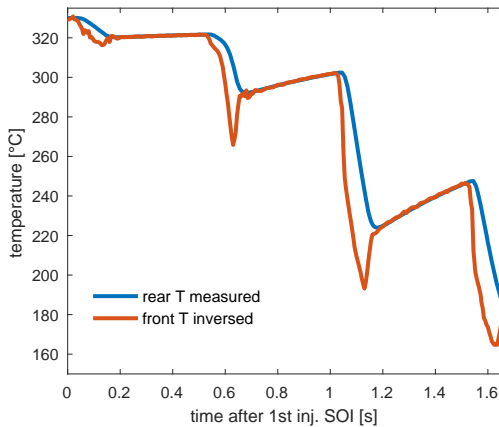


**Figure 5.10:** Temporal evolution of the measured rear surface and the computed front surface temperatures (averaged around the cone center for  $r=2.24$  mm) (gas flow: 400 °C, 100 kg/h, and injection parameters: 100 ms, 2 Hz).



Fig. 5.10 shows a comparison of the measured rear surface temperature and the computed front surface temperature for the first four injections. Directly after SOI the front surface temperature decreases sharply, while the rear surface decreases less and with a phase lag. During the entire injection the front surface has lower temperatures than the rear surface. After the end of each injection, the front and rear surface converge to similar values due to thermal conduction. The front surface temperature, however, behaves similarly to the rear surface temperature, low temperature drop in the first injection and maximum temperature drop in the third injection.

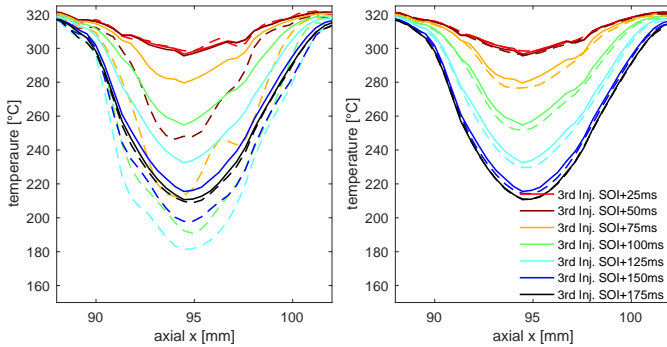


**Figure 5.11:** The 3rd injection temperature profiles at different times after SOI a) solid line: measured rear surface temperature, dashed line: computed front surface temperature; b) solid line: measured rear surface temperature, dashed line: computed rear surface temperature (gas flow: 400 °C, 100 kg/h, and injection parameters: 100 ms, 2 Hz).

Fig. 5.11 compares the plate temperature profiles across the downstream cone centerline, on rear and front surfaces. On the left side, the computed front surface temperature is compared to the measured rear surface temperature. In general, the rear surface temperature drop is damped in magnitude and lagged in time with respect to the front surface temperature. As also shown in Fig. 5.10, the deviation between the front and rear surface temperature only exists during the injection transient, from SOI+50 ms to SOI+150 ms. It peaks around 65 °C at SOI+100 ms, where the spray cooling heat flux peaks as well. Accounting for this deviation, the CHF temperature is around 203 °C from the

front surface temperature side, which then is very close to the literature value,  $200\text{ }^{\circ}\text{C}$  [4, 96]. On the right side, the measured and computed rear surface temperatures are compared. The computation of the rear surface temperatures is based on the front surface temperatures which in turn have been computed from the measured rear surface temperatures. The overall agreement is very good exhibiting differences of less than  $2\text{ }^{\circ}\text{C}$  for all locations and time steps.

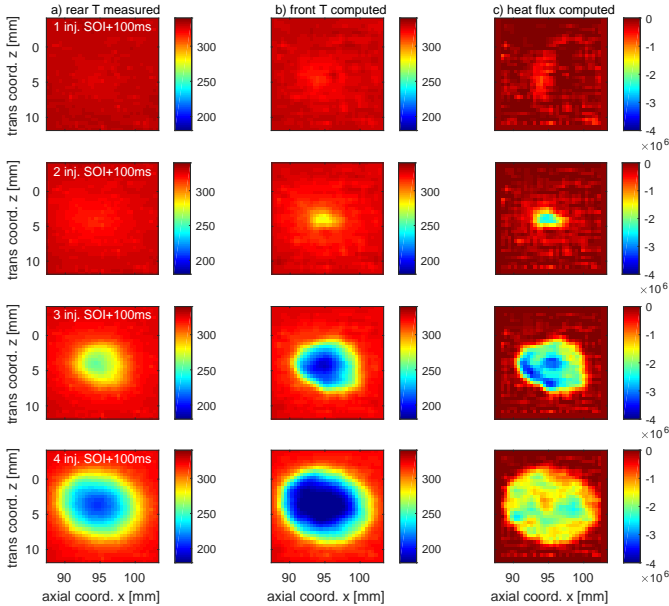


**Figure 5.12:** a) rear measured surface temperature, b) front computed surface temperature and c) computed spray heat flux at 100 ms after SOI for the first 4 injections (gas flow:  $400\text{ }^{\circ}\text{C}$ ,  $100\text{ kg/h}$ , and injection parameters:  $100\text{ ms}$ ,  $2\text{ Hz}$ ).

The measured rear surface temperature, the computed front surface temperature and the distribution of the heat flux at 100 ms after the electronic SOI for the first four injections are depicted in Fig. 5.12. Fig. 5.12a shows the measured rear surface temperature, Fig. 5.12b indicates the front surface temperature, computed as described above, while Fig. 5.12c displays the front surface heat flux. As already mentioned, the x and z coordinates indicate the measurement locations with respect to the

injector nozzle exit. The front surface temperature behaves similarly to the rear surface temperature, while it is much lower during the injection transient as described in Fig. 5.10 and Fig. 5.11. The cooling heat flux is quite low during the first injection, peaking around  $0.5 \text{ MW/m}^2$ , but increases during the second injection to around  $2.5 \text{ MW/m}^2$ . The highest values are reached during the third injection of around  $3.5 \text{ MW/m}^2$  as the critical heat flux regime is crossed. In the fourth injection the peak heat flux decreases to about  $2.5 \text{ MW/m}^2$ . The ratios among these heat fluxes are similar to the ratios of the temporal temperature gradients on the rear side of the impinged plate for the first four injections as shown in Fig. 5.8b.

Water spray cooling experiments on hot steel surfaces reported critical heat flux of  $1 \text{ MW/m}^2$  [70] and  $2 \text{ MW/m}^2$  [68]. It is possible that the low values in [70] are because of the strong averaging applied in the data analysis. According to Jia et al. [68], the critical heat flux increases with the increasing impinging mass flux, having a CHF value of  $2 \text{ MW/m}^2$  at  $1.2 \text{ kg/m}^2\text{s}$ . The impinging mass flux in the present study has been determined in Chap. 2 to be around  $3.3 \text{ kg/m}^2\text{s}$  in the impingement regions.

## 5.5 Summary

Heat transfer characteristics of urea-water-solution (UWS) spray impingement under various diesel exhaust flow conditions have been investigated. The spray has been generated by a 3-hole commercial pressure-driven injector operated at 2 Hz with a standard injection duration of 100 ms, resulting in an injection quantity of 0.2 g UWS per injection. The temperature distribution on the non-impinged, rear surface of a stainless steel plate has been measured by infrared thermography. The spray-impinged side surface temperature and heat flux distributions have been estimated by solving the 3D inverse heat conduction problem in the plate with the sequential function specification method. The main conclusions of the IR-temperature measurements on the rear side of the impinged plate can be summarized as follows:

1. Spray liquid boiling in the impingement regions leads to local cooling. The cooling depends on the instantaneous, local plate temperature. A cooling front starts from the center of the impingement region followed by annular propagation, more pronounced in the downstream direction.
2. At high plate temperatures ( $>327^{\circ}\text{C}$ ), each impingement event results in only minor temporal temperature gradients and low heat removal from the plate.
3. At intermediate plate temperatures ( $327^{\circ}\text{C} > T > 268^{\circ}\text{C}$ ), each impingement event leads to different temporal temperature gradients and heat removal, depending on the instantaneous local plate temperature. The temporal temperature gradient increases with decreasing plate temperature as long as the local plate temperature (rear surface) remains higher than  $268^{\circ}\text{C}$ .
4. Has the local plate been cooled below  $268^{\circ}\text{C}$ , temporal temperature gradients decrease with each consecutive impingement event.
5. The above phenomena can be associated with the boiling behavior of UWS; at rear surface plate temperatures  $>327^{\circ}\text{C}$  local boiling is in the film boiling regime, as temperatures decrease with each consecutive injection the transition regime is entered. At rear surface temperatures of  $268^{\circ}\text{C}$  the critical heat flux is reached. Lower plate temperatures lead to nucleate boiling.
6. Shorter injection durations, i.e. lower injected mass per injection, result in slower cooling of the plate. The local plate temperature, however, reaches similar values for identical total injected mass.
7. All measured variations (gas flow rates, gas flow temperatures and injection durations) have shown similar temperature gradients for identical plate temperatures.
8. Highest temporal temperature gradients ( $\sim 900\text{ K/s}$ ) have been measured at a rear plate surface temperature of  $268^{\circ}\text{C}$ , for all investigated injection durations, gas flows and gas temperatures.

The numerical solution of the inverse heat conduction leads to the corresponding temperature and heat flux on the impinged plate surface:

1. As expected, the front surface temperature decreases more sharply than the rear surface temperature during the impingement event.
2. The critical heat flux temperature (of the impinged side) has been computed at  $203\text{ }^{\circ}\text{C}$  and the critical heat flux at  $3.5\text{ MW/m}^2$ . The former is in good agreement with the boiling behavior of single UWS droplet evaporation measurements while the latter lies in the reported trends for industrial nozzles.



# 6 Conclusions and outlook

## 6.1 Summary

### Spray Impingement Phenomenology

Optical high speed imaging experiments have been performed with the 3-hole injector in order to identify the involved phenomena in detail. The spray impingement leads to formation of three individual liquid films on the corresponding impingement areas due to strong local cooling. During each injection, the liquid film area increases, reaching a maximum shortly after the end of the respective injection. Thereafter, the liquid film retracts, reaching a minimum before the next injection starts. In general, the liquid film areas spread out from injection to injection, leading to a merging of the three films. Afterwards, a significant amount of the liquid film is transported downstream mainly by the injection momentum and forms a liquid accumulation site. After the injection termination, urea starts to crystallize from the urea-enriched liquid film around the spray-impinged area. This is mainly due to evaporation of water leading to increasing urea concentrations on the remaining liquid films. After the formation period the urea crystals melt. The urea crystallization rate is almost 2 times the urea melting rate. The crystallization rate is mainly driven by the process kinetics. However, the melting rate is strongly dependent on the heat transfer rate. Following melting, the urea-enriched film starts evaporating from the upstream side. The thin film in the impinged region is completely evaporated, and no deposit remains. However, solid deposits form at the liquid accumulation site where nucleate boiling is evidenced. Under all tested conditions, permanent deposit have been observed in the liquid accumulation site.

Nuclear magnetic resonance spectroscopy results reveal that the solid deposits are composed of 73.0 % cyanuric acid, 13.8 % biuret, 11.8 % ammelide and 1.5 % ammeline. The main component, cyanuric acid, starts to decompose at 320 °C and is limited by the reaction kinetics [10]. The relative stability of solid deposits suggests that, once they are formed, it is difficult to remove them. The close relationship between liquid film formation and deposit formation indicates that measures should be taken to avoid liquid film formation. Maintaining impinged wall temperatures above the non-wetting threshold would be a promising solution.

### **Quantification of the spray impinging fraction and its dependencies**

The impinging mass flux distributions of the 3-Hole pressure-driven injector have been quantified by a mechanical patternator. There are three distinct impingement regions, each corresponding to one hole of the used injector. The maximum local impingement flux is 5.89 kg/m<sup>2</sup>s at stagnant condition, while it drops down to 3.31 kg/m<sup>2</sup>s at the flow condition of 300 °C, 200 kg/h. In total, still a significant part, 35.6 % of the total injected fluid, impinges on the opposed wall under the exhaust flow condition of 300 °C, 200 kg/h despite of entrainment and evaporation. Furthermore, the impinging mass is modelled as a function of gas flow temperature and momentum, which allows the prediction of the impinging mass quantity under various gas flow conditions. The influence of the gas flow momentum on impinging mass (injected mass minus the entrained mass under non-evaporating conditions) was described by a logarithmic function with good accuracy. The influence of the gas flow temperature on the impinging mass (injected mass minus the evaporated mass) was approximated by a square root function of the temperature difference between the gas flow temperature and the liquid saturation temperature.

In addition, the influence of entrainment and evaporation on the impinging droplet size distribution has been analyzed by combining patternator and PDA results. The impingement mass fraction is gradually increasing with increasing droplet diameter up to 90 µm, whereas almost



all larger droplets reach the opposed wall. Droplets below  $20\ \mu\text{m}$  are almost completely entrained and/or evaporated by the exhaust gas flow, whereas 40 % of mass reduction is evidenced for droplets between  $73\ \mu\text{m}$  to  $90\ \mu\text{m}$ . It is concluded that finer sprays after primary breakup will significantly reduce the wall impingement.

### **Kinetic properties of the spray droplets prior to impingement**

The kinetic properties, i.e. droplet sizes and velocities, of impinging droplets have been assessed by Phase Doppler Anemometry. Four commercially available SCR injectors, three pressure-driven and one air-assisted, have been compared. In general, the spray impingement for pressure-driven injectors is more significant given the low levels of entrainment and evaporation and thus the higher impinging mass. In contrast, the spray of the air-assisted injector is significantly more susceptible to the exhaust flow, leading to lower impingement levels.

Prior to wall impingement, Sauter mean diameters of the droplets from the pressure-driven injectors are between  $60\text{--}80\ \mu\text{m}$ , while that of the air-assisted is  $20\ \mu\text{m}$ . Among the pressure-driven injectors, the 3-hole injector is characterized by the largest droplet sizes ( $\text{SMD}=81.4\ \mu\text{m}$ ), while the two 6-hole injectors have similar average droplet sizes ( $\text{SMD}=68.7$  and  $64.5\ \mu\text{m}$ ). In general, the main part of the spray mass flow is contained in larger droplets in the vicinity of the spray cone center. Further downstream, the droplet sizes containing the main part of the spray mass flow are significantly smaller. However, the air-assisted injector spray is associated with smaller droplets in all investigated locations.

Prior to wall impingement, higher impinging velocities (vertical component, normal to the wall) are associated with larger droplets for pressure-driven sprays, while smaller droplets are strongly decelerated by aerodynamic drag during the movement towards the wall. Velocities of the droplets from the air-assisted injector behave similar to the smallest droplets of the pressure-driven injectors. Therefore, larger droplets have higher Reynolds number and Weber number prior to impingement. For the 3-hole injector, over 95 % of droplets possess Mundo numbers  $K$  (a synthetic non-dimensional number of  $\text{Re}$  and  $\text{We}$ ) lower than 150 regard-

less of exhaust flow conditions. According to the spray/wall interaction regime map [29], for droplets with  $K$  smaller than 150 the principal interaction behavior is deposition as long as the temperature is below the critical wall temperature. Should the temperature be above the critical wall temperature, the interaction regimes change to rebound and thermal breakup. Droplets with Mundo number larger than 150 (generally larger than  $100\ \mu\text{m}$ ) undergo splash below the critical temperature. Apparently, deposition is the most undesirable mode for SCR applications due to the loss of reducing agent and the resulting solid deposit formation.

In summary, the air-assisted injector produces a fine spray, which favors the uniform mixing with the exhaust flow and the mitigation of deposit formation. For pressure-driven injectors, avoiding deposition is definitely essential. This could be achieved by maintaining the wall temperature always above the critical temperature during the spray impingement or increasing the injection pressure as the Mundo number has a stronger proportionality to the droplet velocity than to the droplet size. Nevertheless, other system requirements and the injector location in respect of further parts like exhaust pipe wall, mixer and catalysts are decisive for the selection of the most suitable injector.

### **Heat transfer during a single spray impingement**

The temperature distributions on the non-impinged rear surface of a stainless steel plate have been measured by infrared thermography under various exhaust flow conditions. The measured rear side temperatures have been used for assessing spray cooling heat fluxes by solving the 1D inverse heat conduction problem. The spray impingement leads to a rapid temperature drop on the impinged plate. The cooling effect remains relatively concentrated to the spray-impinged areas while temperatures of the non-impinged areas stay unaffected. Thus, the spray cooling effect on the exhaust pipe wall is local and the lateral heat conduction plays a minor role on the (millisecond) timescale of the entire injection duration. The temperature drop on the  $0.3\ \text{mm}$  plate is up to  $150\ ^\circ\text{C}$  for a  $60\ \text{ms}$  single injection at the gas flow condition of  $300\ ^\circ\text{C}$ ,

200 kg/h. This results in transient local heat fluxes of several megawatts per square meter during the injection. The strongest cooling is in the center of the impinging area and occurs right after the first impingement. Thereafter, the strong and rapid temperature drop in the impingement center leads to a reduction of the heat flux and area of the strongest heat transferred moves annularly to the periphery of the impinged area.

The spray cooling effect decreases with increasing exhaust gas flow rate. Thus, the initial temperature gradient is less steep for higher gas flow rates. However, the influence of the gas flow rate is less pronounced in the spray core impingement area. For a single injection at 300 °C, increasing the gas flow rate from 200 kg/h to 300 kg/h results in 30 % lower heat transferred from the plate to the spray as a result of enhanced droplet entrainment in the gas flow prior to the impingement. Changes in gas flow temperature influence the spray/wall interaction regimes mainly by differing the wall temperatures. As summarized in the droplet kinetics section, most droplets have relatively small Mundo numbers for the 3-hole injector. Therefore, the principal spray/wall interaction behavior is deposition below the critical wall temperature; rebound and thermal breakup should the wall temperature be above the critical wall temperature. At 200 kg/h, increasing the gas flow temperature from 300 °C to 400 °C leads to a substantial reduction of heat fluxes, and in total a 50 % decrease of the transferred heat as the critical temperature is crossed. The shorter contact times in the rebound and thermal breakup regimes result in decreased spray/wall heat transfer. Heating up the exhaust pipe is a solution to limit the cooling on the exhaust pipe wall, thus avoiding deposit formation.

### **Heat transfer characteristics of sequential urea-water spray impingement**

Heat transfer characteristics of urea-water solution (UWS) spray impingement under various exhaust flow conditions have been investigated with the 3-hole injector operated at 2 Hz. The standard injection duration was set at 100 ms. The temporal and spatial temperature distribution on the non-impinged rear surface of a stainless steel plate has been

measured by infrared thermography. The spray impinged side surface temperature and heat flux distributions have been computed by solving the 3D inverse heat conduction in the plate with the sequential function specification method.

Urea-water spray impingement leads to local cooling in the impingement regions, which is in good agreement with the previous single water spray impingement results. The cooling front starts from the center of the impingement region followed by annular propagation, more pronounced in the downstream direction. The spray cooling magnitude heavily depends on the instantaneous local plate temperature. At high plate temperatures ( $>327^{\circ}\text{C}$ ), each impingement event results in only minor negative temporal temperature gradients and thus low amount of heat removal from the plate. At intermediate plate temperatures ( $327^{\circ}\text{C} > T > 268^{\circ}\text{C}$ ), each impingement event leads to increasing temporal temperature gradients and heat removal, depending on the instantaneous local plate temperature. The temporal temperature gradient increases in magnitude with decreasing plate temperature as long as the local plate temperature (rear surface) remains higher than  $268^{\circ}\text{C}$ . Has the local plate been cooled below  $268^{\circ}\text{C}$ , temporal temperature gradients decrease in magnitude with each consecutive impingement event. The above phenomena can be associated with the boiling behavior of the urea-water solution; at rear surface plate temperatures  $>327^{\circ}\text{C}$  local boiling is in the film boiling regime with Leidenfrost phenomena. As temperatures decrease with each consecutive injection the transition regime is entered. At rear surface temperatures of  $268^{\circ}\text{C}$  the critical heat flux is reached. Lower plate temperatures lead to nucleate boiling.

Shorter injection durations, i.e. lower injected mass per injection, result in slower cooling of the plate. The local plate temperature, however, reaches similar values for identical cumulative injected mass. All measured variations (gas flow rates, gas flow temperatures and injection durations) have shown similar temperature gradients for identical plate temperatures. The highest temporal temperature gradients (around  $-900\text{K/s}$ ) have been found at a rear plate surface temperature of  $268^{\circ}\text{C}$ .

The numerical solution of the inverse heat conduction led to the corresponding temperature and heat flux on the impinged front plate surface. In general, the front surface temperature behaves similar to the rear surface temperature. They only differ during the impingement transient. The front surface has lower temperatures than the rear surface, while the front surface temperature decreases more sharply in time. The critical heat flux temperature (of the impinged side) is estimated at 203 °C and the critical heat flux at 3.5 MW/m<sup>2</sup>. The former is in good agreement with the boiling behavior of single UWS droplet evaporation measurements, while the latter lies in the reported trends for industrial nozzles.

In order to keep the impinged wall temperatures at high levels and avoid liquid film formation, efforts should concentrate on restraining the phenomena in the film boiling regime, thus avoiding the transition and nucleate boiling regimes. In real vehicle applications, this could be achieved by avoiding impingement on low temperature duct walls, i.e. by designs where impingement occurs mainly on devices positioned in the exhaust flow and not on the boundaries to the ambient atmosphere. In addition, active heating of such devices will significantly improve the situation and the system performances.

## 6.2 Conclusions and outlook

Pressure-driven injector spray impingement on the opposed wall is unavoidable under current configurations. The spray impingement leads to significant local cooling of the impinged plate and subsequent liquid film formation. As liquid accumulation areas form and spread, the formation of solid deposits, mainly composed of cyanuric acid, is unavoidable. All experiments performed in the controlled conditions of the channel for the present work led to solid deposit formation at the liquid accumulation sites. Once solid deposits are formed, it is difficult to remove them under typical exhaust flow conditions given the cyanuric acid decomposition temperature of 320 °C or higher.

According to the analysis in the present work, pressure-driven injectors, as used in current SCR systems, with injection pressures of 9 bar produce relative large droplets with moderate velocities which are quite inert to the exhaust flow. A major part of the spray droplets, consisting mainly of the larger droplets, impinges on the opposed wall regardless of exhaust flow conditions. From this perspective, it would be better to produce a finer spray to avoid spray wall impingement, either by using air-assisted injectors or by increasing the injection pressure. The impinging droplets in general possess relatively small Mundo numbers. Therefore, the principal spray/wall interaction regime is deposition at low wall temperatures, and rebound and thermal breakup above the critical wall temperature. Maintaining wall temperatures above the critical threshold through active heating, like electric resistance heating, which alter the spray/wall interaction regime, would be a promising solution to reduce liquid film formation tendencies.

The spray cooling magnitude on the opposed wall is heavily dependent on the instantaneous wall temperature. At high plate temperatures around the Leidenfrost point, each impingement event results in only low amount of heat removal from the opposed wall. At intermediate plate temperatures (transition boiling), each impingement event leads to significant heat removal, especially reaching the maximum ( $\text{MW/m}^2$ ) at the critical heat flux point. Has the local plate been cooled below the

critical heat flux temperature, heat removed decreases in magnitude with decreasing wall temperature. The impinged plate temperature could hardly be maintained as soon as the transition boiling regime is entered. To avoid liquid film formation, ultimately suppressing deposit formation, the impinged wall temperature should be kept in the film boiling regime through active heating. However, more active heat transfer surfaces should be added in order to deliver more heat to facilitate water evaporation and thermal decomposition of the urea-water solution.

Future works to improve the system performance could be conducted in the following directions. First of all, improving the feasibility of air-assisted injection on board will reduce the wall impingement; however efficient production of the compressed air will still remain a big challenge. Concerning pressure-driven injectors, increasing the injection pressure would result in a finer spray. However, faster droplets are more prone to impinge. Therefore, it is important to find the optimal injection pressure, which allows either complete entrainment and evaporation before impingement or high Mundo numbers undergoing splash mode below the critical wall temperature. Decreasing the nozzle diameter is also an option to produce a finer spray, however at the expenses of higher manufacturing precision. Moreover, incorporating heating devices in the exhaust pipe, like electric resistance heating or microwave heating, would also be a viable solution to shift the spray/wall impingement regime to rebound and thermal breakup thus eliminating the heat extracted from the impinged walls.

The method used in this study, infrared thermography together with 3D inverse heat conduction solved by sequential function specification method, would be an interesting way to estimate spatially-resolved transient spray cooling heat flux distributions. However, certain studies have to be made to speed up the 3D inverse heat conduction.





# List of Figures

1.1	Schematic diagram of a typical SCR system. . . . .	2
1.2	Typical boiling curve for water at 1 atm: surface heat flux as a function of excess temperature [30]. . . . .	5
1.3	Evaporation characteristics of 30wt % urea-water droplets ( $d=2.67$ mm) on a heated surface [4]. . . . .	7
1.4	Illustrations of two patterns in the evaporation process [4].	7
1.5	Water evaporation time calculated as a function of the initial drop diameter $D_0$ for (a) several temperatures $T_a$ in quiescent air and (b) several relative drop velocities in hot air of $250$ °C [6]. . . . .	9
1.6	Spray/wall interaction regime map according to [29]. . . .	13
2.1	Schematic diagram of the flow lab with the optical film visualization setup . . . . .	24
2.2	Image processing for extracting the liquid film area . . . .	25
2.3	Schematic drawing of the patternator integrated in the flow channel . . . . .	26
2.4	Mass flux distribution with a resolution of $2$ mm $\times$ $2$ mm on the plane $79$ mm apart from the injector nozzle exit at ambient conditions ( $20$ °C, $0$ kg/h). . . . .	30
2.5	Mass flux distribution with a resolution of $2$ mm $\times$ $2$ mm on the plane $79$ mm apart from the injector nozzle exit at the flow condition of $300$ °C, $200$ kg/h. . . . .	31
2.6	Relative frequency and cumulative distribution of mass flux measurements at ambient conditions and at the flow condition of $300$ °C $200$ kg/h. . . . .	32

2.7	Droplet mass distributions at ambient conditions and at the flow condition of 300 °C 200 kg/h. . . . .	33
2.8	Entrainment as a function of momentum. . . . .	34
2.9	Evaporation as a function of temperature. . . . .	35
2.10	First stage of impingement (flow conditions: 300 °C, 100 kg/h, injection 1 Hz of 120 ms for 150 s). . . . .	36
2.11	Initial liquid film area evolution before liquid film merging a) 300 °C, 100 kg/h, 120 ms of 1 Hz b) 300 °C, 100 kg/h, 60 ms of 1 Hz. . . . .	37
2.12	Liquid film area expansion and retraction a) 300 °C, 100 kg/h, 120 ms of 1 Hz b) 300 °C, 100 kg/h, 60 ms of 1 Hz. . . . .	37
2.13	Solid urea crystallizes during the injection interval at a later stage (flow conditions: 300 °C, 100 kg/h, injection 1 Hz of 120 ms for 150 s). . . . .	39
2.14	After the injector closes permanently, urea firstly crystallizes and then melts, followed by the liquid film evaporation (flow conditions: 300 °C, 100 kg/h, injection 1 Hz of 120 ms for 150 s). . . . .	40
2.15	Urea crystallization and urea melting area evolution after the end of injection. . . . .	40
2.16	Urea enriched film starts evaporating from the upstream side, and white deposits form in the downstream side. . . . .	41
2.17	Deposit location and quantity for different injection durations at the flow condition of 300 °C 200 kg/h. . . . .	41
2.18	<sup>13</sup> C NMR spectra of a stock solution (1.3 wt/wt-%) of solid deposits in 1.5 M NaOD/D <sub>2</sub> O of a) 'as is' and after addition of small quantities of b) ammelide, c) ammeline and d) biuret. . . . .	43
2.19	<sup>13</sup> C NMR spectra of a stock solution (1.3 wt/wt-%) of solid deposits in 1.5 M NaOD/D <sub>2</sub> O of a) 'as is' and after addition of small quantities of b) urea, c) triuret and d) melamine. . . . .	44

3.1	Stereo-microscopic photographs of the nozzle tip configuration of the four commercial SCR injectors investigated.	50
3.2	Schematic diagram of shadow imaging setup. . . . .	51
3.3	Setup to characterize the plate emissivity with lid removed.	51
3.4	Shadow imaging contours at different flow conditions for the four commercial SCR injectors (gas flow conditions: 300 °C, red: 100 kg/h, green: 200 kg/h, blue: 300 kg/h) . .	54
3.5	Droplet size distribution and droplet volume distribution of the injector A-A (air-assisted) exhaust gas flow conditions: 300 °C, 100 kg/h . . . . .	55
3.6	Droplet size distribution and droplet volume distribution of the injector P1-6H (6-hole pressure-driven) exhaust gas flow conditions: 300 °C, 100 kg/h. . . . .	56
3.7	Droplet size distribution and droplet volume distribution of the injector P-3H (3-hole pressure-driven) exhaust gas flow conditions: 300 °C, 100 kg/h. . . . .	56
3.8	Droplet size distribution and droplet volume distribution of the injector P2-6H (6-hole pressure-driven) 300 °C, 100 kg/h.	57
3.9	a) Mean downward velocities and b) mean axial velocities for the case of 300 °C, 300 kg/h at different axial locations for A-A (air-assisted) for different droplet size classes . . .	58
3.10	a) Mean downward velocities and b) mean axial velocities for the case of 300 °C, 300 kg/h at different axial locations for P1-6H (6-hole pressure-driven) for different droplet size classes. . . . .	58
3.11	a) Mean downward velocities and b) mean axial velocities for the case of 300 °C, 300 kg/h at different axial locations for P-3H (3-hole pressure-driven) for different droplet size classes. . . . .	59
3.12	a) Mean downward velocities and b) mean axial velocities for the case of 300 °C, 300 kg/h at different axial locations for P2-6H (6-hole pressure-driven) for different droplet size classes. . . . .	59

3.13	Droplet volume flow rate for the case of 300 °C, 300 kg/h at different axial locations for the A-A (air-assisted) injector.	60
3.14	Droplet volume flow rate for the case of 300 °C, 300 kg/h at different transverse locations for P1-6H (6-hole pressure-driven) injector. . . . .	61
3.15	Droplet volume flow rate for the case of 300 °C, 300 kg/h at different axial locations for P2-6H (6-hole pressure-driven) injector. . . . .	61
3.16	Droplet volume flow rate for the case of 300 °C, 300 kg/h at different axial locations for P-3H (3-hole pressure-driven) injector. . . . .	62
4.1	Schematic diagram of the flow lab . . . . .	69
4.2	Infrared thermography camera calibration curve . . . . .	70
4.3	Water emissivity as a function of the wavelength varying with the water film thickness [91]. . . . .	70
4.4	Experimental setup of infrared thermography in the flow channel. . . . .	71
4.5	Setup to characterize the plate emissivity with the lid removed. . . . .	72
4.6	Schematic illustration of 1D inverse heat conduction problem solved with finite element scheme [94]. . . . .	75
4.7	Spatial distribution of a) the measured rear surface temperature [°C], b) the calculated front surface temperature [°C] and c) the calculated front surface heat flux [W/m <sup>2</sup> ] (flow conditions: 300 °C, 200 kg/h). . . . .	77
4.8	Spatial distribution of the front surface heat flux [W/m <sup>2</sup> ] a) 8 ms after SOI b) 22 ms after SOI (flow conditions: 300 °C, 100 kg/h). . . . .	78
4.9	a) Plate front surface temperature and b) plate rear surface temperature profiles across the centerline (z = 2.3 mm) of the downstream spray cone at different times after the electronic SOI (flow conditions: 300 °C, 200 kg/h). . . . .	79

4.10	Temperature profiles across the centerline of each spray cone on the front surface at different times after the electronic SOI a) Upstream cone ( $z = 15.7$ mm), b) middle cone ( $z = -20.6$ mm) and c) downstream cone ( $z = 2.3$ mm) (flow conditions: $300$ °C, $200$ kg/h). . . . .	79
4.11	Temperatures averaged over different sizes of area around the downstream spray cone center for different flow conditions with constant $T$ and different $\dot{m}$ a) $r = 2.7$ mm, b) $r = 5.4$ mm. . . . .	81
4.12	Front surface heat flux averaged over different sizes of area around the downstream spray cone center for different flow conditions with constant $T$ and different $\dot{m}$ a) $r = 2.7$ mm, b) $r = 5.4$ mm. . . . .	81
4.13	Front surface heat flux averaged over different sizes of area around the downstream spray cone center for different flow conditions with constant $\dot{m}$ and different $T$ a) $r = 2.7$ mm, b) $r = 5.4$ mm. . . . .	82
4.14	Spatial distribution of heat exchanged during one injection event a) $300$ °C, $200$ kg/h, b) $300$ °C, $300$ kg/h . . . .	82
4.15	Spatial distribution of heat exchanged during one injection event a) $300$ °C, $200$ kg/h, b) $400$ °C, $200$ kg/h . . . .	83
4.16	Mundo number $K$ estimated from PDA measurements at different flow conditions along the downstream cone centerline at $18$ mm above the bottom of the channel. . . . .	84
4.17	Heat extracted by the spray cone area of different sizes at various gas flow conditions. . . . .	85
5.1	Experimental setup of infrared thermography in the flow channel . . . . .	94
5.2	Flow chart of the 3D inverse heat conduction algorithm . . . . .	97
5.3	Spatial distribution of the measured rear surface temperature for a) the third injection [°C], b) the sixth injection [°C] and c) the ninth injection [°C] (gas flow: $400$ °C, $100$ kg/h, and injection parameters: $100$ ms, $2$ Hz). . . . .	98

5.4	Temporal evolution of temperature averaged around the downstream cone center ( $x=95$ mm, $z=4$ mm) over different radii (gas flow: $400$ °C, $100$ kg/h, and injection parameters: $100$ ms, $2$ Hz) . . . . .	100
5.5	Temperature difference (per injection) profiles across the centerline of the downstream spray cone (gas flow: $400$ °C, $100$ kg/h, and injection parameters: $100$ ms, $2$ Hz). . . . .	101
5.6	Evolution of temperature (averaged around the cone center for $r=2.24$ mm) and its temporal gradient (gas flow: $400$ °C, $100$ kg/h, and injection parameters: $100$ ms, $2$ Hz). . . . .	102
5.7	Temperature (averaged around the cone center over $r=2.24$ mm) difference per injection for a) different gas flow temperatures and b) different gas flow rates (injection parameters: $100$ ms, $2$ Hz). . . . .	103
5.8	Evolution of a) temperature (averaged around the cone center for $r=2.24$ mm) and b) its temporal gradient for different injection durations (gas flow: $400$ °C, $100$ kg/h, and injection frequency: $2$ Hz). . . . .	104
5.9	Temperature gradient as a function of temperature (averaged around the cone center for $r=2.24$ mm) for different conditions investigated. . . . .	105
5.10	Temporal evolution of the measured rear surface and the computed front surface temperatures (averaged around the cone center for $r=2.24$ mm) (gas flow: $400$ °C, $100$ kg/h, and injection parameters: $100$ ms, $2$ Hz). . . . .	106
5.11	The 3rd injection temperature profiles at different times after SOI a) solid line: measured rear surface temperature, dashed line: computed front surface temperature; b) solid line: measured rear surface temperature, dashed line: computed rear surface temperature (gas flow: $400$ °C, $100$ kg/h, and injection parameters: $100$ ms, $2$ Hz). . . . .	107

5.12 a) rear measured surface temperature, b) front computed surface temperature and c) computed spray heat flux at 100 ms after SOI for the first 4 injections (gas flow: 400 °C, 100 kg/h, and injection parameters: 100 ms, 2 Hz). . . . . 108





# List of Tables

2.1	Gas flow conditions during the patternator measurements	27
2.2	Molecular formulae and weights, $^{13}\text{C}$ NMR chemical shifts and no. of carbons contributing to signal intensities of all chemical species possibly present in solid deposit samples	28
2.3	Area occupied by different mass fraction at ambient conditions and at 300 °C, 200 kg/h. . . . .	30
2.4	Estimated film thickness before liquid film merging and the comparison to numerical simulation [45]. . . . .	38
2.5	Sample compositions determined by quantitative evaluation of $^{13}\text{C}$ NMR data of sample under the condition of 300 °C, 100 kg/h 120 ms 'as is' and after addition of small aliquots of reference material. . . . .	44
3.1	Characteristics of the four commercial SCR injectors . . .	49
3.2	PDA sending optics and receiving optics settings . . . . .	52
3.3	Experimental flow conditions . . . . .	52
3.4	Summary of droplet size distributions . . . . .	57



# Bibliography

- [1] M. Koebel, M. Elsener, and M. Kleemann, "Urea-SCR: a promising technique to reduce NO<sub>x</sub> emissions from automotive diesel engines," *Catalysis Today*, vol. 59, no. 3, pp. 335–345, 2000.
- [2] S. D. Yim, S. J. Kim, J. H. Baik, I. S. Nam, Y. S. Mok, J. H. Lee, B. K. Cho, and S. H. Oh, "Decomposition of urea into NH<sub>3</sub> for the SCR process," *Industrial and Engineering Chemistry Research*, vol. 43, no. 16, pp. 4856–4863, 2004.
- [3] J. Y. Kim, S.-h. Ryu, and J.-s. Ha, "Numerical prediction on the characteristics of spray-induced mixing and thermal decomposition of urea solution in SCR systems," in *Proceedings of the 2004 Fall Technical Conference of the ASME Internal Combustion Engine Division of ICEF04*, 2004.
- [4] S. Musa, M. Saito, T. Furuhashi, and M. Arai, "Evaporation characteristics of a single aqueous urea solution droplet," *ICLASS-2006, Kyoto, Paper ID ICLASS06-195*, vol. 2, no. 1, 2006.
- [5] T. J. Wang, S. W. Baek, S. Y. Lee, D. H. Kang, and G. K. Yeo, "Experimental investigation on evaporation of urea-water-solution droplet for SCR applications," *AIChE Journal*, vol. 55, no. 12, pp. 3267–3276, 2009.
- [6] S. Grout, J. B. Blaisot, K. Pajot, and G. Osbat, "Experimental investigation on the injection of an urea-water solution in hot air stream for the SCR application: Evaporation and spray/wall interaction," *Fuel*, vol. 106, pp. 166–177, 2013.

- [7] A. Spiteri, P. Dimopoulos Eggenschwiler, Y. Liao, G. Wigley, K. A. Michalow-Mauke, M. Elsener, O. Kröcher, and K. Boulouchos, “Comparative analysis on the performance of pressure and air-assisted urea injection for selective catalytic reduction of NO<sub>x</sub>,” *Fuel*, vol. 161, pp. 269–277, 2015.
- [8] Z. Li, J. Deng, L. Li, L. Cao, and Z. Wu, “A study on the factors affecting heated wall impinging characteristics of scr spray,” *SAE Technical Paper 2011-01-1311*, 2011.
- [9] X. Shi, J. Deng, Z. Wu, and L. Li, “Effect of injection parameters on spray characteristics of urea-SCR system,” *SAE International Journal of Engines*, vol. 6, no. 2, pp. 873–881, 2013.
- [10] A. M. Bernhard, D. Peitz, M. Elsener, A. Wokaun, and O. Kröcher, “Hydrolysis and thermolysis of urea and its decomposition byproducts biuret, cyanuric acid and melamine over anatase TiO<sub>2</sub>,” *Applied Catalysis B: Environmental*, vol. 115–116, pp. 129–137, 2012.
- [11] P. M. Schaber, J. Colson, S. Higgins, D. Thielen, B. Anspach, and J. Brauer, “Thermal decomposition (pyrolysis) of urea in an open reaction vessel,” *Thermochimica Acta*, vol. 424, no. 1–2, pp. 131–142, 2004.
- [12] L. Xu, W. Watkins, R. Snow, G. Graham, R. McCabe, C. Lambert, and R. O. Carter, “Laboratory and Engine Study of Urea-Related Deposits in Diesel Urea-SCR After-Treatment Systems,” *SAE Technical Paper 2007- 01-1582*, 2007.
- [13] G. Zheng, A. Fila, A. Kotrba, and R. Floyd, “Investigation of Urea Deposits in Urea SCR Systems for Medium and Heavy Duty Trucks,” *SAE Technical Paper 2010-01-1941*, 2010.
- [14] M. Koebel and E. O. Strutz, “Thermal and Hydrolytic Decomposition of Urea for Automotive Selective Catalytic Reduction Systems : Thermochemical and Practical Aspects,” *Ind. Eng. Chem. Res.*, vol. 42, pp. 2093–2100, 2003.

- [15] C. Scott Sluder, J. M. E. Storey, S. A. Lewis, and L. A. Lewis, "Low Temperature Urea Decomposition and SCR Performance," *SAE Technical Paper 2005-01-1858*, 2005.
- [16] A. Nishioka, K. Amou, H. Yokota, and T. Murakami, "A urea-dosing device for enhancing low-temperature performance by active-ammonia production in an SCR system," *SAE Technical Paper 2008-01-1026*, 2008.
- [17] V. Ebrahimian, A. Nicolle, and C. Habchi, "Detailed Modeling of the Evaporation and Thermal Decomposition of Urea-Water Solution in SCR Systems," *American Institute of Chemical Engineers*, vol. 58, no. 7, pp. 1998–2009, 2012.
- [18] T. L. Mckinley, A. G. Alleyne, and C.-f. Lee, "Mixture Non-Uniformity in SCR Systems : Modeling and Uniformity Index Requirements for Steady- State and Transient Operation," *SAE International Journal of Fuels and Lubricants*, vol. 3, no. 1, pp. 486–499, 2010.
- [19] V. O. Strots, S. Santhanam, B. J. Adelman, G. a. Griffin, and E. M. Derybowski, "Deposit Formation in Urea-SCR Systems," *SAE International Journal of Fuels and Lubricants*, vol. 2, no. 2, pp. 283–289, 2009.
- [20] B. Guan, R. Zhan, H. Lin, and Z. Huang, "Review of state of the art technologies of selective catalytic reduction of NO<sub>x</sub> from diesel engine exhaust," *Applied Thermal Engineering*, vol. 66, no. 1-2, pp. 395–414, 2014.
- [21] A. M. Bernhard, *Catalytic urea decomposition, side-reactions and urea evaporation in the selective catalytic reduction of NO<sub>x</sub>*. PhD thesis, ETH Zurich, 2012.
- [22] A. Nishioka, Y. Sukegawa, K. Katogi, H. Mamada, T. Kowatari, T. Mukai, and H. Yokota, "A Study of a New Aftertreatment System (2): Control of Urea Solution Spray for Urea-SCR," *SAE Technical Paper 2006-01-0644*, 2006.

- [23] P. Gaynor, B. Reid, G. Hargrave, T. Lockyer, and J. Wilson, “An Experimental Investigation into DEF Dosing Strategies for Heavy Duty Vehicle Applications,” *SAE International Journal of Engines*, vol. 8, no. 3, 2015.
- [24] A. Roppertz, S. Fügler, and S. Kureti, “Investigation of Urea-SCR at Low Temperatures,” *Topics in Catalysis*, vol. 60, no. 3-5, pp. 199–203, 2016.
- [25] H. Smith, T. Lauer, M. Mayer, and S. Pierson, “Optical and Numerical Investigations on the Mechanisms of Deposit Formation in SCR Systems,” *SAE International Journal of Fuels and Lubricants*, vol. 7, no. 2, pp. 525–542, 2014.
- [26] T. Lockyer, B. Reid, G. Hargrave, P. Gaynor, and J. Wilson, “Optical Investigation on the Ability of a Cordierite Substrate Mixing Device to Combat Deposits in SCR Dosing Systems,” *SAE Technical Paper 2015-01-1039*, 2015.
- [27] F. Birkhold, U. Meingast, and P. Wassermann, “Analysis of the Injection of Urea-Water-Solution for Automotive SCR DeNOx-Systems : Modeling of Two-Phase Flow and Spray / Wall-Interaction,” *SAE Technical Paper 2006-01-0643*, no. 724, 2006.
- [28] F. Birkhold, U. Meingast, P. Wassermann, and O. Deutschmann, “Modeling and simulation of the injection of urea-water-solution for automotive SCR DeNOx-systems,” *Applied Catalysis B: Environmental*, vol. 70, no. 1-4, pp. 119–127, 2007.
- [29] D. Kuhnke, *Spray Wall Interaction Modelling by Dimensionless Data Analysis*. Phd thesis, Universität Darmstadt, 2004.
- [30] F. P. Incropera, D. P. DeWitt, T. L. Bergman, and A. S. Lavine, *Fundamentals of heat and mass transfer*. John Wiley and Sons, 6th ed., 2007.
- [31] A. Lundström and H. Ström, “Modeling aspects of the injection of urea-spray for NOx abatement for heavy duty diesel engines,” in *Sprays: Types, Technology and Modeling*, pp. 257–286, 2011.

- [32] E. Abu-Ramadan, K. Saha, and X. Li, "Numerical Modeling of the Impingement Process of Urea-Water Solution Spray on the Heated Walls of SCR Systems," *SAE Technical Paper 2012-01-1301*, 2012.
- [33] S. F. Benjamin and C. A. Roberts, "Significance of droplet size when injecting aqueous urea into a selective catalytic reduction after-treatment system in a light-duty diesel exhaust," *Institution of Mechanical Engineers - Fuel Systems for IC Engines*, 2012.
- [34] N. S. Nayak, "The Evaporation and Spray Wall Interaction Behavior of Urea Water Solution (UWS) in Selective Catalytic Reduction (SCR) Systems of Modern Automobiles," *SAE Technical Paper 2013-24-0162*, 2013.
- [35] A. Varna, K. Boulouchos, A. Spiteri, P. Dimopoulos Eggenchwiler, and Y. M. Wright, "Numerical Modelling and Experimental Characterization of a Pressure-Assisted Multi-Stream Injector for SCR Exhaust Gas After-Treatment," *SAE International Journal of Engines*, vol. 7, no. 4, pp. 2012–2021, 2014.
- [36] L. Nocivelli, G. Montenegro, Y. Liao, and P. Dimopoulos Eggenchwiler, "Modeling of Aqueous Urea Solution injection with characterization of spray-wall cooling effect and risk of onset of wall wetting," *Energy Procedia*, vol. 82, pp. 38–44, 2015.
- [37] X. Gan, D. Yao, F. Wu, J. Dai, L. Wei, and X. Li, "Quasi 1D modeling of two-phase flow and deposit formation for urea-selective catalytic reduction systems," *Journal of Zhejiang University-SCIENCE A (Applied Physics & Engineering)*, vol. 17, no. 8, pp. 597–613, 2016.
- [38] S. Sazhin, "Advanced models of fuel droplet heating and evaporation," *Progress in Energy and Combustion Science*, vol. 32, no. 2, pp. 162–214, 2006.
- [39] J. Oh, K. Kim, and K. Lee, "Effects of various mixer types on the spatial distribution of a De-NO<sub>x</sub> reductant," *Fuel*, vol. 94, pp. 93–101, 2012.

- [40] L. Hua, Y. Zhao, J. Hu, T. Tao, and Shijin Shuai, "Comparison Between Air-Assisted and Airless Urea Spray for Diesel SCR System by PDA and CFD," *SAE Technical Paper 2012-01-1081*, 2012.
- [41] A. Muzard, "Development of a 3D spray visualisation method for low-pressure injectors," *MTZ*, pp. 50–55, 2013.
- [42] N. van Vuuren, "High Speed Video Measurements of a High Temperature Urea Injector Spray - Comparison of Spray Evolution in Water and AUS-32," *SAE Technical Paper 2013-01-2527*, 2013.
- [43] J. Oh and K. Lee, "Spray characteristics of a urea solution injector and optimal mixer location to improve droplet uniformity and NO<sub>x</sub> conversion efficiency for selective catalytic reduction," *Fuel*, vol. 119, pp. 90–97, mar 2014.
- [44] A. Spiteri and P. Dimopoulos Eggenschwiler, "Experimental fluid dynamic investigation of urea-water sprays for diesel selective catalytic reduction-denox applications," *Industrial and Engineering Chemistry Research*, vol. 53, no. 8, pp. 3047–3055, 2014.
- [45] A. Varna, A. C. Spiteri, Y. M. Wright, and P. Dimopoulos, "Experimental and numerical assessment of impingement and mixing of urea water sprays for nitric oxide reduction in diesel exhaust," *Applied Energy*, vol. 157, pp. 824–837, 2015.
- [46] L. Postrioti, G. Brizi, C. Ungaro, M. Mosser, and F. Bianconi, "A methodology to investigate the behaviour of urea-water sprays in high temperature air flow for SCR de-NO<sub>x</sub> applications," *Fuel*, vol. 150, pp. 548–557, 2015.
- [47] N. Van Vuuren, G. Brizi, G. Buitoni, L. Postrioti, and C. Ungaro, "Experimental Analysis of the Urea-Water Solution Temperature Effect on the Spray Characteristics in SCR Systems," *SAE Technical Paper 2015-24-2500*, 2015.



- [48] A. Spiteri, *Experimental Investigation of The Injection Process in urea-SCR Denox Exhaust Gas Aftertreatment Systems*. PhD thesis, ETH Zurich, 2016.
- [49] S. Prabhu S, N. S. Nayak, N. Kapilan, and V. Hindasageri, “An experimental and numerical study on effects of exhaust gas temperature and flow rate on deposit formation in Urea-Selective Catalytic Reduction ( SCR ) system of modern automobiles,” *Applied Thermal Engineering*, vol. 111, pp. 1211–1231, 2017.
- [50] J. Oh, K. Kim, and K. Lee, “Spray characteristics of four-hole injectors used for a hydrocarbon lean nitrogen oxide catalyst system in a diesel engine,” *Proceedings of the Institution of Mechanical Engineers, Part D: Journal of Automobile Engineering*, vol. 226, no. 8, pp. 1073–1087, 2012.
- [51] N. Wruck, *Transientes Sieden von Tropfen bei Wandaufprall*. PhD thesis, RWTH Aachen, 1998.
- [52] U. Meingast, *Spray-Wand-Wechselwirkung bei der dieselmotorischen Direkteinspritzung*. PhD thesis, RWTH Aachen, 2003.
- [53] F. Akao, K. Araki, S. Mori, and A. Moriyama, “Deformation behaviors of a liquid droplet impinging onto hot metal surface,” *Transactions of the Iron and Steel Institute of Japan*, vol. 20, no. 11, pp. 737–743, 1980.
- [54] M. R. Panão and A. L. N. Moreira, “Visualization and Analysis of Spray Impingement Under Cross-Flow Conditions,” *SAE Technical Paper 2002-01-2664*, 2002.
- [55] M. R. O. Panão and A. L. N. Moreira, “Experimental Characterization of an Cross-Flow Conditions,” *Atomization and Sprays*, vol. 15, pp. 201–222, 2005.
- [56] M. R. O. Panão, A. L. N. Moreira, and D. F. G. Durão, “Effect of a cross-flow on spray impingement with port fuel injection systems for HCCI engines,” *Fuel*, vol. 106, pp. 249–257, 2013.

- [57] C. Arcoumanis and J. C. Chang, “Heat transfer between a heated plate and an impinging transient diesel spray,” *Experiments in Fluids*, vol. 16, no. 2, pp. 105–119, 1993.
- [58] C. Arcoumanis and J. C. Chang, “Flow and Heat Transfer Characteristics of Impinging Transient Diesel Sprays,” *SAE Technical Paper 940678*, 1994.
- [59] C. Arcoumanis and P. Cutter, “Flow and heat transfer characteristics of impinging diesel sprays under cross-flow conditions,” *SAE Technical Paper 950448*, 1995.
- [60] C. Arcoumanis, P. Cutter, and D. S. Whitelaw, “Heat Transfer Processes in Diesel Engines,” *Chemical Engineering Research and Design*, vol. 76, no. 2, pp. 124–132, 1998.
- [61] L. Reichelt, U. Meingast, and U. Renz, “Calculating transient wall heat flux from measurements of surface temperature,” *International Journal of Heat and Mass Transfer*, vol. 45, pp. 579–584, 2002.
- [62] U. Meingast, L. Reichelt, and U. Renz, “Measuring transient wall heat flux under diesel engine conditions,” *International Journal of Engine Research*, vol. 5, no. 5, pp. 443–452, 2005.
- [63] A. L. N. Moreira, J. Carvalho, and M. R. O. Panão, “An experimental methodology to quantify the spray cooling event at intermittent spray impact,” *International Journal of Heat and Fluid Flow*, vol. 28, no. 2, pp. 191–202, 2007.
- [64] T. L. Cox and S. C. Yao, “Heat Transfer of Sprays of Large Water Drops Impacting on High Temperature Surfaces,” *Journal of Heat Transfer*, vol. 121, no. 2, p. 446, 1999.
- [65] S. C. Yao and T. L. Cox, “General Heat Transfer Correlation for Impacting Water Sprays on High-Temperature Surfaces,” *Experimental Heat Transfer*, vol. 15, no. 4, pp. 207–219, 2002.

- [66] J. Wendelstorf, K.-H. Spitzer, and R. Wendelstorf, "Spray water cooling heat transfer at high temperatures and liquid mass fluxes," *International Journal of Heat and Mass Transfer*, vol. 51, no. 19-20, pp. 4902–4910, 2008.
- [67] K. A. Estes and I. Mudawar, "Correlation of Sauter mean diameter and critical heat flux for spray cooling of small surfaces," *International Journal of Heat and Mass Transfer*, vol. 38, no. 16, pp. 2985–2996, 1995.
- [68] W. Jia and H. H. Qiu, "Experimental investigation of droplet dynamics and heat transfer in spray cooling," *Experimental Thermal and Fluid Science*, vol. 27, no. 7, pp. 829–838, 2003.
- [69] A. Labergue, M. Gradeck, and F. Lemoine, "Comparative study of the cooling of a hot temperature surface using sprays and liquid jets," *International Journal of Heat and Mass Transfer*, vol. 81, pp. 889–900, 2015.
- [70] R. Dou, Z. Wen, and G. Zhou, "Heat transfer characteristics of water spray impinging on high temperature stainless steel plate with finite thickness," *International Journal of Heat and Mass Transfer*, vol. 90, pp. 376–387, 2015.
- [71] H. M. Al-Ahmadi and S. C. Yao, "Spray Cooling of High Temperature Metals Using High Mass Flux Industrial Nozzles," *Experimental Heat Transfer*, vol. 21, pp. 38–54, 2008.
- [72] S. Sebelius, T. T. Le, L. J. Pettersson, and H. Lind, "Identification of urea decomposition from an SCR perspective; A combination of experimental work and molecular modeling," *Chemical Engineering Journal*, vol. 231, pp. 220–226, 2013.
- [73] A. Munnannur, M. Chiruta, and Z. G. Liu, "Thermal and Fluid Dynamic Considerations in Aftertreatment System Design for SCR Solid Deposit Mitigation," *SAE Technical Paper 2012-01-1287*, 2012.

- [74] M. D. Amiridis, T. Zhang, and R. J. Farrauto, "Selective catalytic reduction of nitric oxide by hydrocarbons," *Applied Catalysis B: Environmental*, vol. 10, pp. 203–227, 1996.
- [75] R. Burch, J. P. Breen, and F. C. Meunier, "A review of the selective reduction of NO<sub>x</sub> with hydrocarbons under lean-burn conditions with non-zeolitic oxide and platinum group metal catalysts," *Applied Catalysis B: Environmental*, vol. 39, pp. 283–303, 2002.
- [76] A. Kotsifa, D. I. Kondarides, and X. E. Verykios, "A comparative study of the selective catalytic reduction of NO by propylene over supported Pt and Rh catalysts," *Applied Catalysis B: Environmental*, vol. 80, pp. 260–270, 2008.
- [77] M. Sridhar, J. Anton, V. Bokhoven, and O. Kröcher, "Applied Catalysis A : General Effect of ammonia on the decomposition of ammonium formate over Au/TiO<sub>2</sub> under oxidizing conditions relevant to SCR : Enhancement of formic acid decomposition rate and CO<sub>2</sub> production," *Applied Catalysis A: General*, vol. 486, pp. 219–229, 2014.
- [78] M. Sridhar, D. Ferri, M. Elsener, J. A. V. Bokhoven, and O. Kröcher, "Promotion of Ammonium Formate and Formic Acid Decomposition over Au/TiO<sub>2</sub> by Support Basicity under SCR-Relevant Conditions," *ACS catalysis*, vol. 5, pp. 4772–4782, 2015.
- [79] Y. Liao, R. Furrer, P. Dimopoulos Eggenschwiler, and K. Boulouchos, "Experimental investigation of the heat transfer characteristics of spray/ wall interaction in diesel selective catalytic reduction systems," *Fuel*, vol. 190, pp. 163–173, 2017.
- [80] M. Eichelbaum, R. J. Farrauto, and M. J. Castaldi, "Applied Catalysis B : Environmental The impact of urea on the performance of metal exchanged zeolites for the selective catalytic reduction of NO<sub>x</sub> Part I . Pyrolysis and hydrolysis of urea over zeolite catalysts," *Applied Catalysis B: Environmental*, vol. 97, no. 1-2, pp. 90–97, 2010.

- [81] A. L. N. Moreira, A. S. Moita, and M. R. Panão, “Advances and challenges in explaining fuel spray impingement: How much of single droplet impact research is useful?,” *Progress in Energy and Combustion Science*, vol. 36, no. 5, pp. 554–580, 2010.
- [82] Z. Wang, H. Ding, X. Ma, H. Xu, and M. L. Wyszynski, “Ultra-high speed imaging study of the diesel spray close to the injector tip at the initial opening stage with single injection,” *Applied Energy*, vol. 165, pp. 335–344, 2016.
- [83] Z. Wang, Y. Li, C. Wang, H. Xu, and M. L. Wyszynski, “Experimental study on primary breakup of diesel spray under cold start conditions,” *Fuel*, vol. 183, pp. 617–626, 2016.
- [84] F. Puschmann and E. Specht, “Transient measurement of heat transfer in metal quenching with atomized sprays,” *Experimental Thermal and Fluid Science*, vol. 28, no. 6, pp. 607–615, 2004.
- [85] B. Li, T. Cader, J. Schwarzkopf, K. Okamoto, and B. Ramaprian, “Spray angle effect during spray cooling of microelectronics: Experimental measurements and comparison with inverse calculations,” *Applied Thermal Engineering*, vol. 26, no. 16, pp. 1788–1795, 2006.
- [86] M. Gradeck, J. A. Ouattara, B. Rémy, and D. Maillet, “Solution of an inverse problem in the Hankel space - Infrared thermography applied to estimation of a transient cooling flux,” *Experimental Thermal and Fluid Science*, vol. 36, pp. 56–64, 2012.
- [87] D. Massiot, F. Fayon, M. Capron, I. King, L. Calv, B. Alonso, J.-o. Durand, B. Bujoli, Z. Gan, and G. Hoatson, “Modelling one- and two-dimensional solid-state NMR spectra,” *Magnetic Resonance in Chemistry*, vol. 40, no. 1, pp. 70–76, 2002.
- [88] European Union, “Regulation (EC) No 595/2009 of the European Parliament and of the Council of 18 June 2009 on type-approval of motor vehicles and engines with respect to emissions from heavy duty vehicles (Euro VI),” 2009.

- [89] L. Wang, B. Sundén, A. Borg, and H. Abrahamsson, “Heat Transfer Characteristics of an Impinging Jet in Crossflow,” *Journal of Heat Transfer*, vol. 133, no. 12, p. 122202, 2011.
- [90] Y. Liao, P. Dimopoulos Eggenschwiler, A. Spiteri, L. Nocivelli, G. Montenegro, and K. Boulouchos, “Fluid Dynamic Comparison of AdBlue Injectors for SCR Applications,” *SAE International Journal of Engines*, vol. 8, no. 5, pp. 2303–2311, 2015.
- [91] Watanabe Atsuo, Shimizu Ken, “Knowledge of electromagnetic waves in the food industry (1),” *Chemical Magazine MOL*, pp. 120–128, 1987.
- [92] C. Chen, “Attenuation of Electromagnetic Radiation by Haze, Fog, Clouds, and Rain,” tech. rep., 1975.
- [93] Gaussorgues G., *Thermographie Infrarouge Principes*. 1989.
- [94] J. V. Beck, B. Blackwell, and C. R. S. Clair, *Inverse Heat Conduction: Ill-Posed Problems*. Wiley-Interscience, 1985.
- [95] F. Puschmann, E. Specht, and J. Schmidt, “Measurement of spray cooling heat transfer using an infrared-technique in combination with the phase-Doppler technique and a patternator,” *Int J Heat Technol*, vol. 19, pp. 51–56, 2001.
- [96] Y. Liao, L. Nocivelli, P. Dimopoulos Eggenschwiler, and A. Spiteri, “Experimental investigation of urea-water sprays in Selective Catalytic Reduction (SCR) systems,” *Proceedings 15. Internationales Stuttgarter Symposium*, pp. 953–966, 2015.
- [97] W. Brack, B. Heine, F. Birkhold, M. Kruse, and O. Deutschmann, “Formation of Urea-Based Deposits in an Exhaust System : Numerical Predictions and Experimental Observations on a Hot Gas Test Bench,” *Emission Control Science and Technology*, pp. 115–123, 2016.

- [98] S.-J. Jeong, S.-J. Lee, and W.-S. Kim, “Numerical study on the optimum injection of urea– water solution for SCR DeNO<sub>x</sub> system of a heavy-duty diesel engine to improve DeNO<sub>x</sub> performance and reduce NH<sub>3</sub> slip,” *Environmental Engineering Science*, vol. 25, no. 7, pp. 1017–1036, 2008.
- [99] Y. Liao, P. Dimopoulos Eggenschwiler, D. Rentsch, F. Curto, and K. Boulouchos, “Characterization of the urea-water spray impingement in diesel selective catalytic reduction systems,” *Applied Energy*, vol. 205, pp. 964–975, 2017.
- [100] Y. Liao, P. Dimopoulos Eggenschwiler, R. Furrer, M. Wang, and K. Boulouchos, “Heat transfer characteristics of urea-water spray impingement on hot surfaces,” *International Journal of Heat and Mass Transfer*, vol. 117, pp. 447–457, 2018.
- [101] Y. Liao and P. Dimopoulos Eggenschwiler, “Experimental investigation of heat transfer characteristics of UWS spray impingement in diesel SCR,” *Proceedings 16. Internationales Stuttgarter Symposium*, pp. 49–58, 2016.
- [102] A. Spiteri, Y. Liao, and P. Dimopoulos Eggenschwiler, “Comparison of Pressure and Air-Assisted Atomizers for Urea-SCR Injection in Diesel Engine Exhaust,” *Proceedings 14. Internationales Stuttgarter Symposium*, pp. 911–921, 2014.
- [103] L. Nocivelli, G. Montenegro, A. Onorati, F. Curto, P. Dimopoulos Eggenschwiler, Y. Liao, and A. Vogel, “Quantitative Analysis of Low Pressure-Driven Spray Mass Distribution and Liquid Entrainment for SCR Application through a Mechanical Patternator,” *SAE Technical Paper 2017-01-0965*, 2017.





# Curriculum Vitae

## Personal Data

Name	Yujun Liao
Date of birth	11.08.1989
Place of birth	Changsha, China
Nationality	Chinese

## Education

2014 – 2017	Doctoral student at ETH Zürich and EMPA, Aerothermochemistry and Combustion Systems Laboratory
2011 – 2014	Studies in Electrical Engineering at ETH Zürich MSc Energy Science and Technology in June 2014
2008 – 2011	Studies in Automotive Engineering at Politecnico di Torino BSc in July 2011
2007 – 2008	Bachelor Studies in Energy, Power System and Automation at Xi'an Jiaotong University
2004 – 2007	High School Attached to Hunan Normal University, China High School Diploma in June 2007



## Journal publications

- Y. Liao, P. Dimopoulos Eggenschwiler, A. Spiteri, L. Nocivelli, G. Montenegro, and K. Boulouchos, “Fluid Dynamic Comparison of AdBlue Injectors for SCR Applications,” *SAE International Journal of Engines*, vol. 8, no. 5, pp. 2303–2311, 2015
- Y. Liao, R. Furrer, P. Dimopoulos Eggenschwiler, and K. Boulouchos, “Experimental investigation of the heat transfer characteristics of spray/wall interaction in diesel selective catalytic reduction systems,” *Fuel*, vol. 190, pp. 163–173, 2017
- Y. Liao, P. Dimopoulos Eggenschwiler, D. Rentsch, F. Curto, and K. Boulouchos, “Characterization of the urea-water spray impingement in diesel selective catalytic reduction systems,” *Applied Energy*, vol. 205, pp. 964–975, 2017
- Y. Liao, P. Dimopoulos Eggenschwiler, R. Furrer, M. Wang, and K. Boulouchos, “Heat transfer characteristics of urea-water spray impingement on hot surfaces,” *International Journal of Heat and Mass Transfer*, vol. 117, pp. 447–457, 2018
- A. Spiteri, P. Dimopoulos Eggenschwiler, Y. Liao, G. Wigley, K. A. Michalow-Mauke, M. Elsener, O. Kröcher, and K. Boulouchos, “Comparative analysis on the performance of pressure and air-assisted urea injection for selective catalytic reduction of NO<sub>x</sub>,” *Fuel*, vol. 161, pp. 269–277, 2015
- L. Nocivelli, G. Montenegro, Y. Liao, and P. Dimopoulos Eggenschwiler, “Modeling of Aqueous Urea Solution injection with characterization of spray-wall cooling effect and risk of onset of wall wetting,” *Energy Procedia*, vol. 82, pp. 38–44, 2015

## Conference publications

- Y. Liao, L. Nocivelli, P. Dimopoulos Eggenschwiler, and A. Spiteri, “Experimental investigation of urea-water sprays in Selective Catalytic

Reduction (SCR) systems,” *Proceedings 15. Internationales Stuttgarter Symposium*, pp. 953–966, 2015

Y. Liao and P. Dimopoulos Eggenschwiler, “Experimental investigation of heat transfer characteristics of UWS spray impingement in diesel SCR,” *Proceedings 16. Internationales Stuttgarter Symposium*, pp. 49–58, 2016

A. Spiteri, Y. Liao, and P. Dimopoulos Eggenschwiler, “Comparison of Pressure and Air-Assisted Atomizers for Urea-SCR Injection in Diesel Engine Exhaust,” *Proceedings 14. Internationales Stuttgarter Symposium*, pp. 911–921, 2014

L. Nocivelli, G. Montenegro, A. Onorati, F. Curto, P. Dimopoulos Eggenschwiler, Y. Liao, and A. Vogel, “Quantitative Analysis of Low Pressure-Driven Spray Mass Distribution and Liquid Entrainment for SCR Application through a Mechanical Patternator,” *SAE Technical Paper 2017-01-0965*, 2017